2019 Fall

"Advanced Physical Metallurgy"

- Non-equilibrium Solidification -

12.02.2019

Eun Soo Park

Office: 33-313
Telephone: 880-7221
Email: espark@snu.ac.kr
Office hours: by appointment

5.7. Annealing of Bulk Metallic Glasses: SR → SCLR (& PS) → Crystallization

5.7.1 Structural Relaxation

RELAXATION BEHAVIOR

Structural relaxation = stabilization

On annealing, the as-synthesized glass slowly transforms toward an "ideal" glass of lower energy through structural relaxation. = annihilation of "defects" or free volume, or recombination of the defects of opposing character, or by changes in both topological and compositional SRO

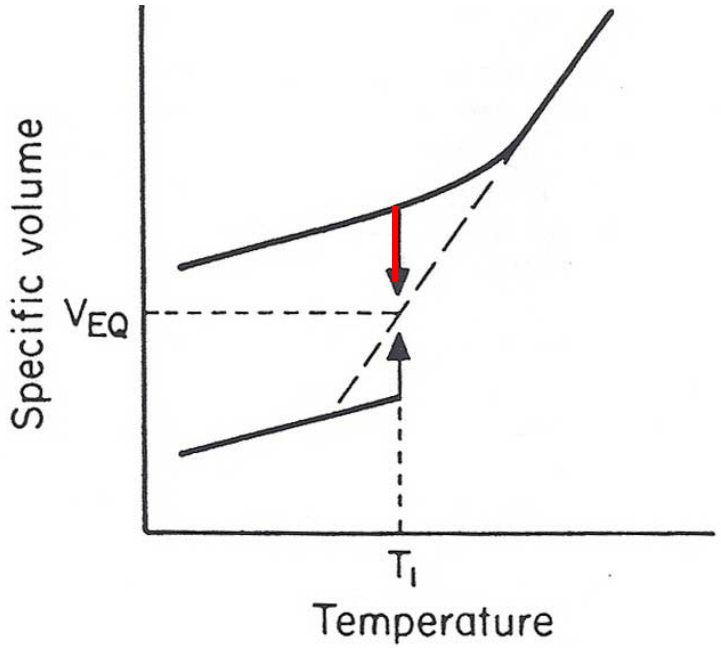

Fig. 9a. Relaxation from initial volumes above and below the equilibrium volume (schematic)

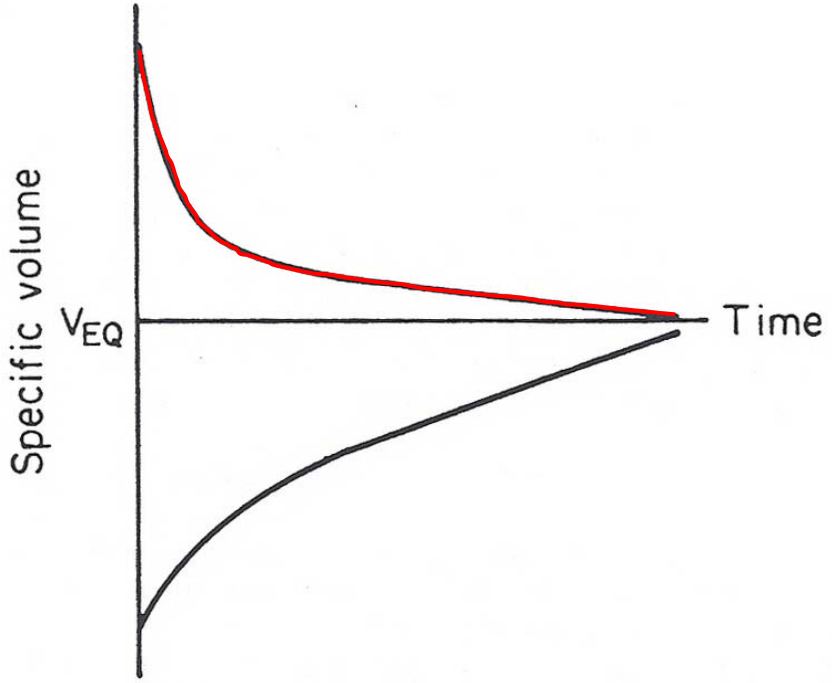

Fig. 9b. Variation of volume with time for initial volumes above and below the equilibrium volume (schematic)

Temperature dependence of relaxation time
: α relaxation (VFT) & β relaxation (Arrhenius)

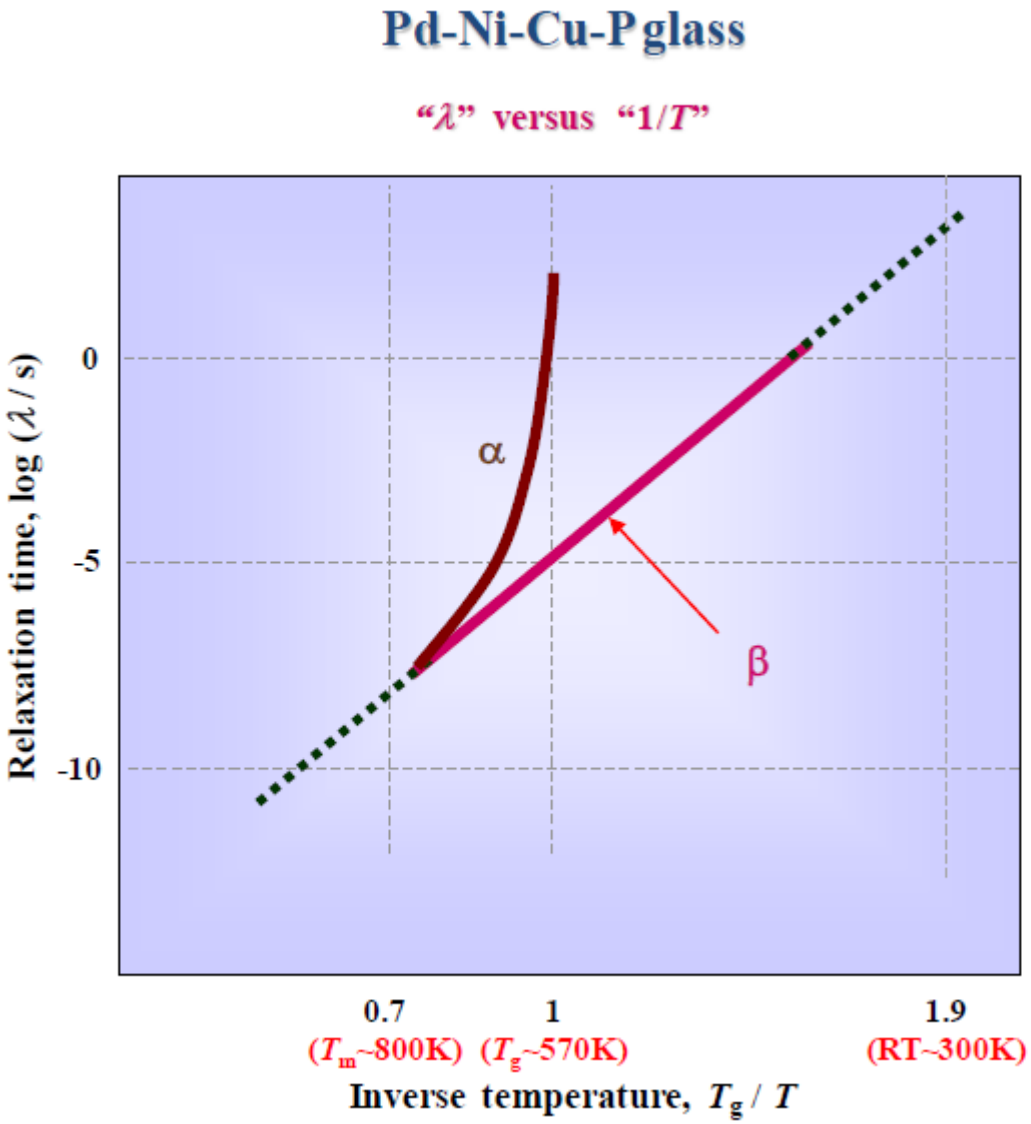

α VFT

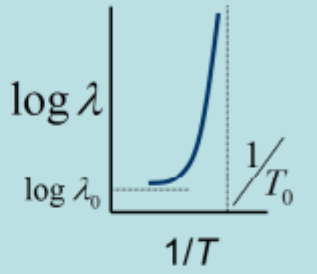

$$\lambda_\alpha = \lambda_{\alpha 0} \exp\left(\frac{Q_\alpha}{T - T_0}\right)$$

Arrhenius β

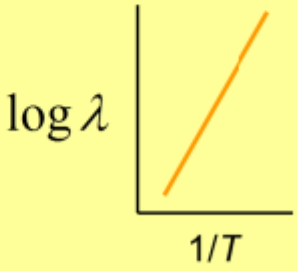

$$\lambda_\beta = \lambda_{\beta,0} \exp\left(\frac{Q_\beta}{kT}\right)$$

Dynamic mechanical relaxations in typical glasses

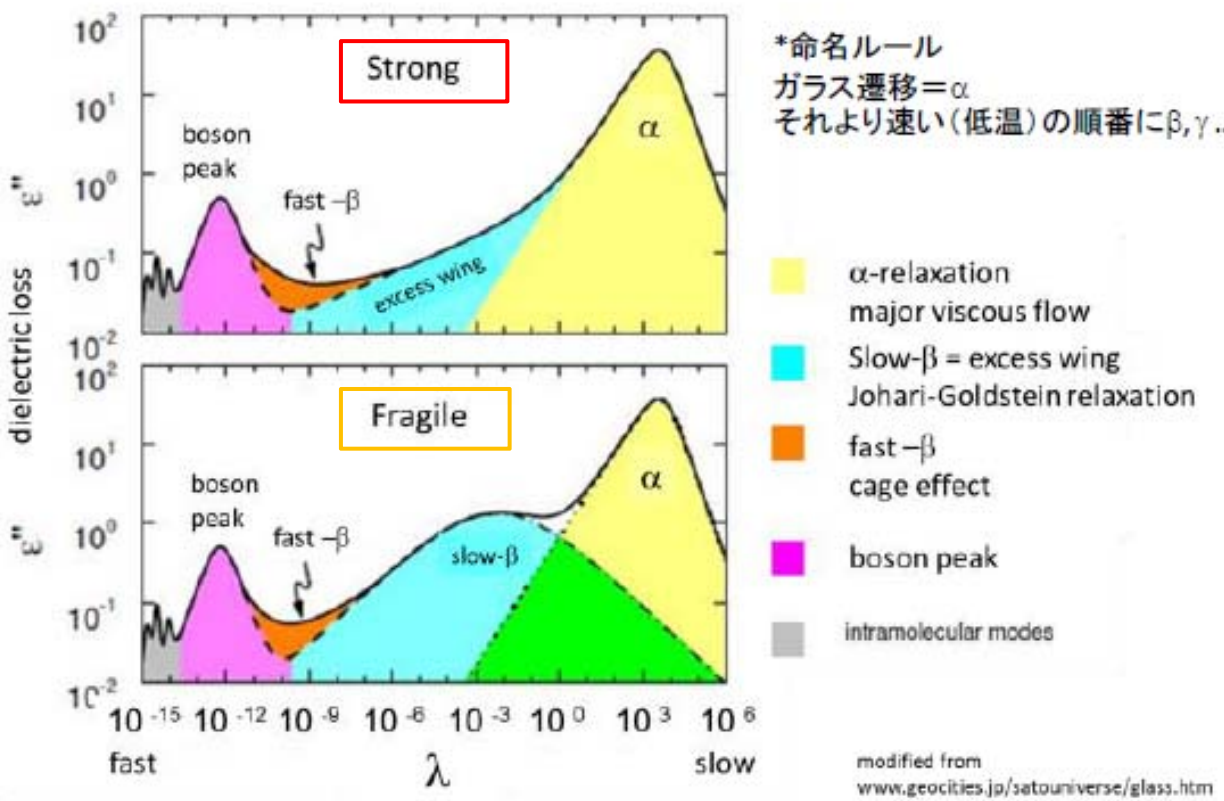

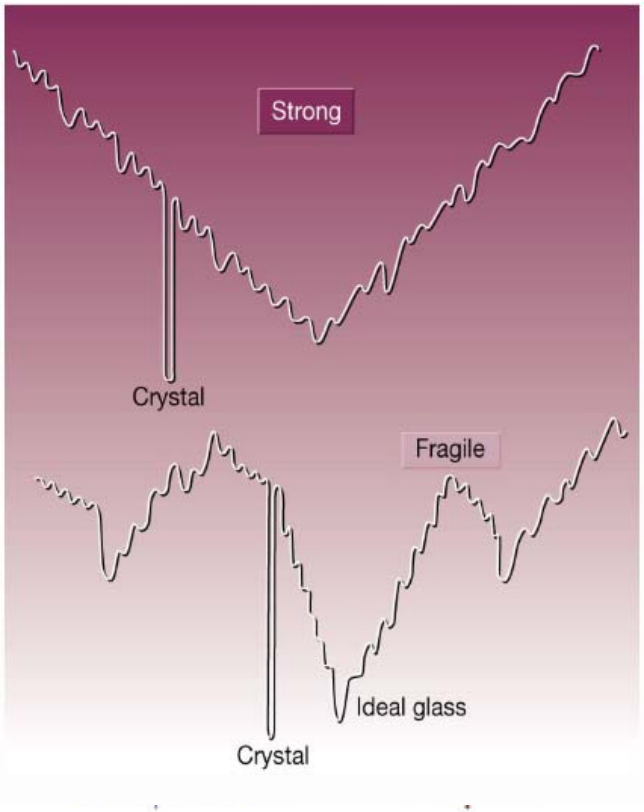

Strong: small deviation of activation E
between α relaxation and β relaxation

Fragile: large deviation of activation E
between α relaxation and β relaxation

Schematic representation of the energy landscapes of strong and fragile substances.

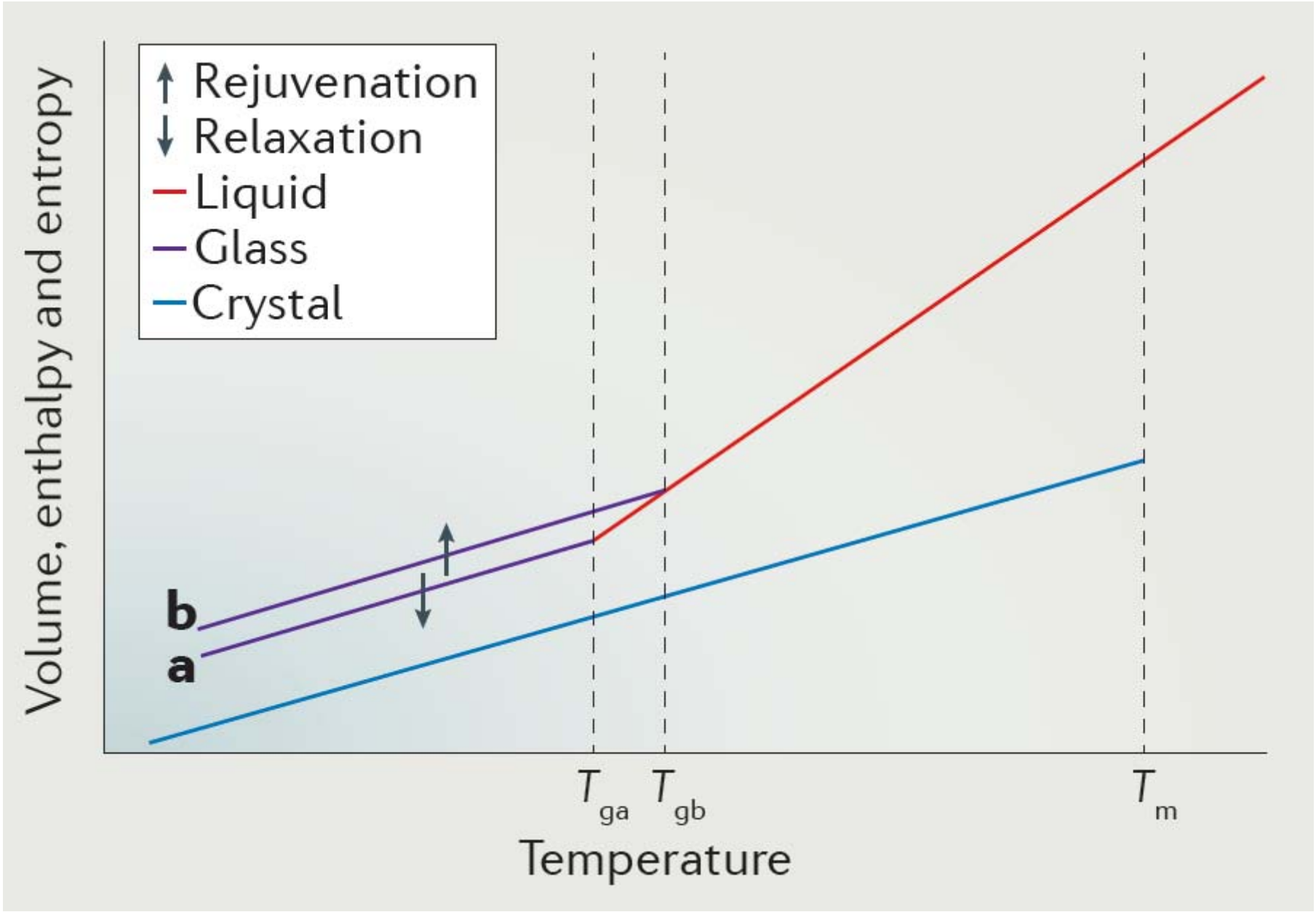
Rejuvenation
Relaxation
Liquid
Glass
Crystal
Volume, enthalpy and entropy
b
a
T_{ga}
T_{gb}
T_m
Temperature

Effect on high pressure torsion(HPT) process on BMGs

Structural rejuvenation

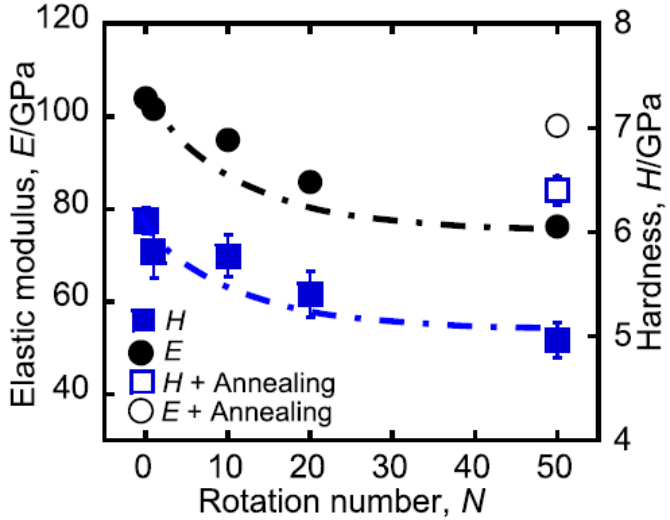

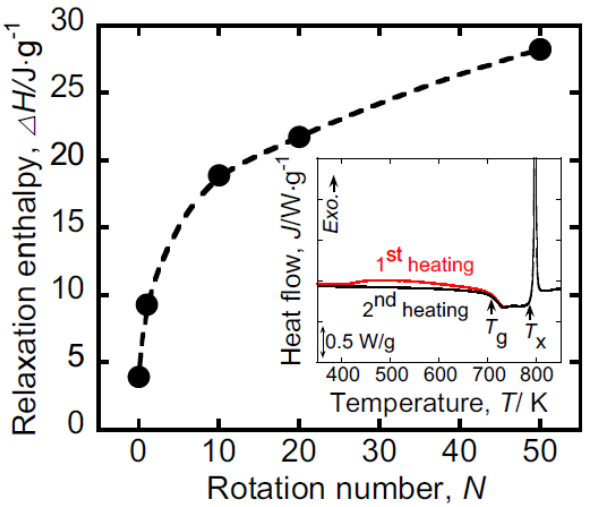

Mechanical softening

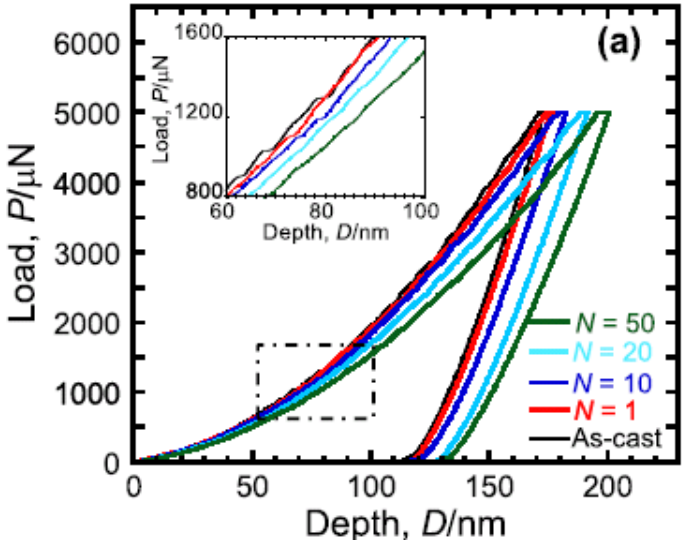

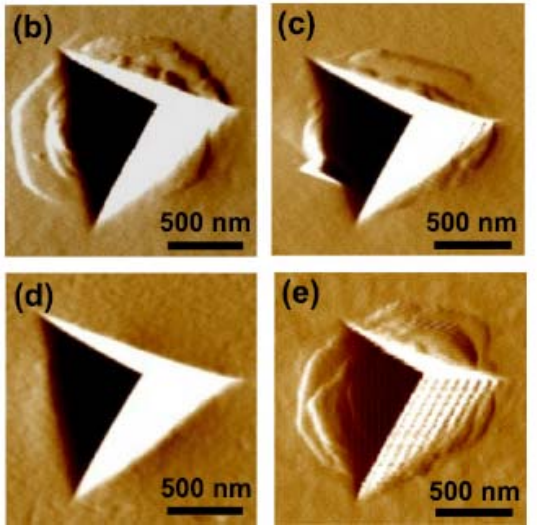

F. Meng et al (2012)

DSC analysis of Zr BMG/ZrN composites after HPT process

Zr BMGs

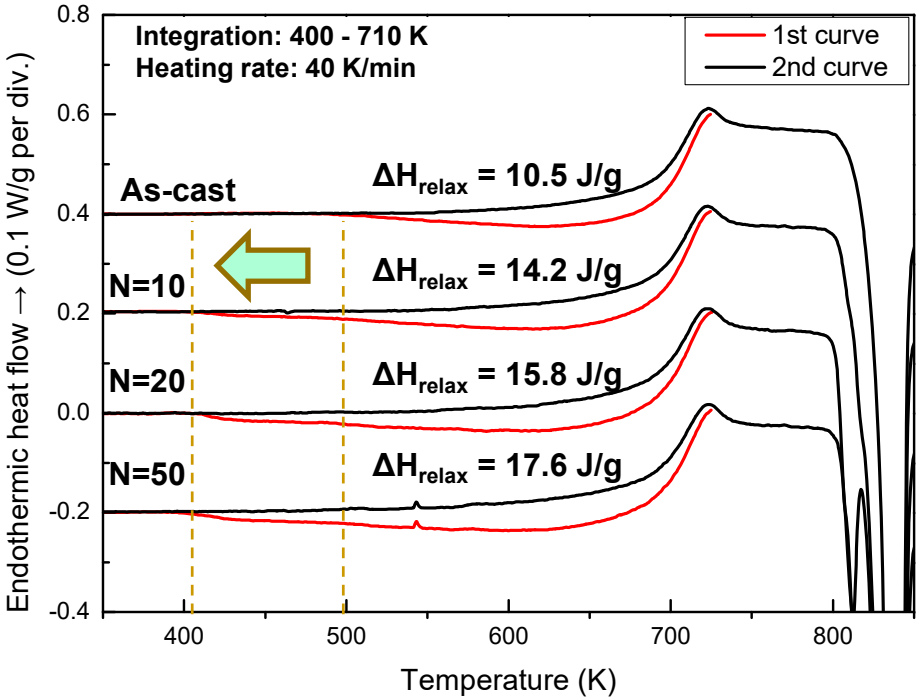

Zr BMG/ZrN composites

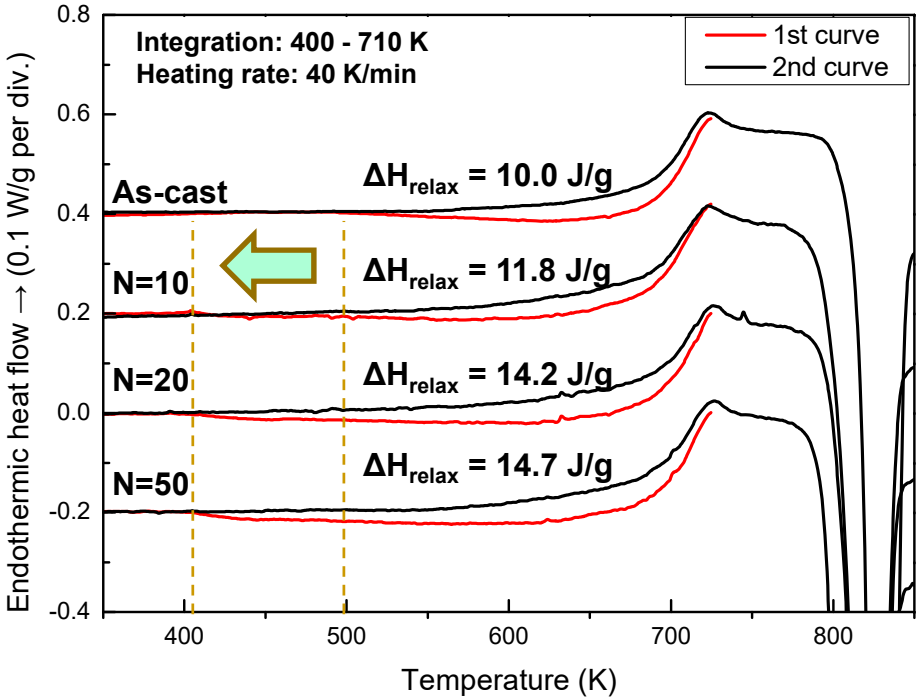

- **Enthalpy of relaxation was increased as # of rotation increased**
- **Enthalpy of relaxation for BMG composites was lower than that for monolithic BMGs.**
- **Relaxation onset temperature of the samples was reduced compared to as-cast sample.**

Structural relaxation of Zr BMG/ZrN composites after HPT process

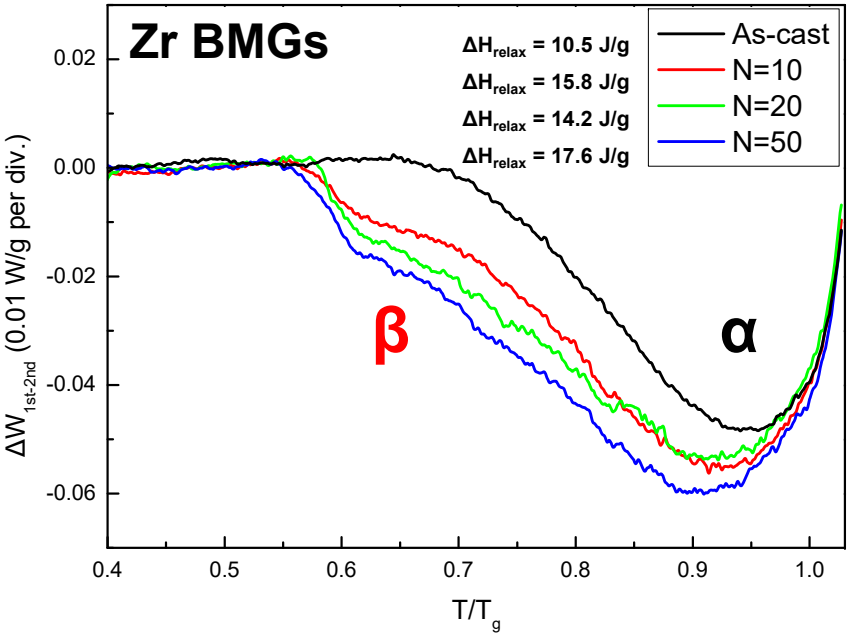

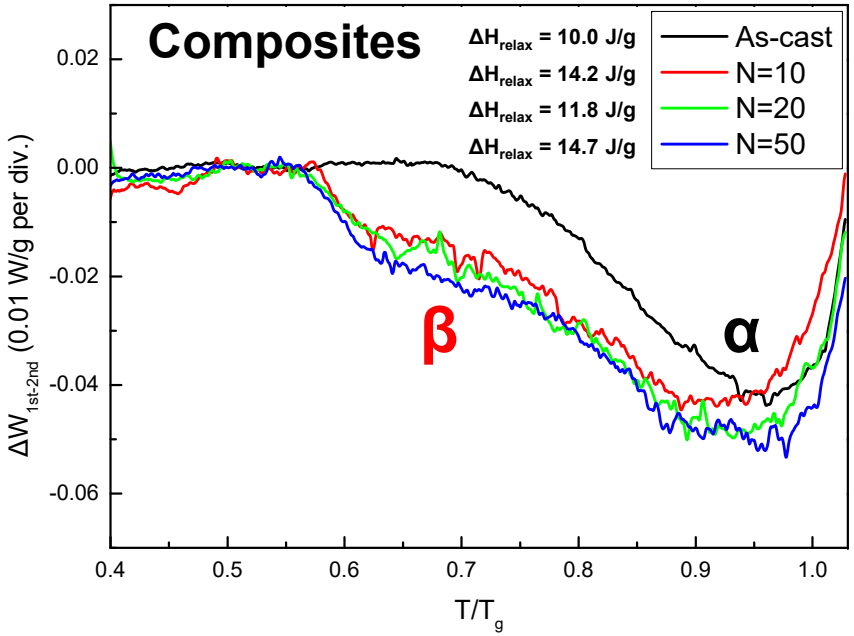

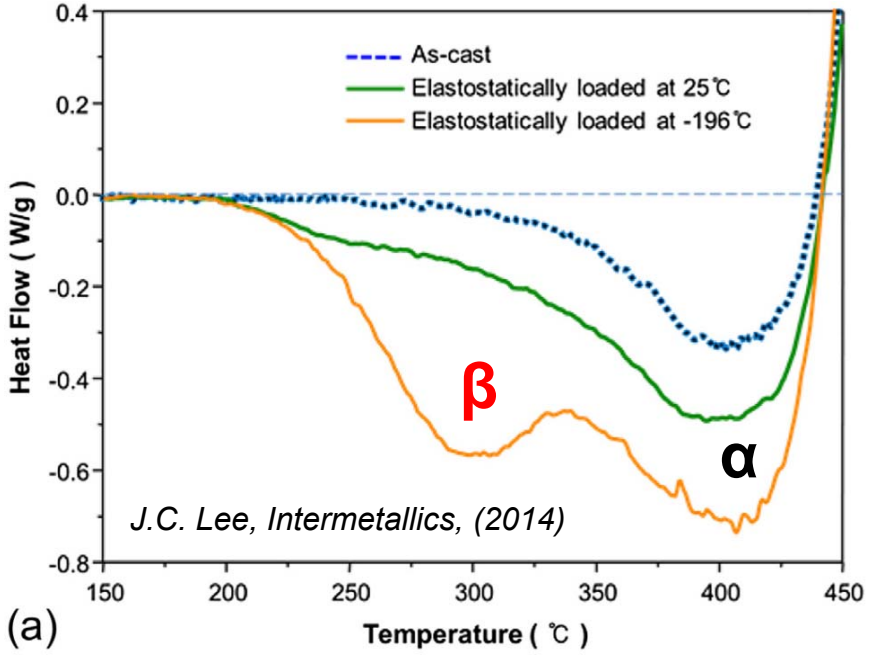

α relaxation
annihilation of short range order
(loose packing, free volume)

β relaxation
annihilation of medium range order
(shear transformation zones)

High pressure torsion of BMGs
→ Short, medium range structural disordering
→ Activation of β relaxation

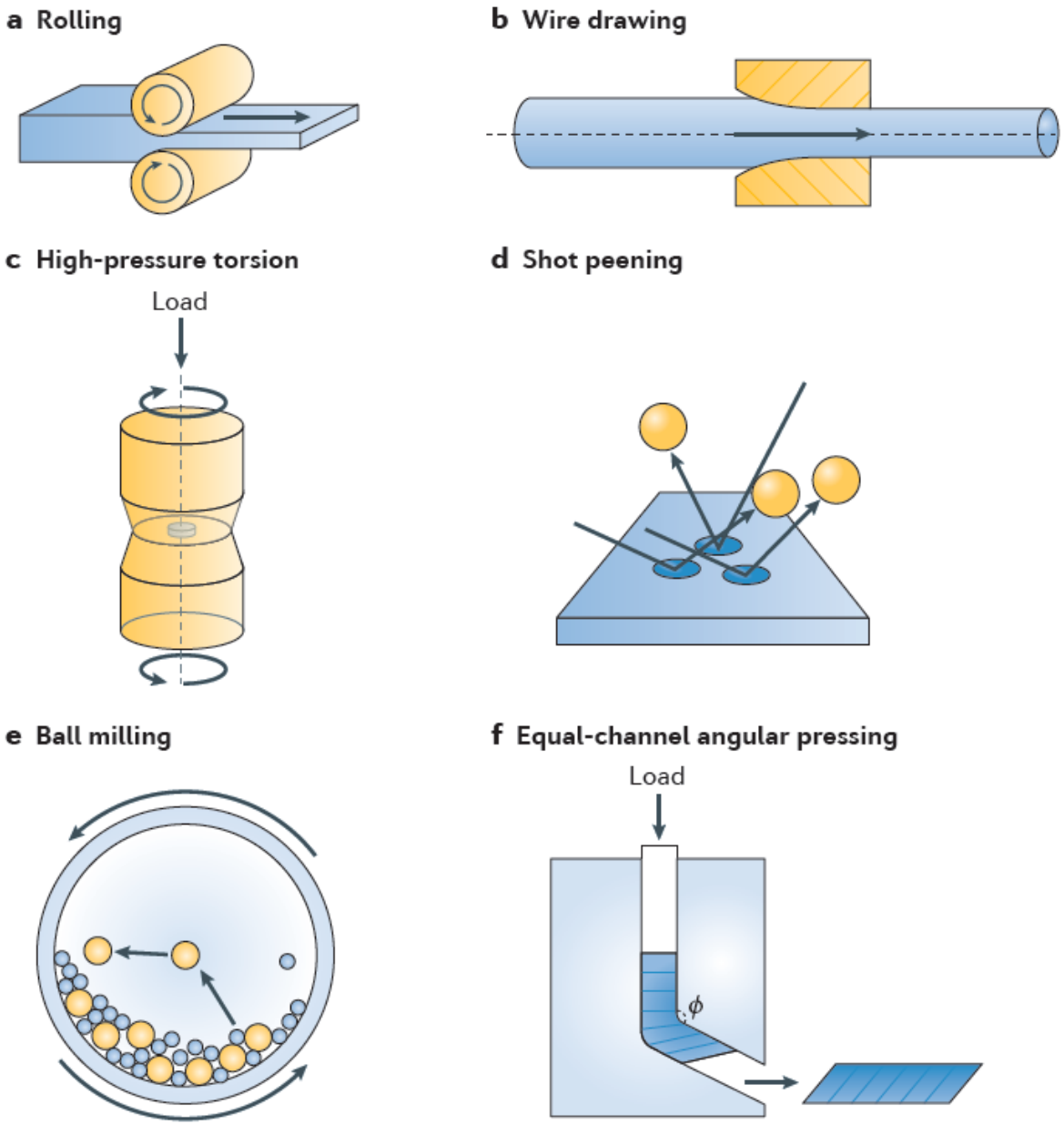
a Rolling
b Wire drawing
c High-pressure torsion
Load
d Shot peening
e Ball milling
f Equal-channel angular pressing
Load
ϕ

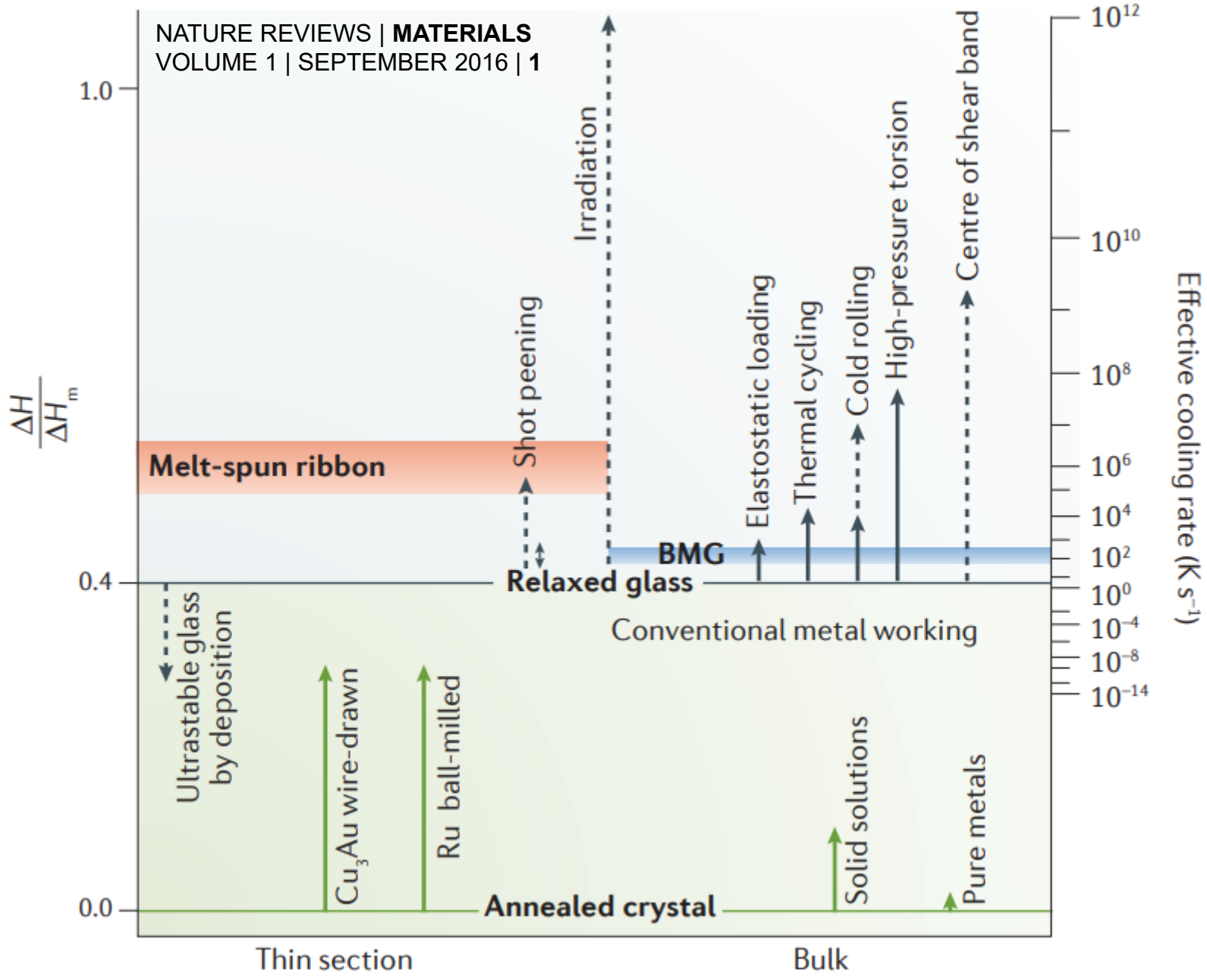

Figure 3 | **Relative enthalpies of deformed metallic states at room temperature.**

* Assuming that the change in enthalpy is entirely due to structural changes in the glassy state and that the average free volume per atom (=V_f/V_m, where V_f is the free volume and V_m is the atomic volume) is proportional to the change in enthalpy:

$$\frac{V_f}{V_m} = C\Delta H \tag{5.5}$$

where C is a constant. The proportionality constant C is determined by first calculating V_f using the Grest and Cohen model [83]:

$$V_f = \frac{k}{2s_0}\left(T - T_0 + \sqrt{(T-T_0)^2 + \frac{4V_a s_0}{k}T}\right) \tag{5.6}$$

$Zr_{44}Ti_{11}Ni_{10}Cu_{10}Be_{25}$ glassy

where k is the Boltzmann constant. The appropriate fit parameters for the above alloy were reported to be: $bV_m s_0/k = 4933\,\mathrm{K}$ with $b = 0.105$, $4V_a s_0/k = 162\,\mathrm{K}$, $T_0 = 672\,\mathrm{K}$. V_m for this alloy has been reported to be 1.67×10^{-29} m^3 near the liquidus temperature. Thus, by calculating V_f from Equation 5.6, V_f/V_m can be calculated.

→ The mechanical properties of metallic glasses (including the BMGs) are affected by the magnitude of free volume present in them. Hence, it becomes important to be able to quantitatively determine the free volume present in the glass to relate the magnitude of free volume to the changes in mechanical properties.

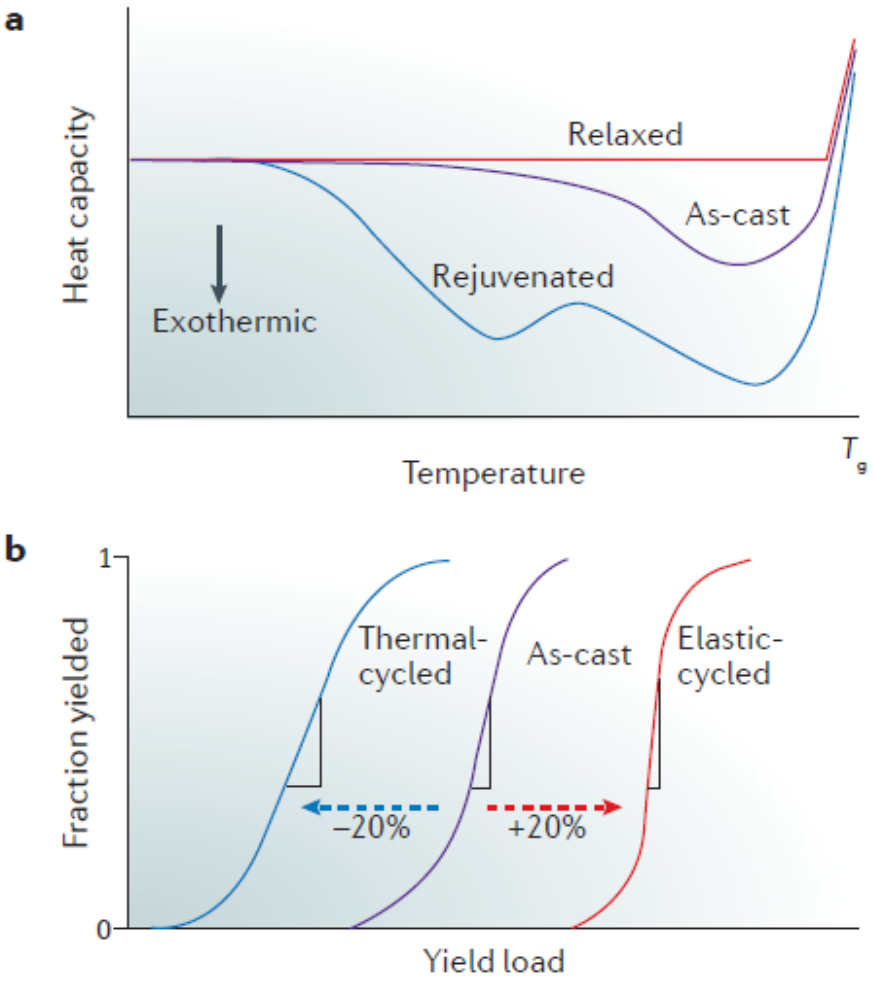
a
Heat capacity
Relaxed
As-cast
Rejuvenated
Exothermic
Temperature
T_g
b
Fraction yielded
1
0
Thermal-cycled
As-cast
Elastic-cycled
–20%
+20%
Yield load

Box 2 | **Energetic processing of metals**

The mechanical deformation of solids transfers energy to the material. This energy transfer also occurs in other processing methods including irradiation. Energetic processing of this type can lead to an energy increase in the sample (rejuvenation) but also to relaxation. These opposing trends are important for metallic glasses, which show a range of energies in their as-cast state (BOX 1). After long processing times, the changes induced in the structure and properties of the solid eventually saturate. More specifically, a steady state is reached in which the rate of structural change (damage) introduced by the processing is balanced by the rate of structural relaxation, which is enhanced by the increased atomic mobility in the processed material. In the steady state, enthalpy, entropy and volume are higher — that is, the state is less relaxed and more rejuvenated — at higher processing rates (strain rate or irradiation flux) and at lower temperatures. This reflects the balance of damage and relaxation rates.

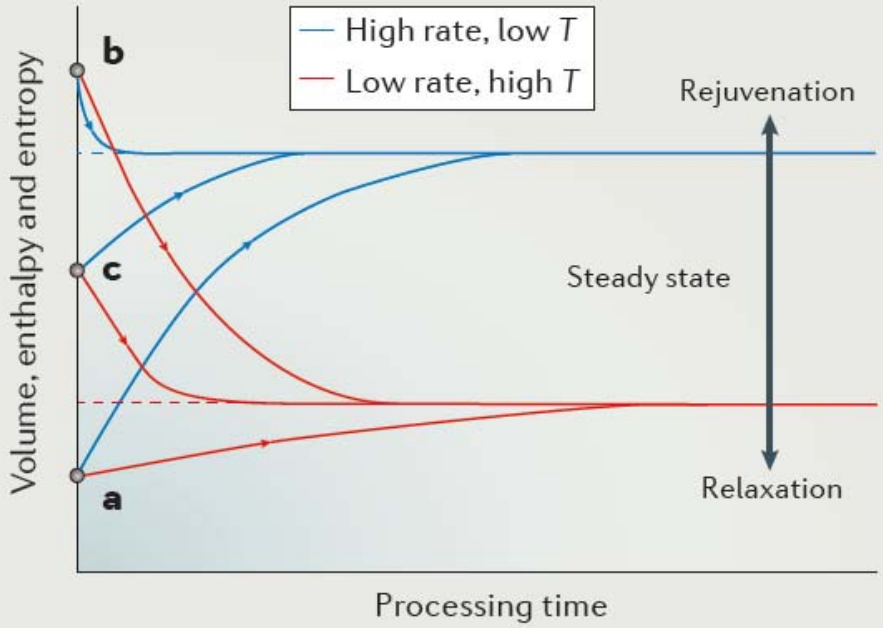

The illustration shows three possible cases: case **a** is a solid of low initial energy (for example, a polycrystal with a low dislocation density or a relaxed glass) that retains some of the injected energy and evolves into a more rejuvenated state; case **b** is a solid of high initial energy (for example, a polycrystal with a high dislocation density or a rapidly quenched glass) that evolves into a more relaxed state; and case **c** is a given initial state that may evolve in either direction, depending on processing rate and temperature. Such considerations, which are well understood for mechanical deformation[52] and irradiation[145] of polycrystalline metals, need to be further explored in the context of the mechanical deformation of metallic glasses.

Annealing of Bulk Metallic Glasses: SR → SCLR (& PS) → Crystallization

5.7.2 Glass Transition: abrupt variation of C_p

Acta Materialia 59 (2011)

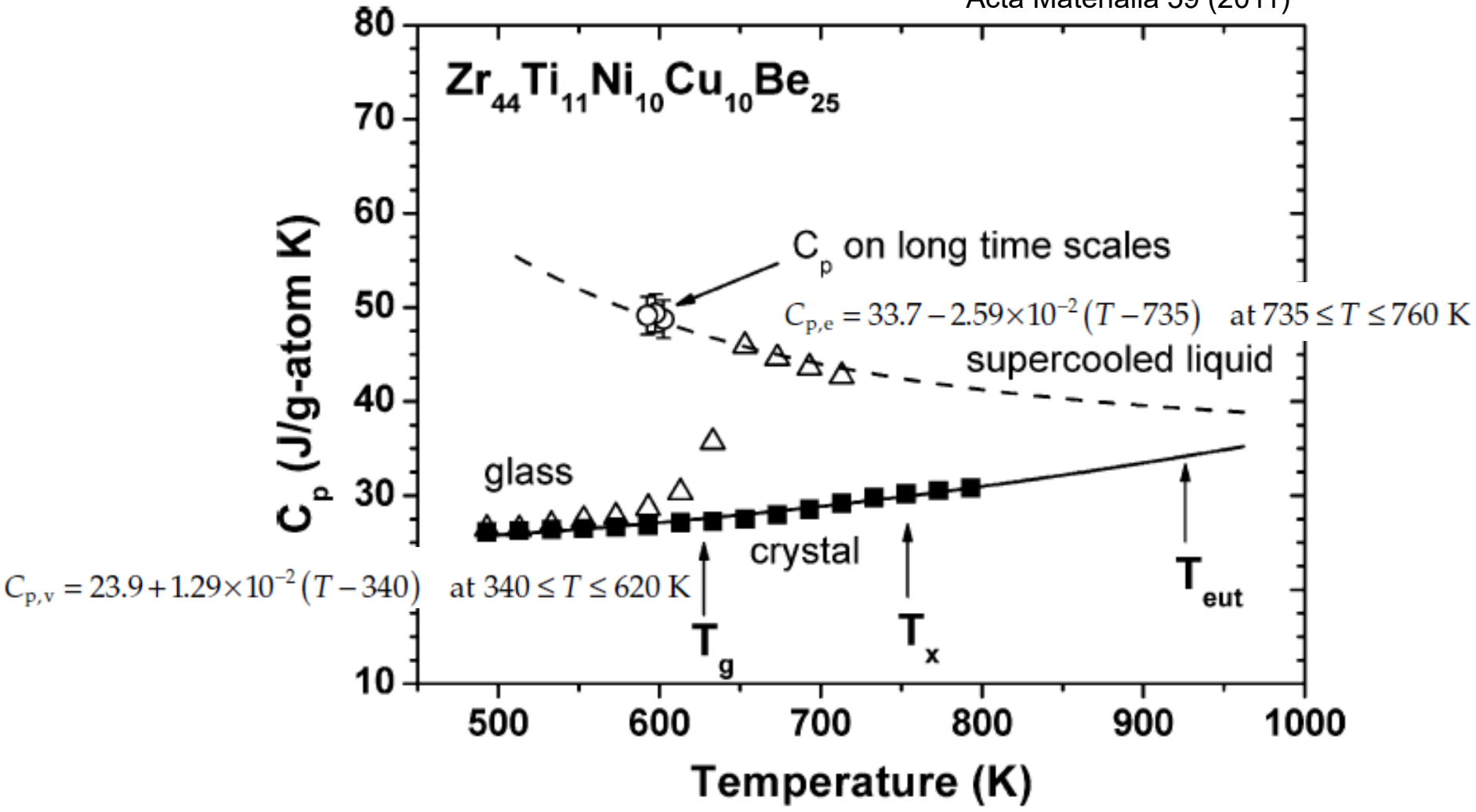

- **Ideal glass transition temperature (T_{oc} =T_g^0)**

: lower temperature limit to occur glass transition thermodynamically

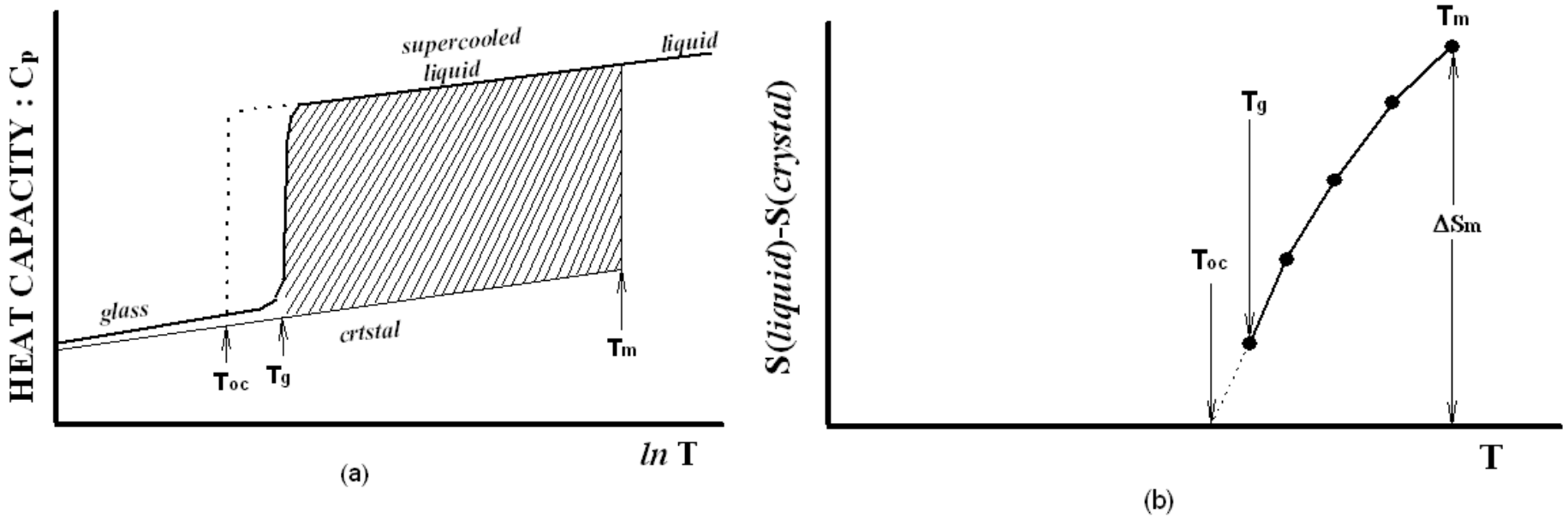

Variation of (a) C_p and (b) excess entropy, S depending on temp. for glass, crystal and liquid. Ideal glass transition temp, T_{oc}. is the temperature when excess entropy is disappeared.

TABLE 5.4

Increase in Specific Heat from the As-Quenched Glassy (g) State to the Supercooled Liquid (scl) Condition, $\Delta C_{p,g\rightarrow scl}$ for Different Metallic Glasses Synthesized by Melt Spinning, and Measured at a Heating Rate of 0.67 K s^{-1} (40 K min^{-1})

Composition	$\Delta C_{p,g\rightarrow scl}$ (J mol^{-1} K^{-1})	ΔT_x (K)	Reference
$La_{55}Al_{20}Cu_{25}$	11.5	59	[84]
$La_{55}Al_{25}Ni_{20}$	14.0	69	[85]
$Mg_{50}Ni_{30}La_{20}$	17.4	58	[86]
$Zr_{60}Al_{15}Ni_{25}$	6.25	77	[87]
$Zr_{65}Cu_{27.5}Al_{7.5}$	—	88	[75]
$Zr_{65}Cu_{17.5}Ni_{10}Al_{7.5}$	14.5	127	[15]

Note: ΔT_x represents the width of the supercooled liquid region.

The $\Delta C_{p,g\rightarrow scl}$ values for the Zr-based metallic glasses are considerably smaller than those of Pd–Ni–P and Pt–Ni–P glasses. Even though the reasons for this difference are not clearly known at the moment, it is possible that it is related to (1) the higher packing fraction of atoms in the glassy Zr-alloys, which require a lower cooling rate to form the glassy structure, (2) the possibility of the atomic configuration in the glassy and supercooled liquid structures being similar, and (3) the higher T_g values in comparison to those of La-, Mg-, Pd-, and Pt-based glassy alloys.

Overshoot in heating process

When the kinetics become fast enough to allow the sample to regain metastable equilibrium

Determined from DSC up-scan

$$\int_{T^*}^{T_f'} (C_p^e - C_p^g) dT_f = \int_{T^*}^{T'} (C_p - C_p^g) dT$$

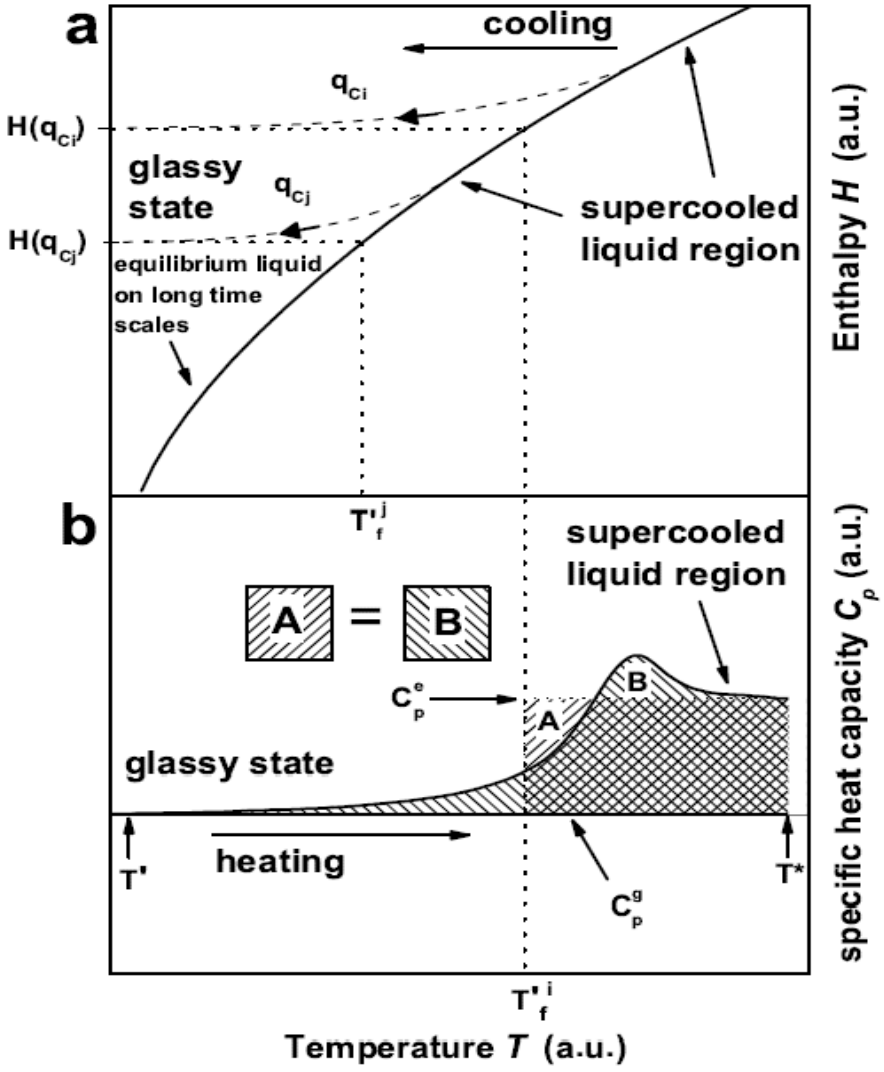

J. Appl. Phys. 107, 123529 (2010)

5.7.3 Phase separation

2-Amorphous phases

Polymer

(AFM)
PGMA/PS

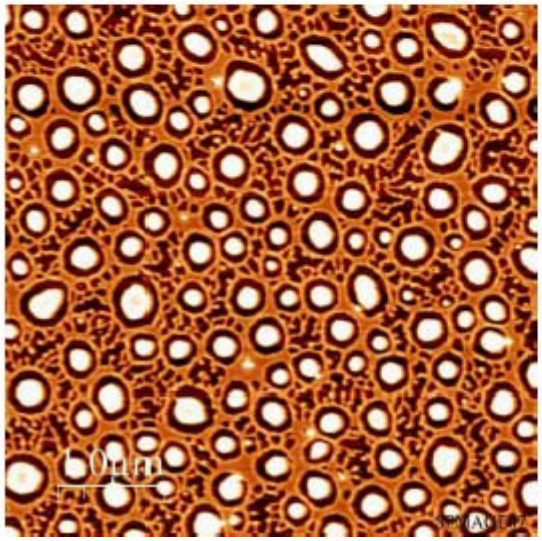

Oxide glass

(SEM)
SiO_2-NaO_2

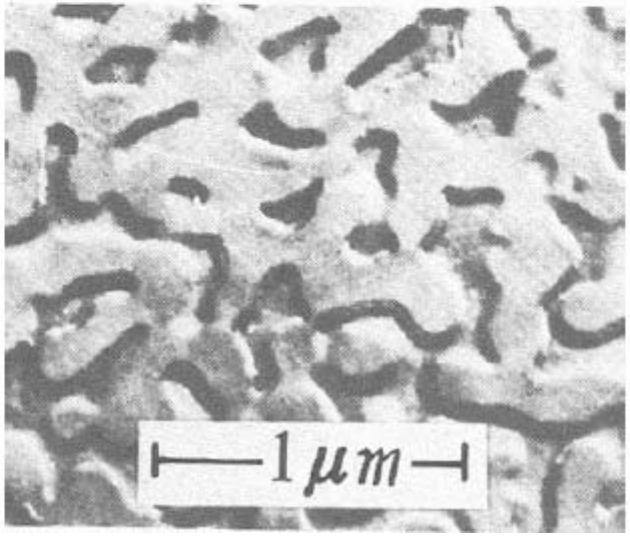

Metallic glass

(TEM)
TiYAlCo

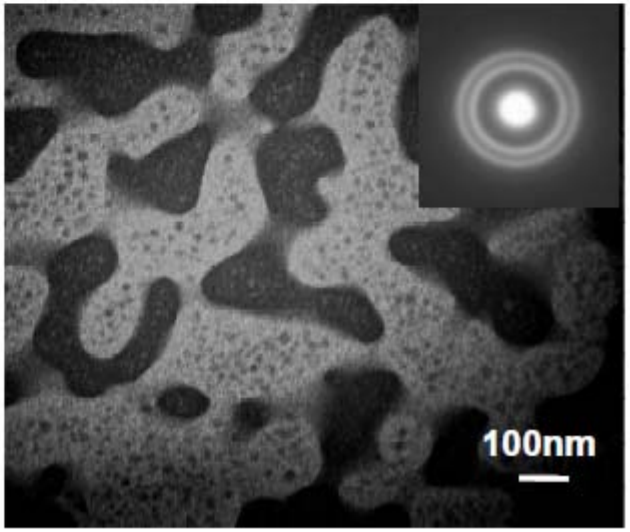

Annealing of Bulk Metallic Glasses: SR → SCLR (& PS) → Crystallization

5.7.3 Phase separation

* Miscibility gaps in phase separating system

- **Stable immiscibility**

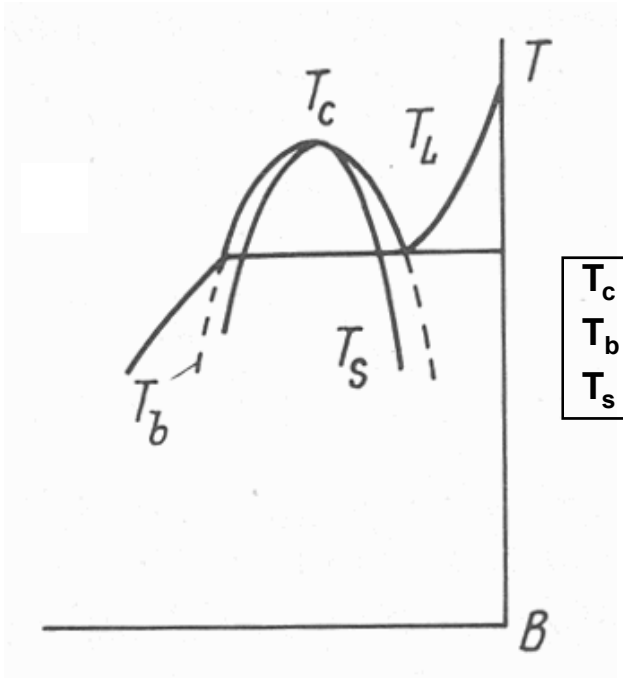

T_c : critical temperature
T_b : binodal curve
T_s : spinodal curve

- **Metastable immiscibility**

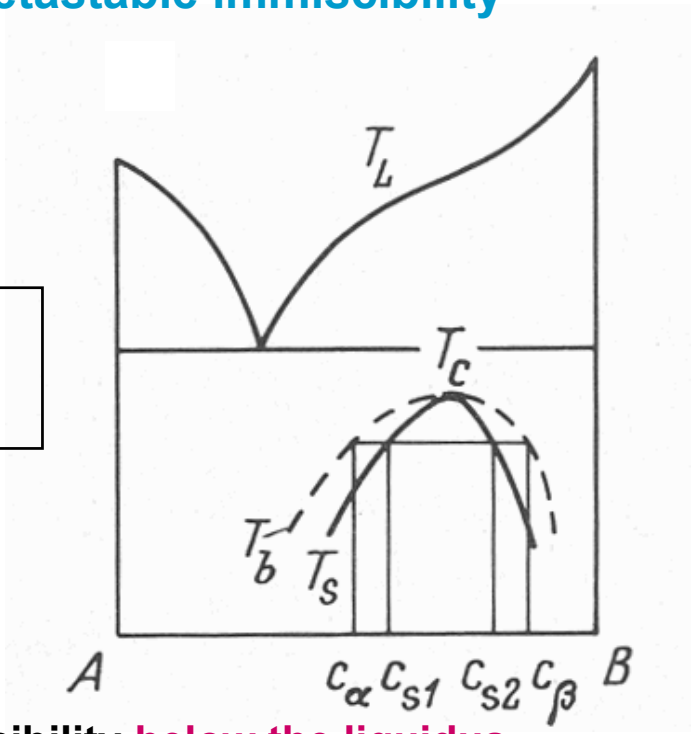

immiscibility **above the liquidus**

⇒ decomposition into stable liquid

immiscibility **below the liquidus**

⇒ decomposition into metastable liquid

"Phase separation in glass" ed. by Mazurin and Porai-Koshits (1984)

(a) Positive heat of mixing relation among constituent elements

- **Alloy design considering heat of mixing relation among constituent elements**

$\Delta H_{mix} \gg 0$ between A & B

⬇

creates (meta)stable miscibility gap in limited composition range

⬇

Phase separation to A-rich & B-rich phase

- **Different two-phase structure by initial composition before phase separation**

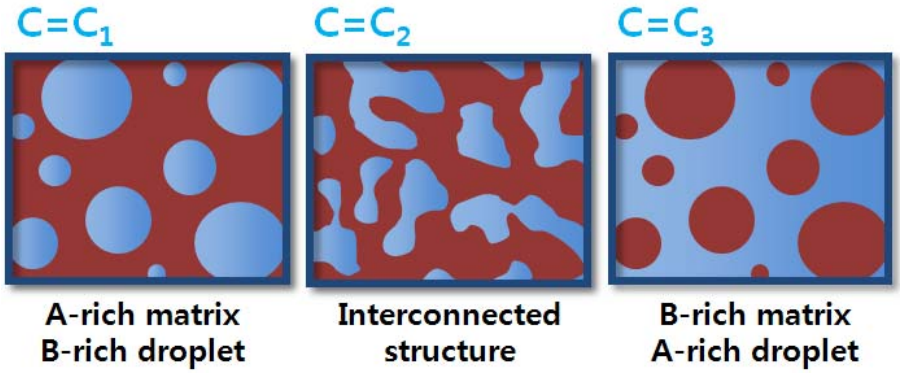

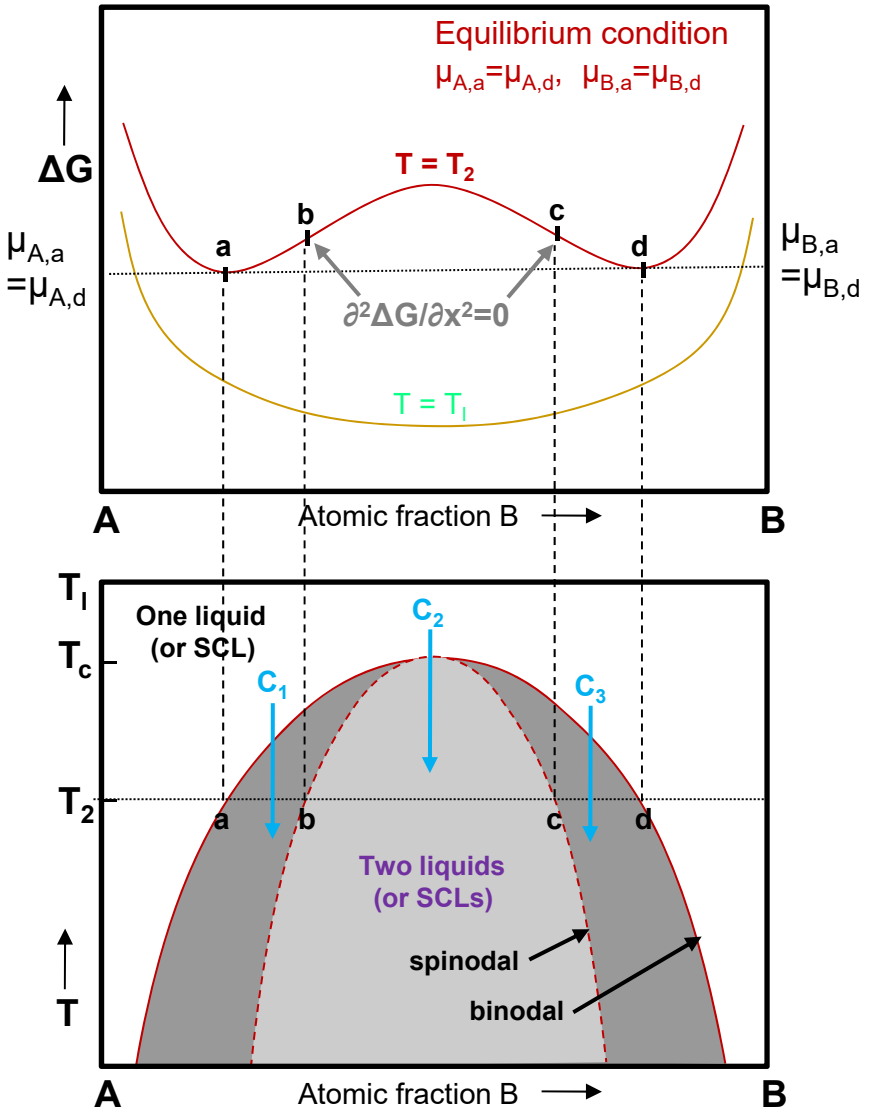

Nucleation and growth ↔ Spinodal decomposition without any barrier to the nucleation process

3D image construction process - $Gd_{30}Ti_{25}Al_{25}Co_{20}$

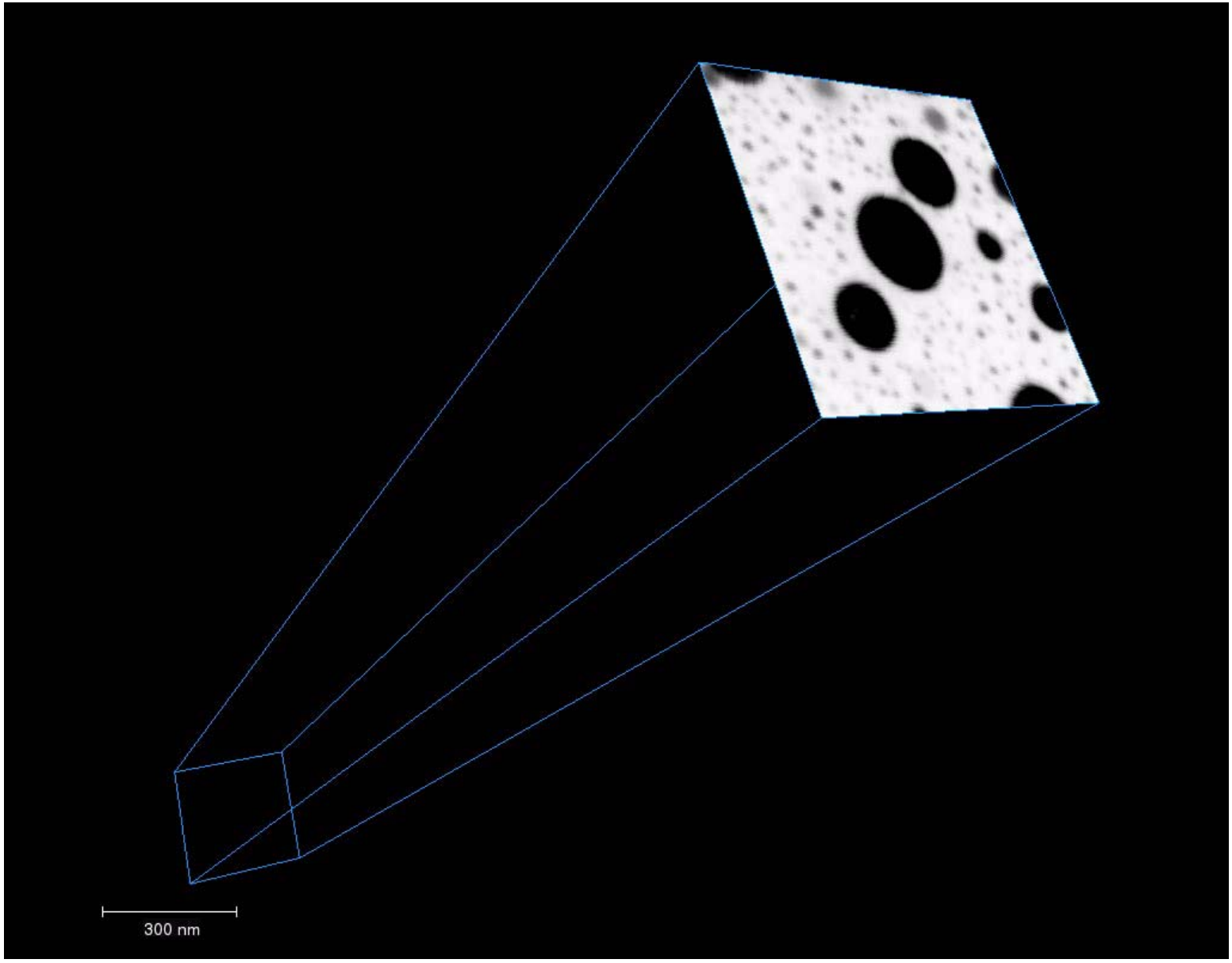

3D microstructure of phase separated metallic glass

Wheel side

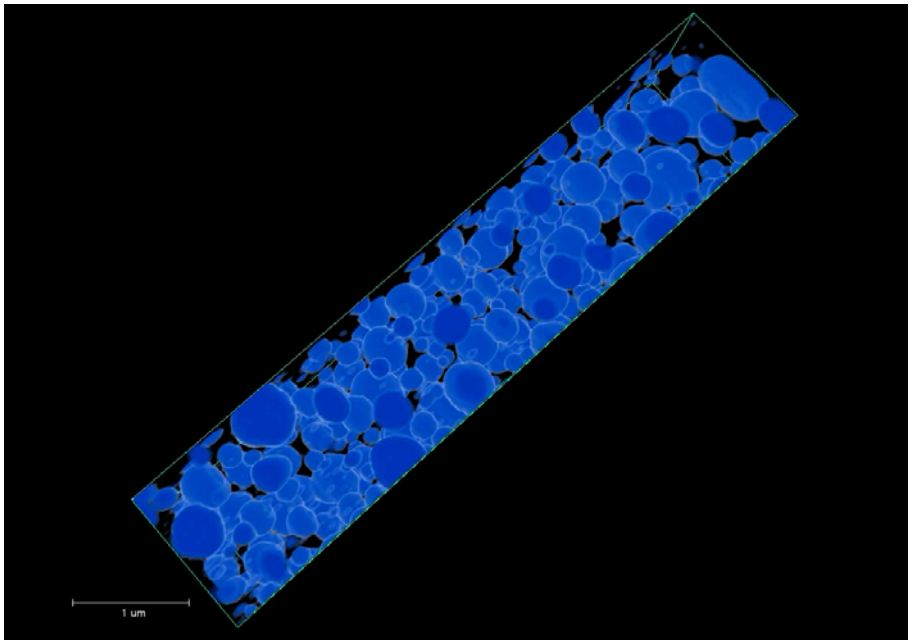

Free side

Volume fraction = 33.78%

Wheel side

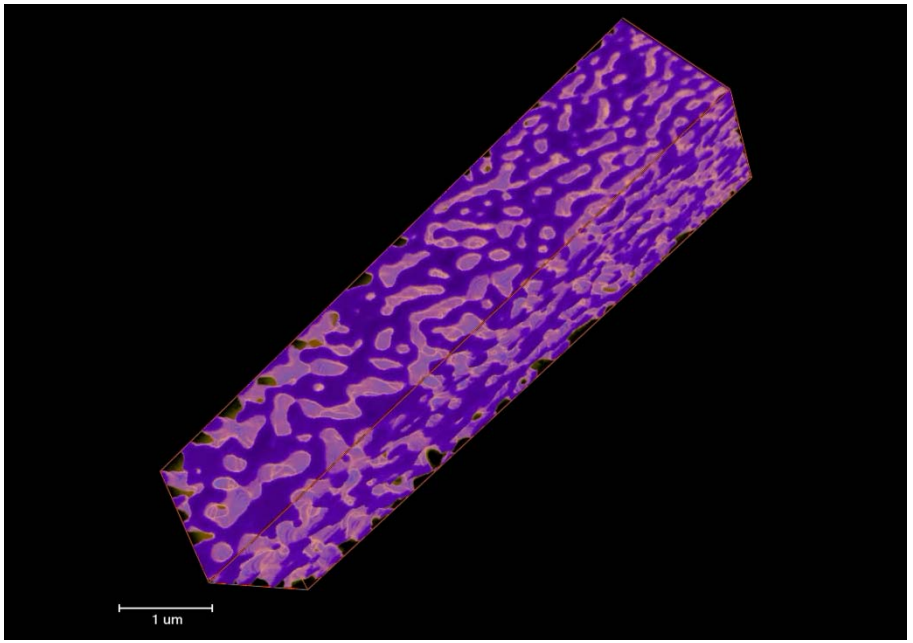

Free side

Volume fraction = 48.74%

It is possible to tailor the sizes of the glassy phases by varying the solidification rate during cooling.

5.5.5 Spinodal Decomposition

Spinodal mode of transformation has no barrier to nucleation

: describing the transformation of a system of two or more components in a metastable phase into two stable phases

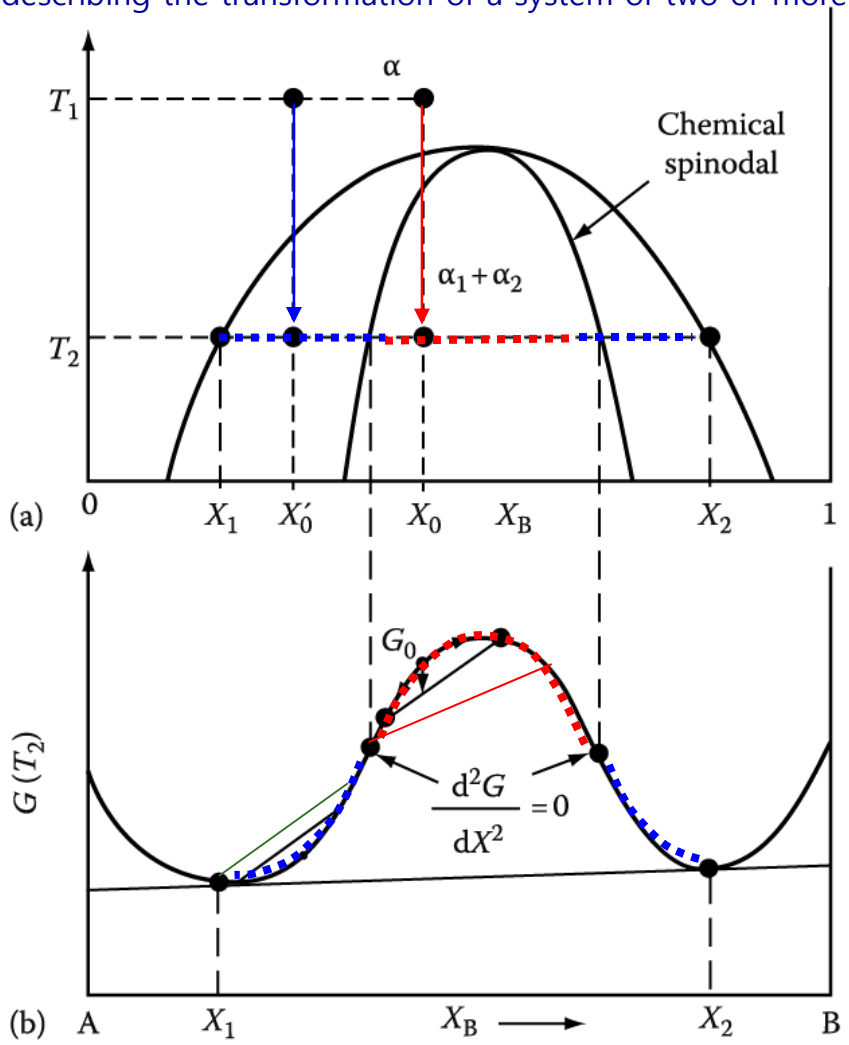

Fig. 5.38 Alloys between the spinodal points are unstable and can decompose into two coherent phasees α_1 and α_2 without overcoming an activation energy barrier. Alloys between the coherent miscibility gaps and the spinodal are metastable and can decompose only after nucleation of the other phase.

How does it differ between inside and outside the inflection point of Gibbs free energy curve?

1) Within the spinodal $\frac{d^2G}{dX^2} < 0$

: phase separation by small fluctuations in composition/ **"up-hill diffusion"**

2) If the alloy lies outside the spinodal, small variation in composition leads to an increase in free energy and the alloy is therefore metastable.

The free energy can only be decreased if nuclei are formed with a composition very different from the matrix.

→ nucleation and growth
: "down-hill diffusion"

a) Composition fluctuations within the spinodal

b) Normal down-hill diffusion outside the spinodal

up-hill diffusion

down-hill diffusion

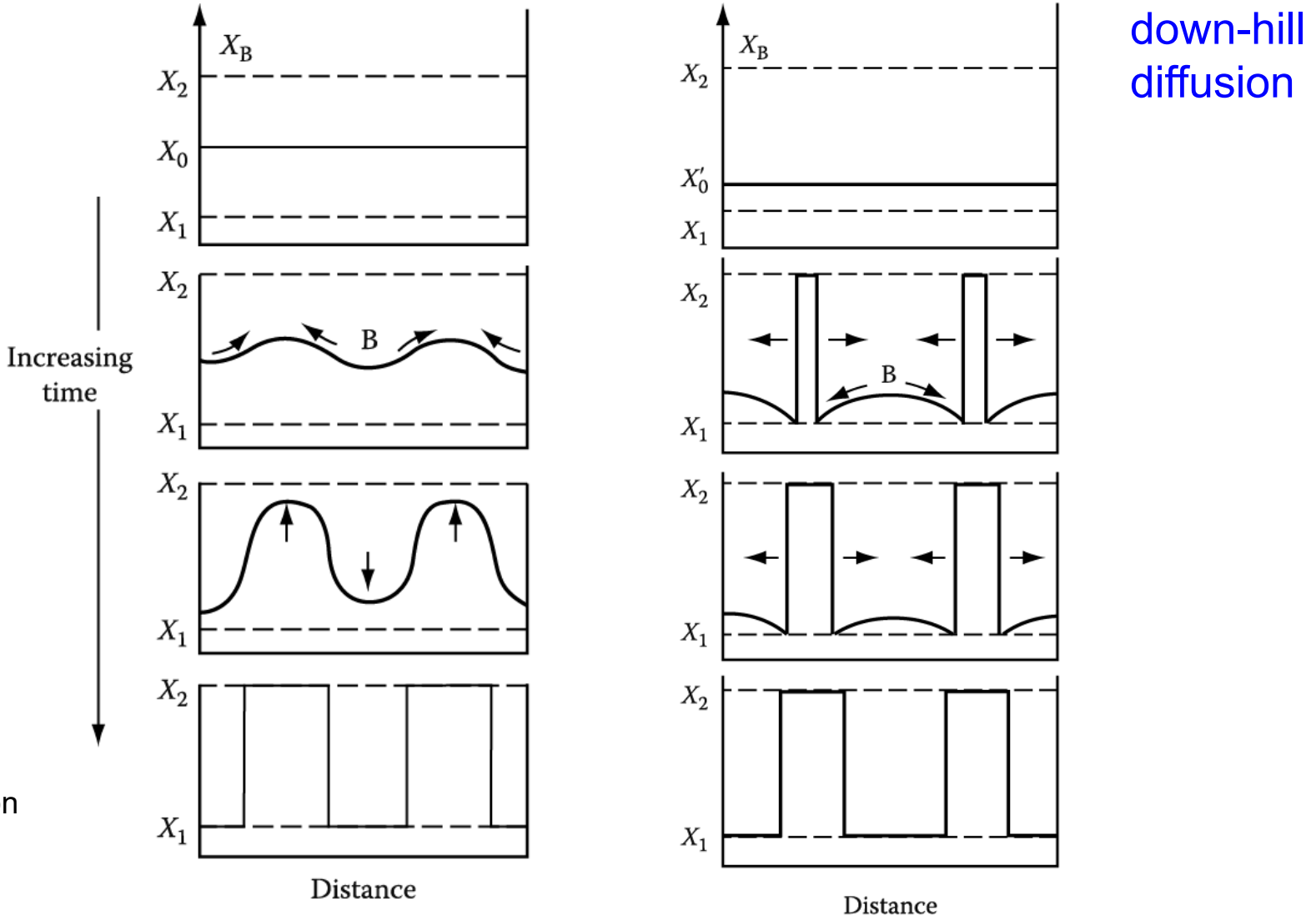

interdiffusion coefficient D<0

Fig. 5.39 & 5.40 schematic composition profiles at increasing times in (a) an alloy quenched into the spinodal region (X_0 in Figure 5.38) and (b) an alloy outside the spinodal points (X_0' in Figure 5.38)

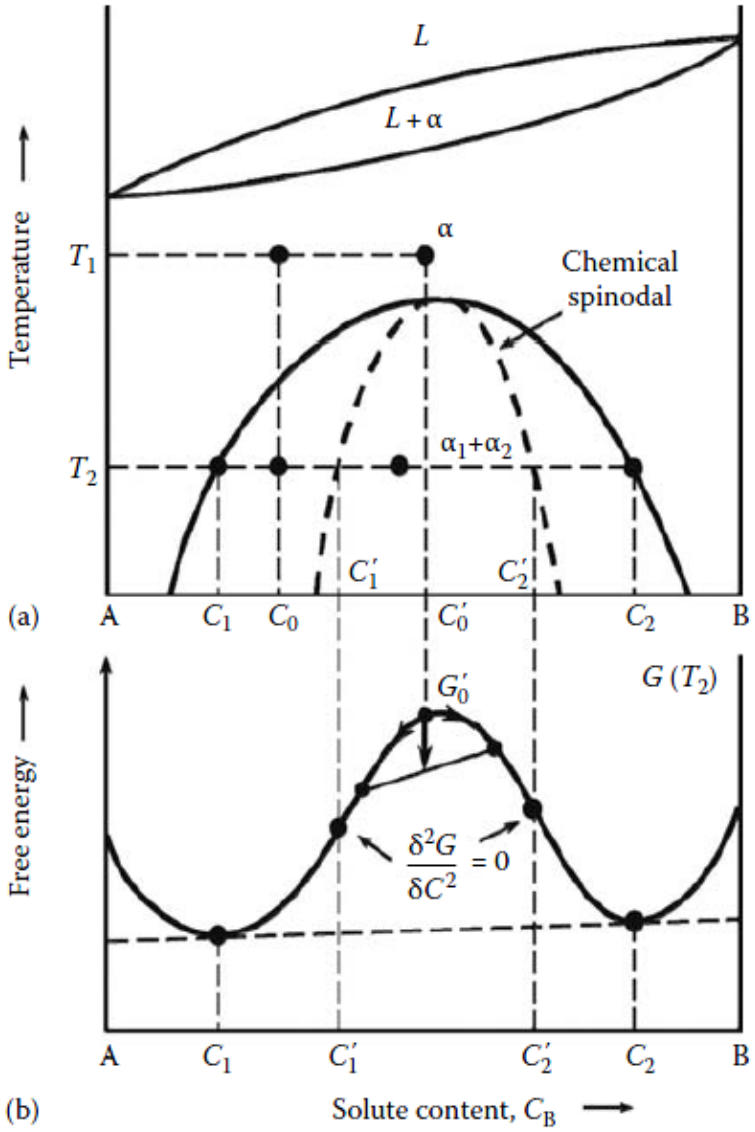

FIGURE 5.14
(a) Typical phase diagram showing a miscibility gap in the solid state. (b) The corresponding free-energy vs. composition diagram featuring two minima. Phase separation is possible in such an alloy system either by a nucleation and growth process or by a spinodal decomposition process.

TABLE 5.5

Alloy Systems Showing Phase Separation in the Glassy State

Alloy Composition	Synthesis Method	Characterization Method(s)	Compositions of the Two Glassy Phases	Comments	References
$Ag_{20}Cu_{48}Zr_{32}$	Melt spinning	TEM			[93]
$Cu_{43}Zr_{43}Al_7Ag_7$	Cu-mold casting	TEM and 3DAP	$Cu_{40.7}Zr_{46.8}Al_{8.0}Ag_{4.5}$ and $Cu_{36.8}Zr_{43.5}Al_{7.0}Ag_{12.7}$	Phase separation due to unusually high plastic strain	[94]
$Cu_{46}Zr_{22}Y_{25}Al_7$	Melt spinning	DSC and TEM	$Cu_{35.7}Zr_{12.8}Y_{44.3}Al_{7.2}$ and $Cu_{53.4}Zr_{31.8}Y_{8.3}Al_{6.5}$		[95]
$La_{27.5}Zr_{27.5}Al_{25}Cu_{10}Ni_{10}$	Melt spinning	SEM and TEM	$La_{5.0}Zr_{51.4}Cu_{5.4}Ni_{13.2}Al_{25}$ and $La_{43.4}Zr_{10.9}Cu_{14.4}Ni_{8.2}Al_{22.1}$		[96]
$Nd_{60-x}Zr_xAl_{10}Co_{30}$ $(6 \le x \le 40)$	Melt spinning	DSC and TEM			[97]
$Ni_{70}Nb_{15}Y_{15}$	Melt spinning	DSC, TEM, and SAXS			[98]
$Ni_{66}Nb_{17}Y_{17}$	Melt spinning	DSC, TEM, and SAXS			[98]
$Ni_{58.5}Nb_{20.25}Y_{21.25}$	Melt spinning	DSC, SEM, TEM, and SAXS	$Ni_{59}Nb_{16}Y_{25}$ and $Ni_{57}Nb_{28}Y_{15}$ by SEM and $Ni_{53}Nb_{42}Y_5$ and $Ni_{60}Nb_{10}Y_{30}$ by TEM	No two T_gs were observed	[98,99]
$Ni_{54}Nb_{23}Y_{23}$	Melt spinning	DSC, TEM, and SAXS	$Ni_{50}Nb_{44}Y_6$ and $Ni_{58}Nb_7Y_{35}$		[98]
$Ni_{61}Zr_{28-x}Nb_7Al_4Ta_x$ $(x=0, 2, 4, 6, 8)$	Melt spinning			No evidence of phase separation	[100]
$Pd_{80}Au_{3.5}Si_{16.5}$	Roller quenching	DSC and SAXS		Apparent phase separation	[31]
$Pd_{78}Au_6Si_{16}$	Splat cooling	DSC and TEM	Segregation into (Pd–Au)-rich and Si-rich glassy phases	No clear identification of the phases	[30]
$Pd_{40.5}Ni_{40.5}P_{19}$	Centrifugal spinning	DSC		Two T_gs were observed only after the original glassy sample was heated beyond the first exothermic peak, then cooled quickly and reheated	[34]

TABLE 5.5 (continued)

Alloy Systems Showing Phase Separation in the Glassy State

Alloy Composition	Synthesis Method	Characterization Method(s)	Compositions of the Two Glassy Phases	Comments	References
$Pd_{80}Si_{20}$	Splat cooling	DSC and TEM	Pd-rich particles embedded in a Si-rich matrix	No clear identification of the phases	[30]
$Ti_{28}Y_{28}Al_{24}Co_{20}$	Melt spinning	XRD and TEM	$Y_{40.4}Ti_{14.7}Al_{21.9}Co_{23}$ and $Ti_{45.6}Y_{11.6}Al_{26.7}Co_{16.1}$	No clear T_g in DSC	[101]
$Ti_{56-x}Y_xAl_{22}Co_{22}$ ($x = 11$, 20, or 28)	Melt spinning	TEM	$Y_{44.5}Ti_{8.8}Al_{36.9}Co_{9.8}$ and $Ti_{47.2}Y_{2.1}Al_{19.9}Co_{30.8}$. These compositions depend on the initial composition of the alloy.		[102]
$Zr_{63.8}Ni_{16.2}Cu_{15}Al_5$	Cu-mold casting		$Zr_{68.5}Cu_{8.1}Ni_{21.3}Al_{2.1}$ and $Zr_{62.4}Cu_{16.7}Ni_{14.6}Al_{6.3}$	Noted 30% plastic strain during compression at room temperature	[103]
$Zr_{36}Ti_{24}Be_{40}$	Melt spinning	DSC and TEM		Two T_gs were reported. Nagahama et al. [104] concluded that this alloy crystallized in a eutectic mode and that there was no phase separation	[89]
$Zr_{52.5}Ti_5Cu_{17.9}Ni_{14.6}Al_{10}$ (Vit 105)	Cu-mold casting and Melt spinning	SANS and TEM		Phase separation? Kajiwara et al. [106] suggested primary crystallization	[105]
$Zr_{41.2}Ti_{13.8}Cu_{12.5}Ni_{10.0}Be_{22.5}$ (Vit 1)	Water quenching	DSC, SANS, TEM and APFIM	Zr-rich and Be-rich phases		[107–109]
$Zr_{28}Y_{28}Al_{22}Co_{22}$	Melt spinning	Dynamic Mechanical Analysis and TEM	$Y_{30.9}Zr_{26.0}Al_{24.8}Co_{18.3}$ and $Zr_{36.4}Y_{15.8}Al_{28.8}Co_{19.0}$	Phase separation observed during heating of a homogeneous glassy phase	[110]
$Zr_{60-x}Y_xAl_{15}Ni_{25}$ ($x = 15$, 27, and 45)	Melt spinning	DSC		Two supercooled liquid regions	[111]

a. Phase separation in solid state

- Pd-Si-Ag alloy / two amorphous phase formation after heating just above T_g

Chen and Turnbull, Acta Metall., 17, 1021 (1969)

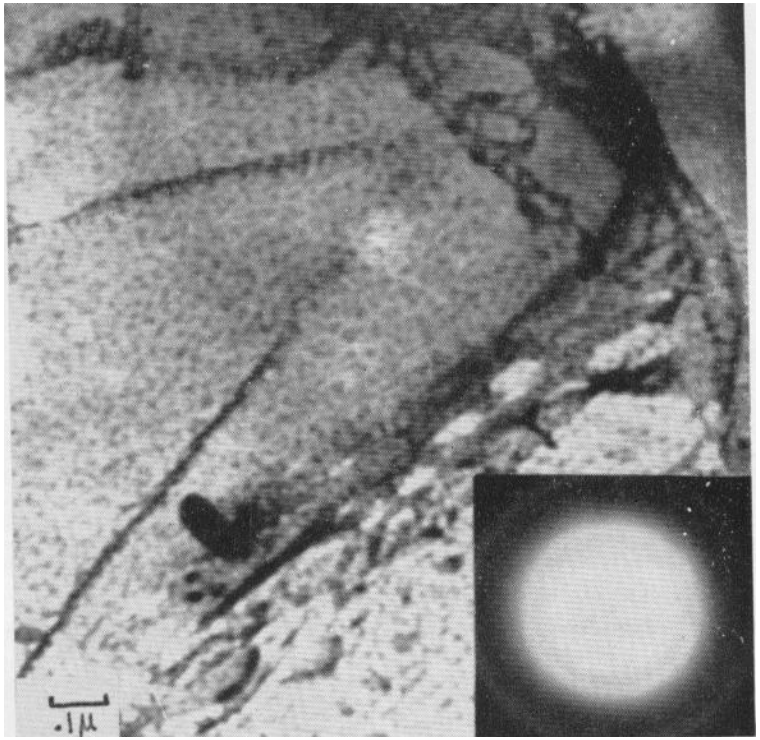

- After heating just above T_g, two amorphous separation occurs, but crystallization occurs simultaneously.

- Zr-Ti-Cu-Ni-Be BMG / small angle neutron scattering

Schneider et al, Appl. Phys. Lett., 68, 493 (1996)

decomposed during cooling in the liquid state to a two-phase mixture of Be-rich and Zr-rich glassy regions with a typical length scale of tens of nanometers

Martin et al., Acta Mater., 52, 4427 (2004)

Ti-rich and Be-depleted regions that appeared in the early stage of annealing due to the partitioning of alloying elements accompanied by the crystallization reaction.

* Zr-Y-Al-Ni system: homogeneous glassy phase in the as-quenched state had transformed into a mixed structure consisting of the Zr-rich Zr-Al-Ni glassy phase and the Y-rich Y-Al-Ni crystalline phase (3-5 nm).

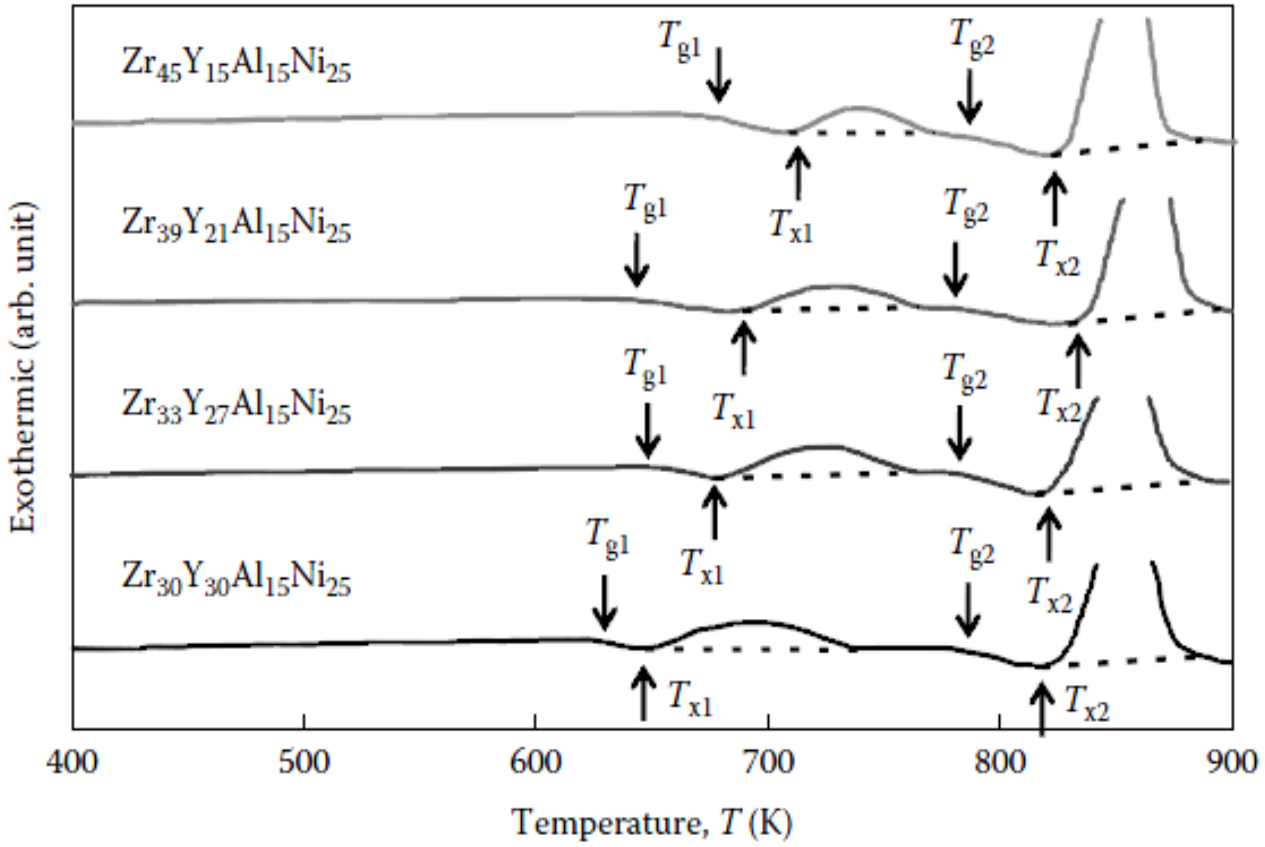

FIGURE 5.15
DSC curves of the glassy $Zr_{60-x}Y_xAl_{15}Ni_{25}$ (x=15, 21, 27 and 30) alloys obtained at a heating rate of 0.67 K s^{-1}(40 K min^{-1}). Note the presence of two T_gs and two T_xs in all the alloys studied. (Reprinted from Inoue, A. et al., *Mater. Sci. Eng. A*, 179/180, 346, 1994. With permission.)

* Zr-Y-Al-Ni system: exhibit two glass transition temperature

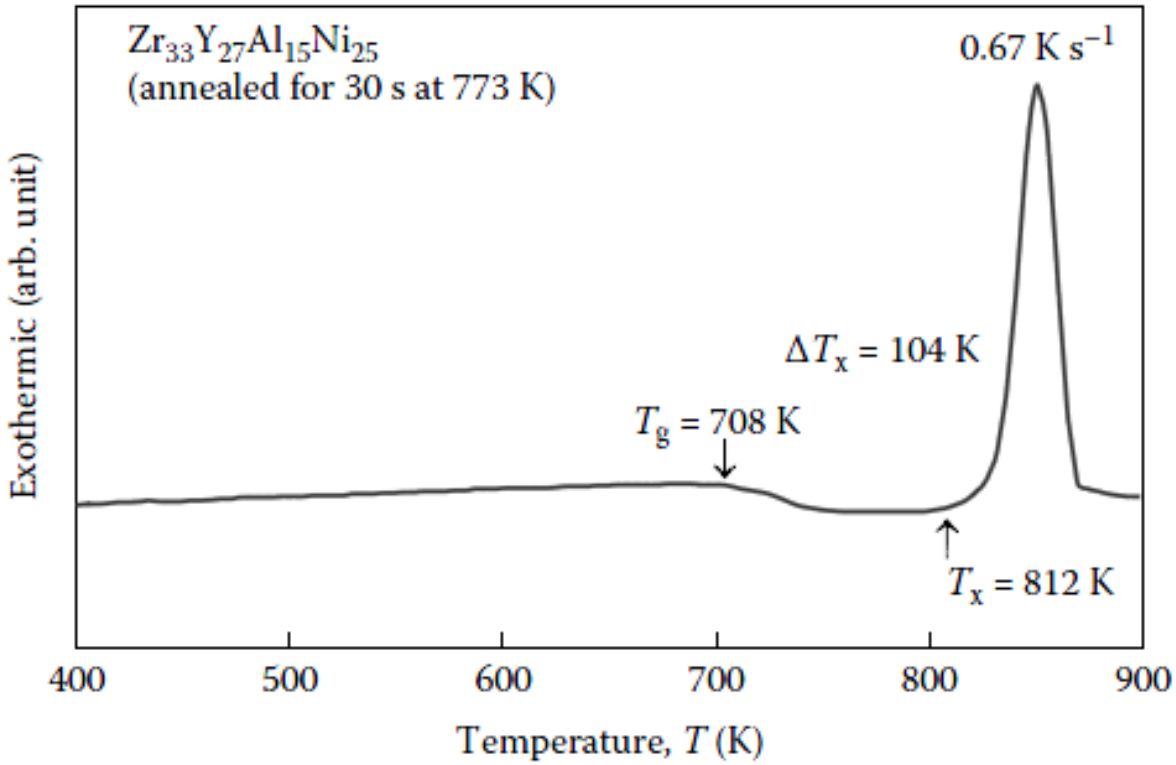

FIGURE 5.16
DSC curve of the glassy $Zr_{33}Y_{27}Al_{15}Ni_{25}$ alloy pre-annealed for 30 s at 773 K. The width of the supercooled liquid region, ΔT_x (= $T_x - T_g$), has now increased to 104 K from 40 K in the as-solidified condition. (Reprinted from Inoue, A. et al., *Mater. Sci. Eng. A*, 179/180, 346, 1994. With permission.)

b. Phase separation in liquid state

* La-Zr-Al-Cu-Ni system

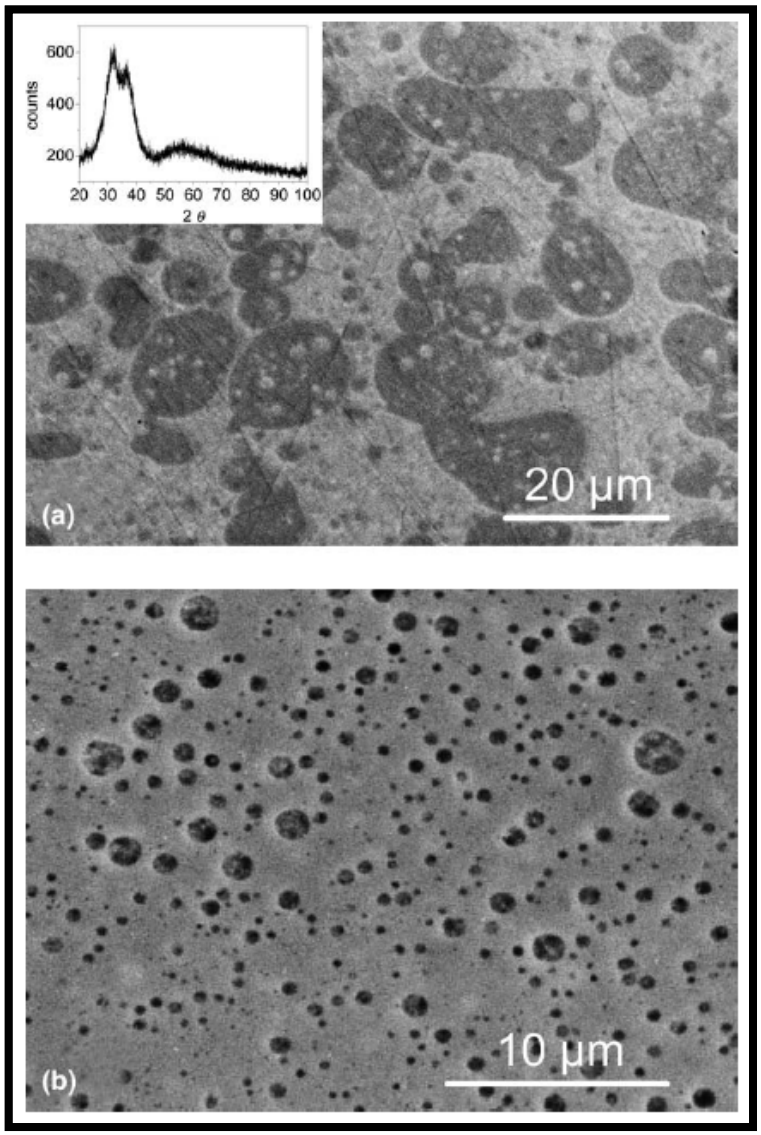

Kundig et al., *Acta Mat.*, 52 (2004) 2441-2448.

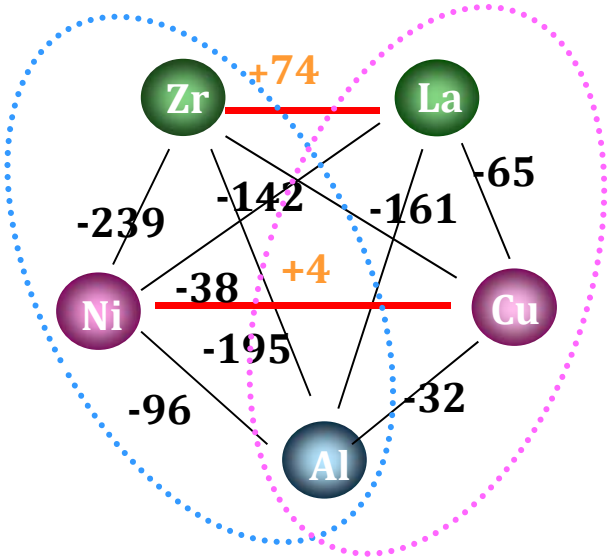

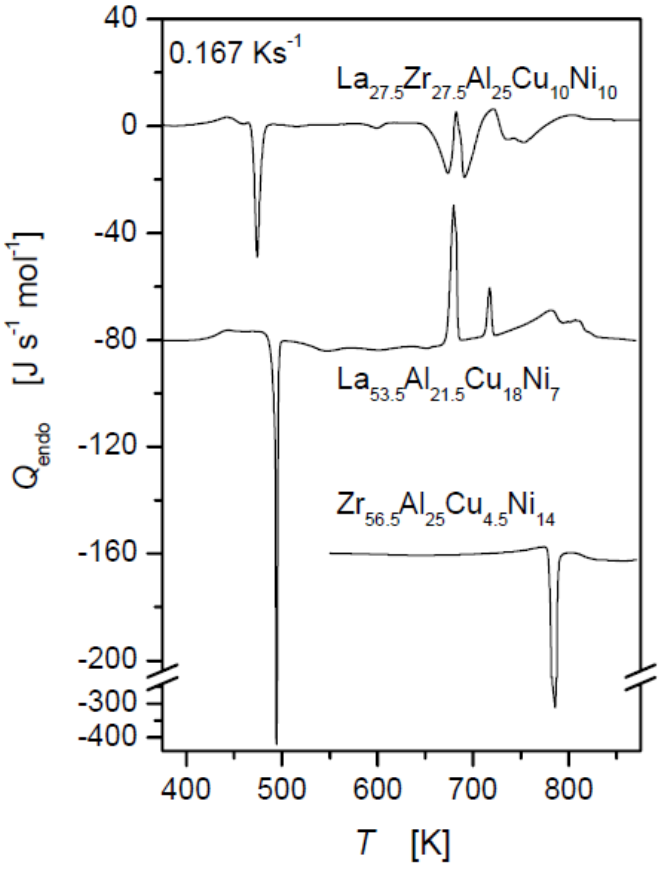

* La-Zr-Al-Cu-Ni system

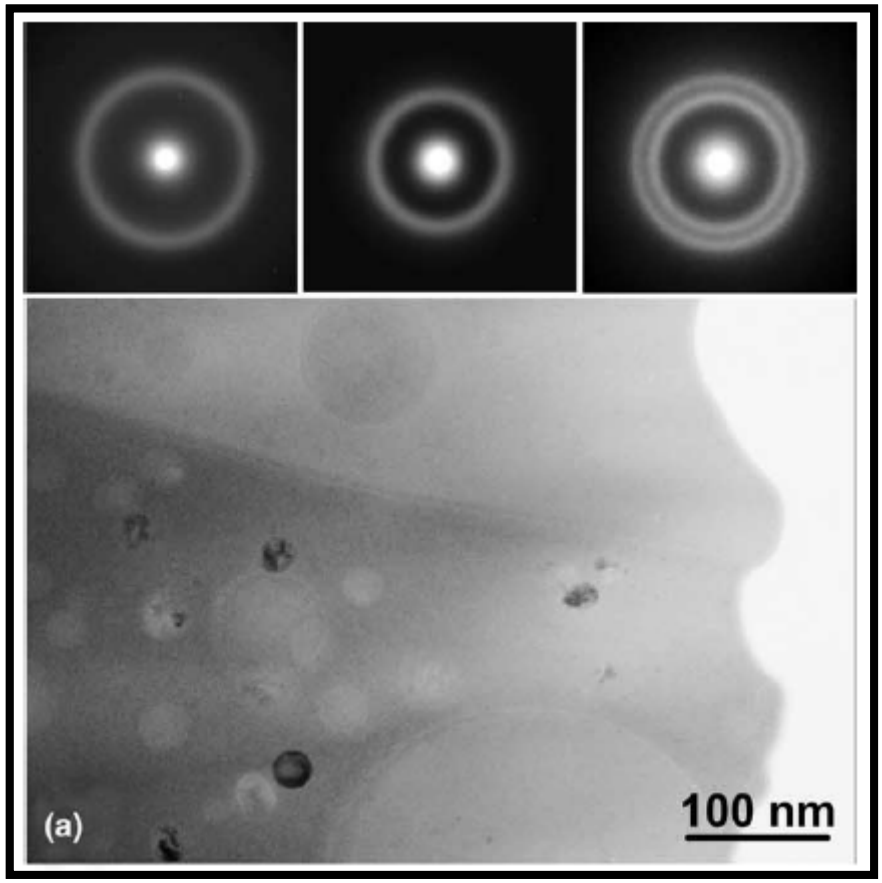

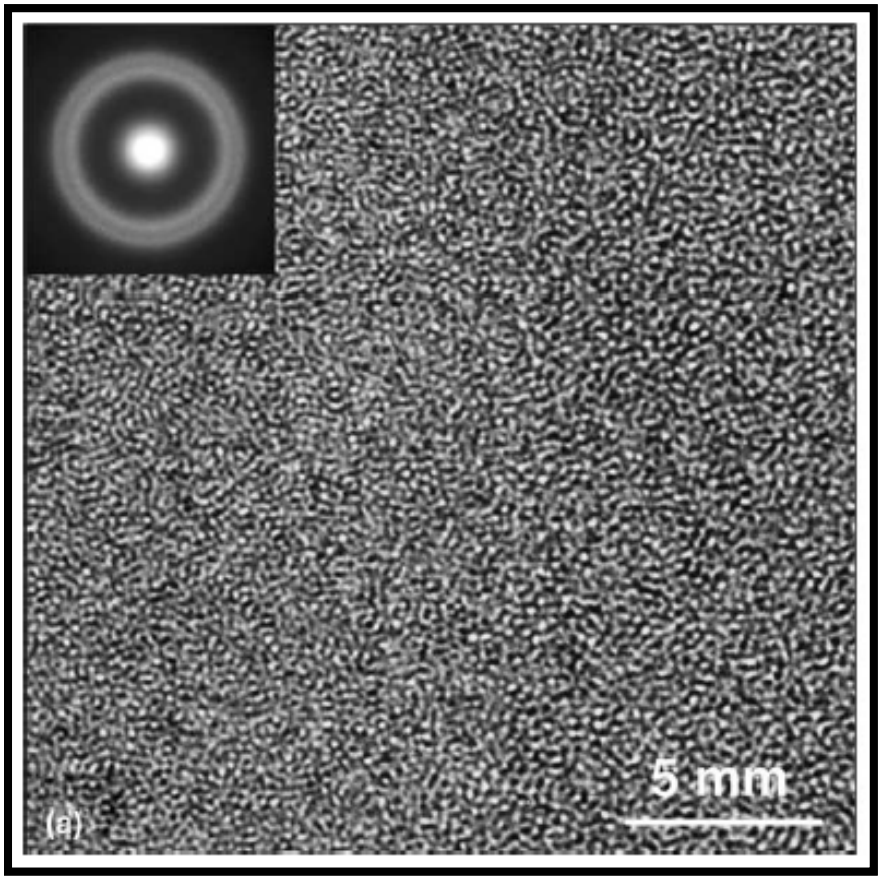

Kundig et al., *Acta Mat.*, 52 (2004) 2441-2448.

* La-Zr-Al-Cu-Ni system

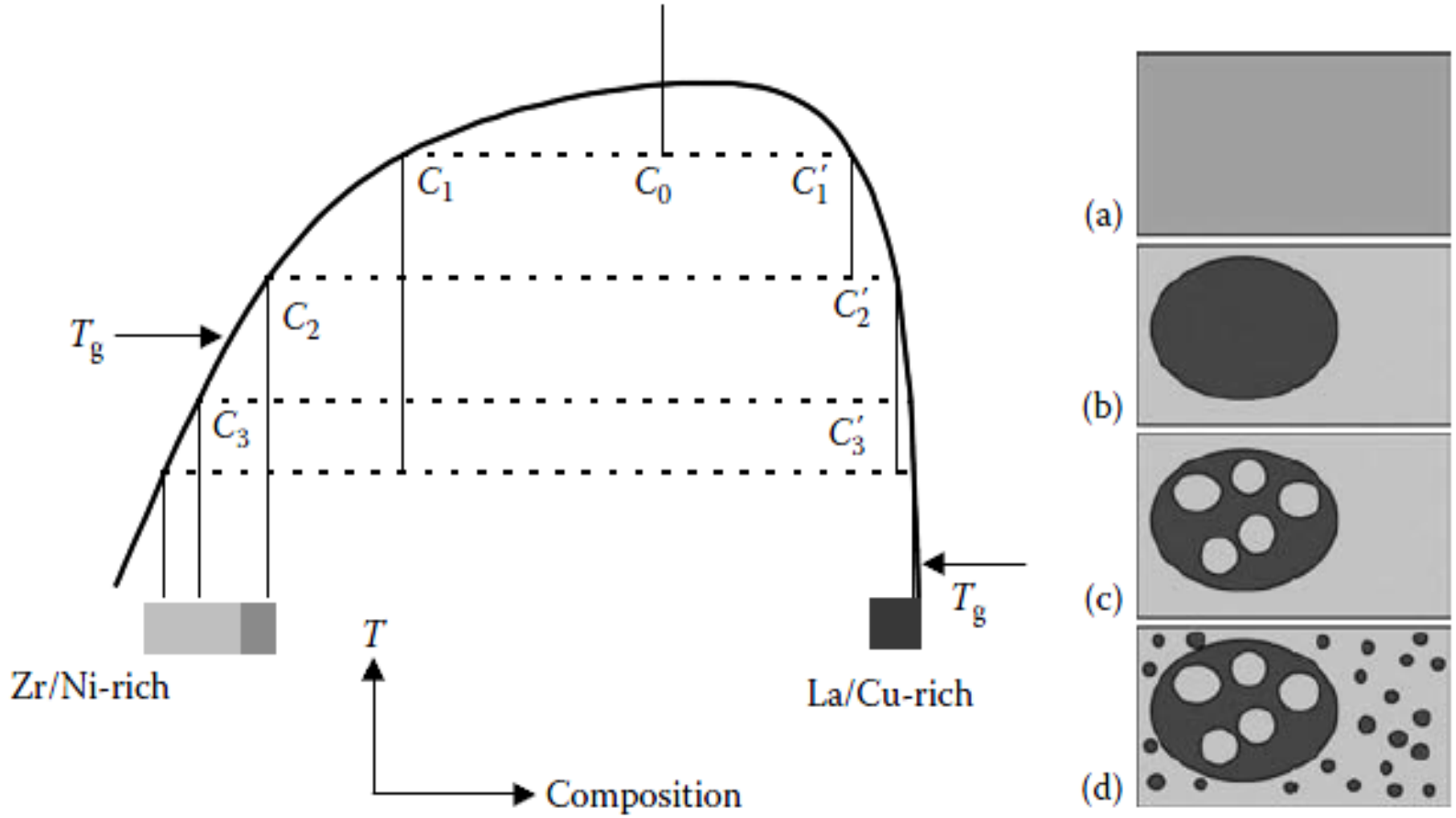

FIGURE 5.17
Schematic of the miscibility gap and the sequence of phase formation during cooling in the La–Zr–Al–Cu–Ni system. The positions of letters (a) to (d) in the diagram on the left correspond to the schematic microstructures (a) to (d) on the right. (Reprinted from Kündig, A.A. et al., *Acta Mater.*, 52, 2441, 2004. With permission.)

Shell/Yard region in phase separated structure

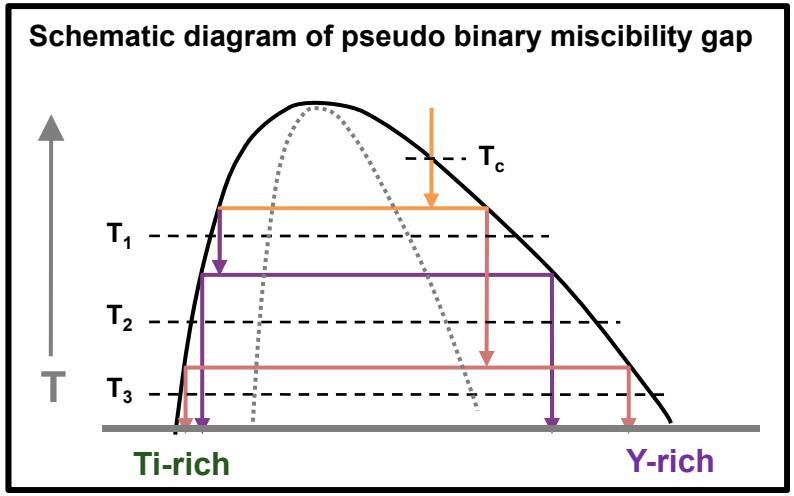

- Yard : Secondary phase-free region

  Shell : The layer enveloping primary phase by wetting

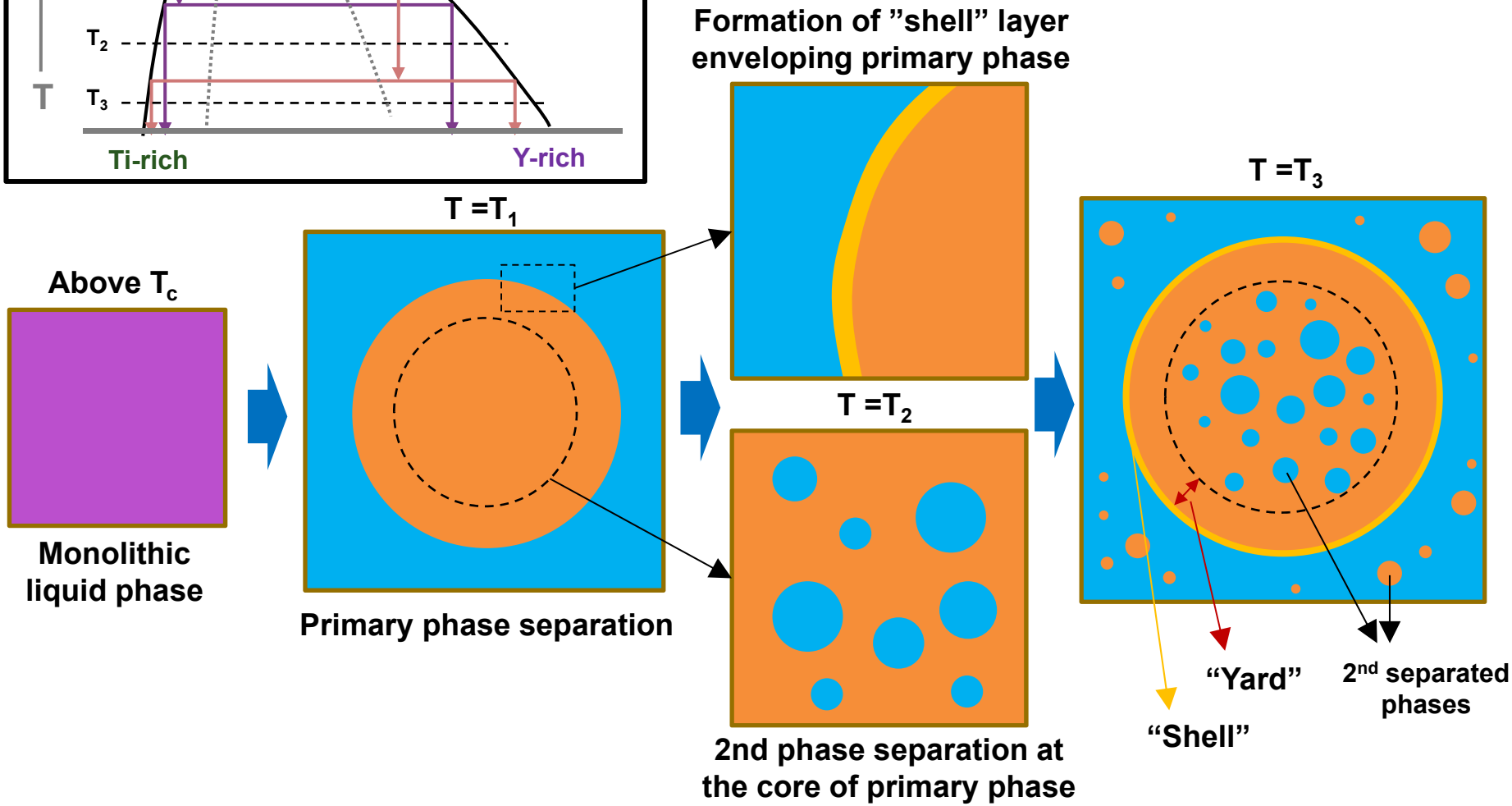

* Ti-Y-Al-Co system → $Ti_{24}Y_{18}La_{18}Al_{22}Co_{18}$ three different glassy phase

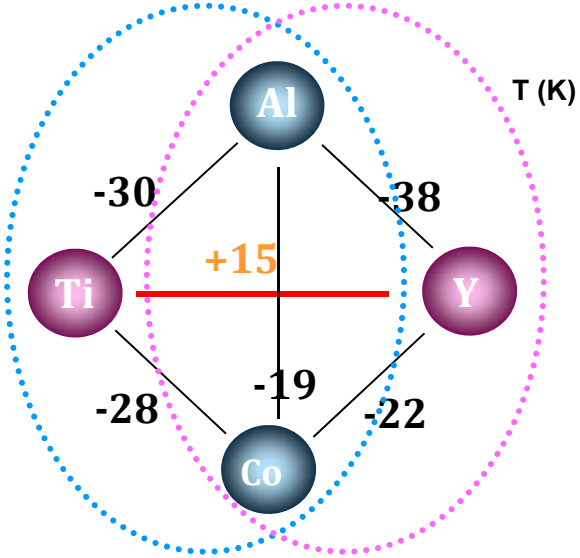

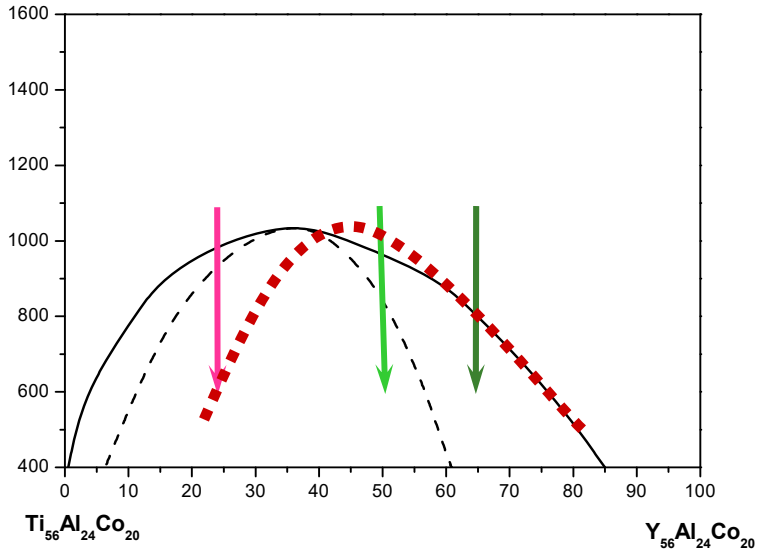

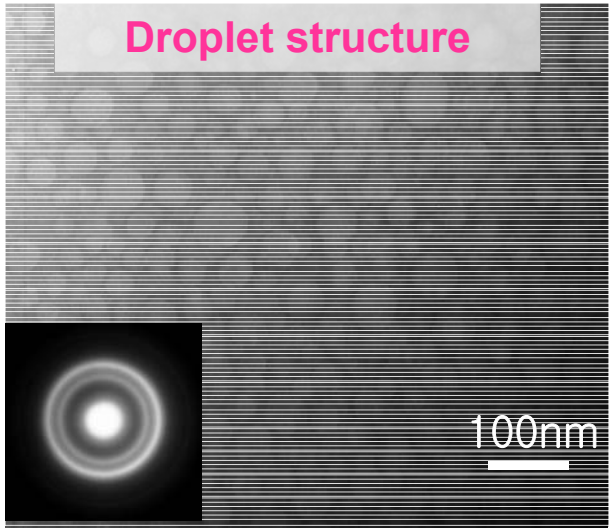

$(Y_{56}Al_{24}Co_{20})_{25}(Ti_{56}Al_{24}Co_{20})_{75}$

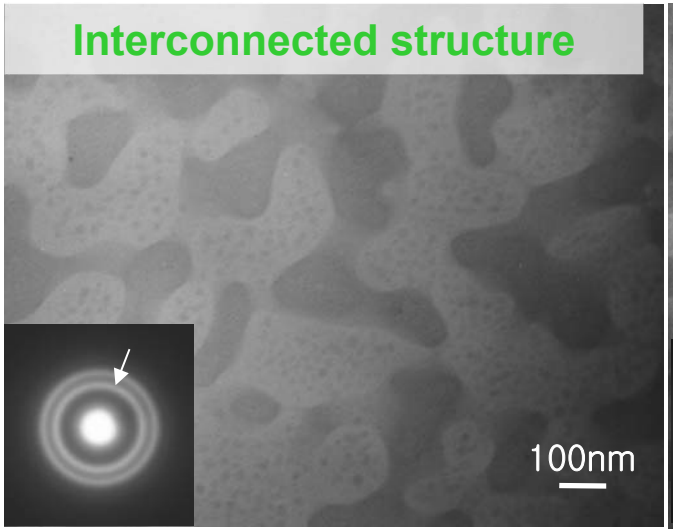

$(Y_{56}Al_{24}Co_{20})_{50}(Ti_{56}Al_{24}Co_{20})_{50}$

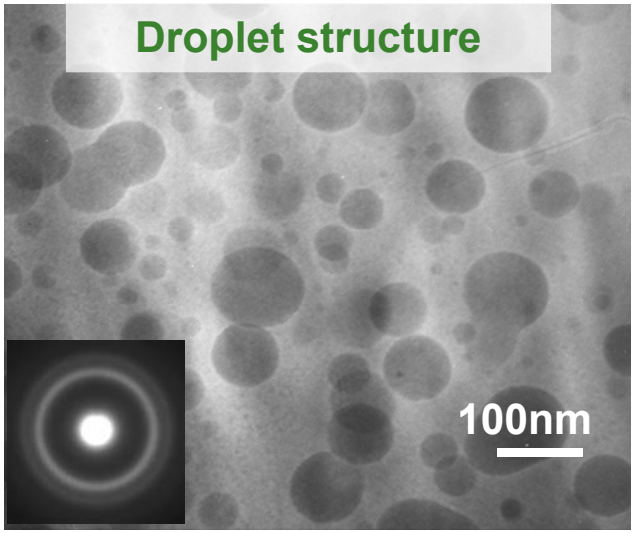

$(Y_{56}Al_{24}Co_{20})_{65}(Ti_{56}Al_{24}Co_{20})_{35}$

* Ti-Y-Al-Co system

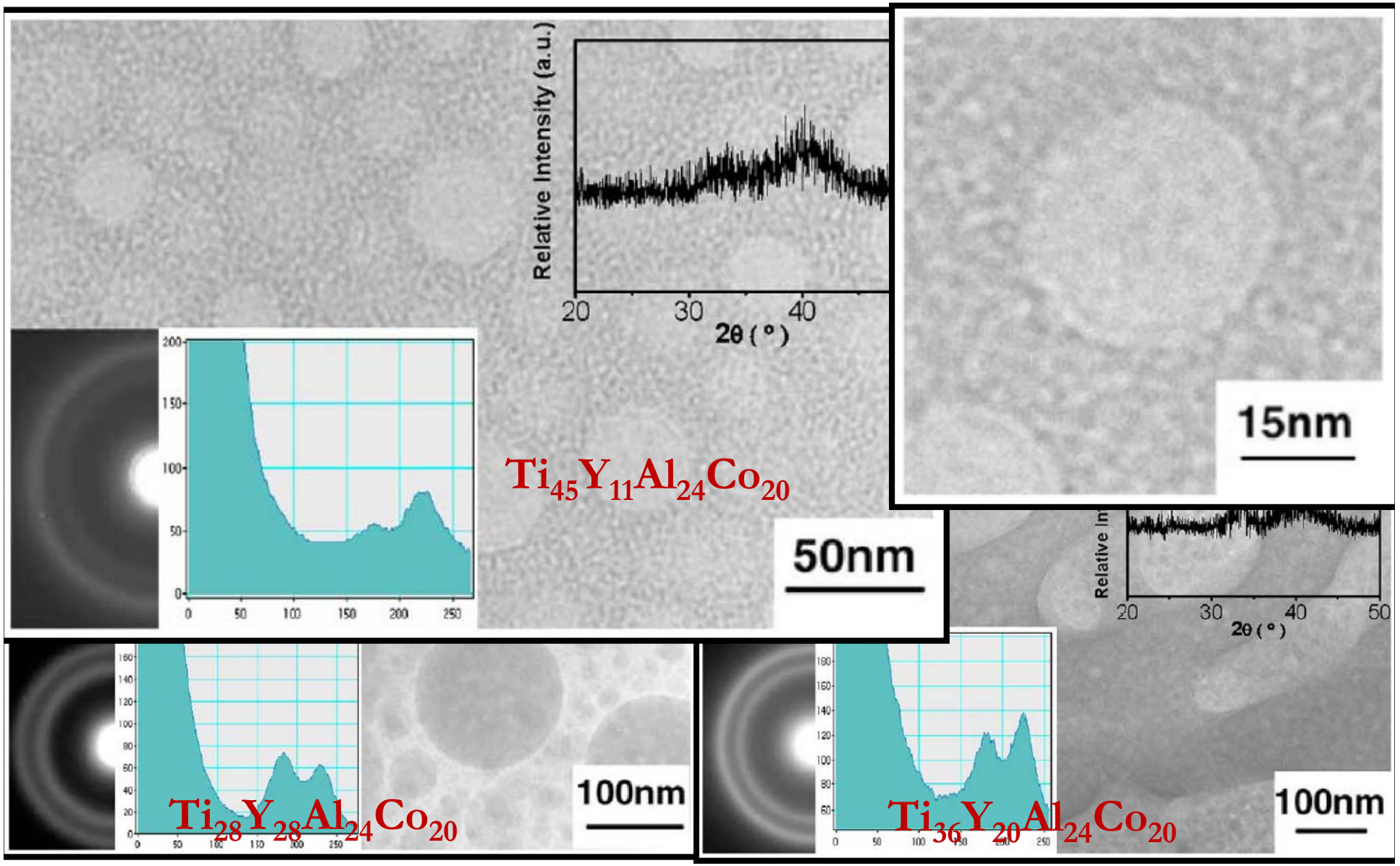

B.J.Park et al., *Appl. Phys. Lett.*. 85 (2004) 6353.
Phys. Rev. Lett., 96 (2006) 245503.

* Ni-Nb-Y system

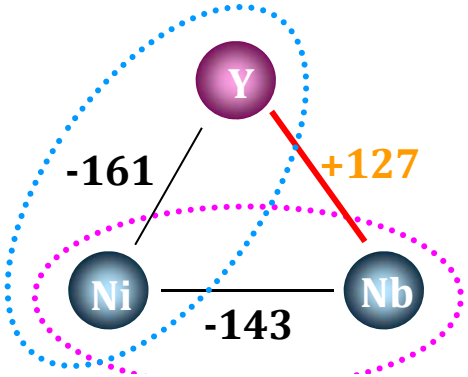

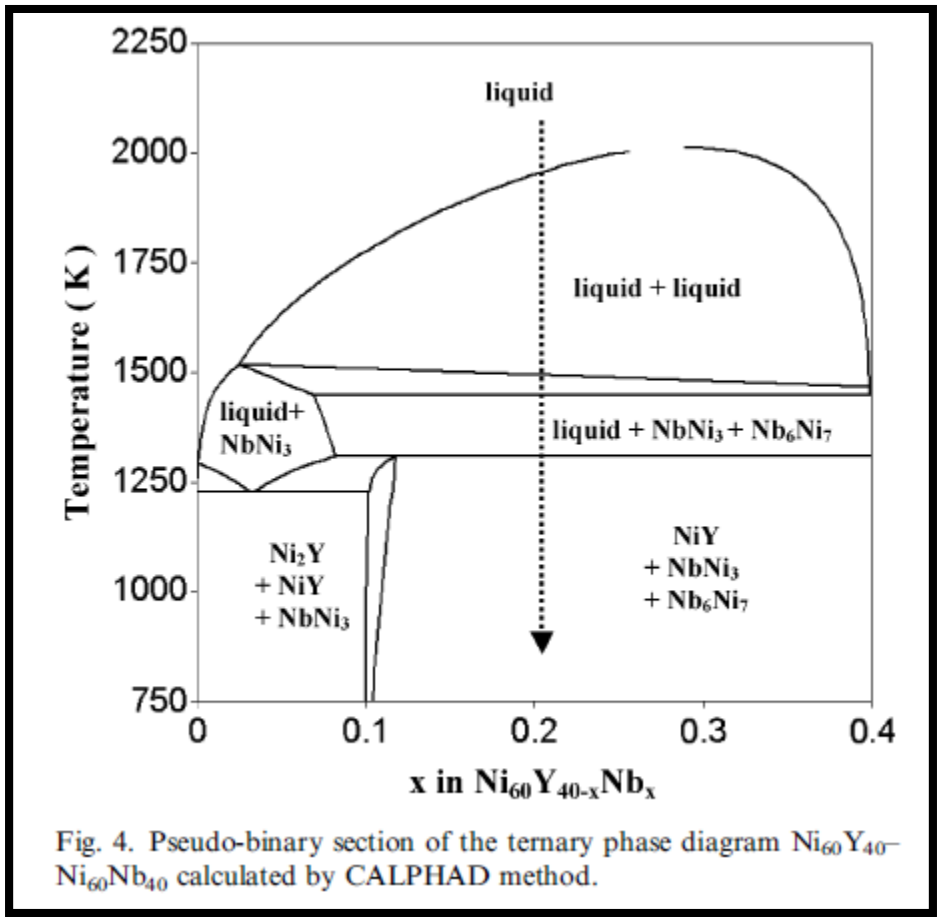

Fig. 4. Pseudo-binary section of the ternary phase diagram $Ni_{60}Y_{40}$–$Ni_{60}Nb_{40}$ calculated by CALPHAD method.

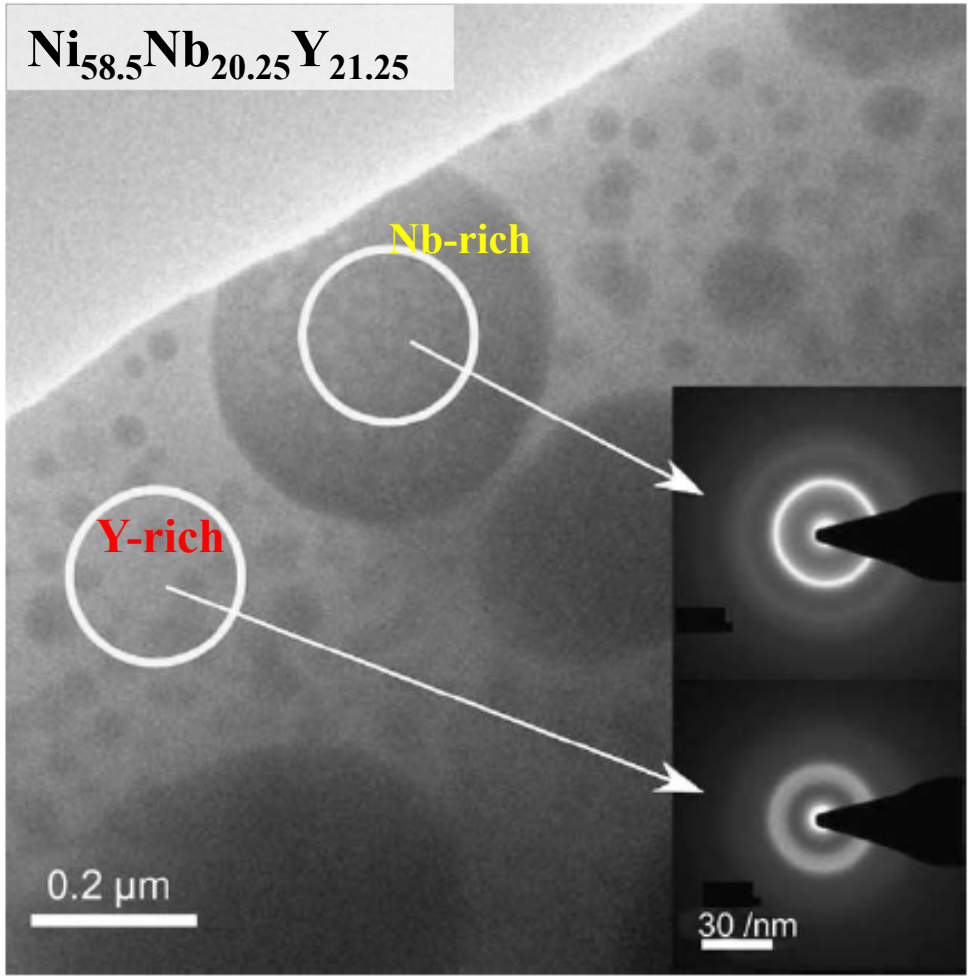

Mattern et al., *Scripta Mat.* 53 (2005) 271.
Mat. Sci. Eng. A, 449-451 (2007) 207.

Microstructure determining parameters of phase separation in metallic glasses

- ❖Composition
- ❖Glass-forming ability of the separated liquid
- ❖Critical temperature
- ❖Asymmetry of the spinodal curve / Decomposition range

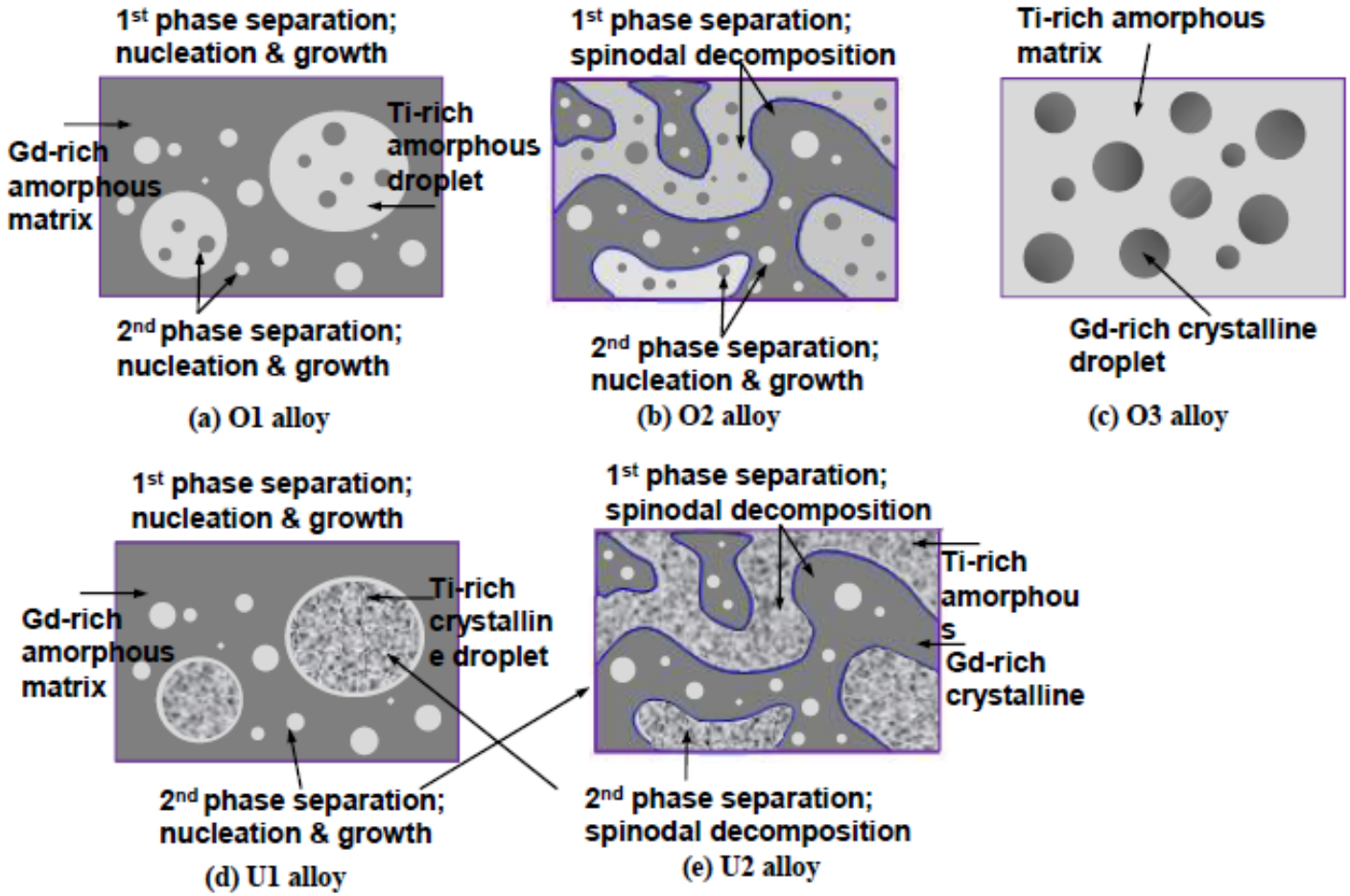

Thermodynamic calculation using CALPHAD

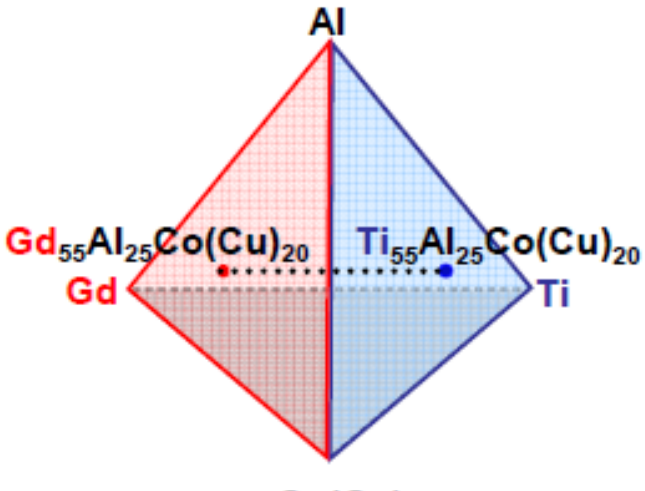

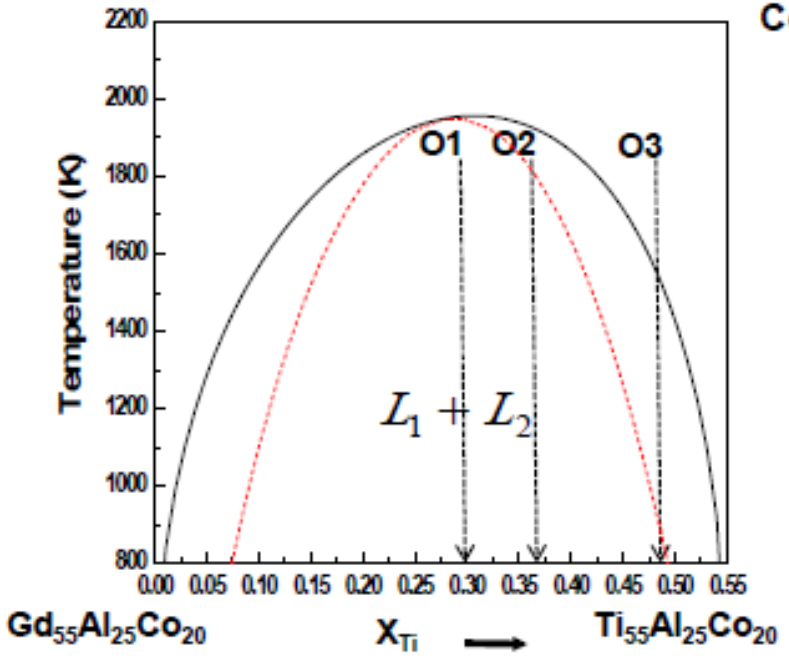

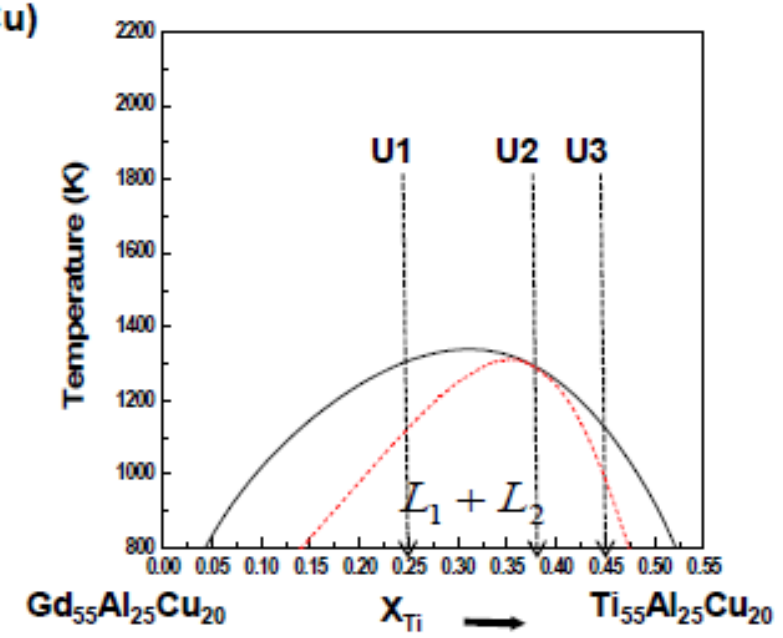

Microstructure evolution (GdTiAlCo)

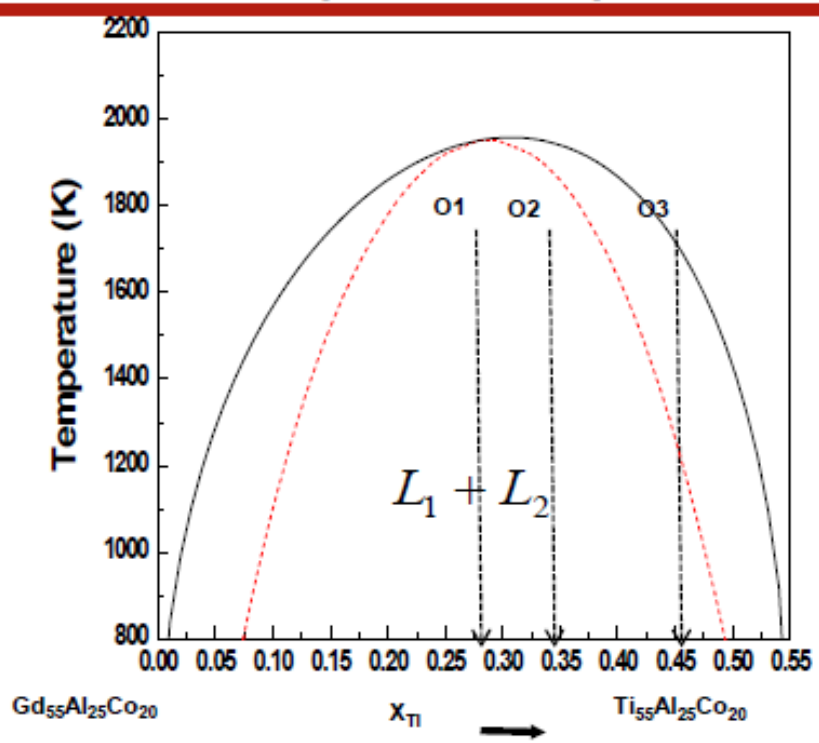

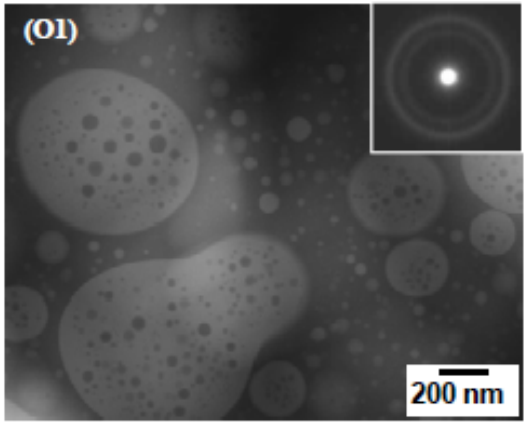

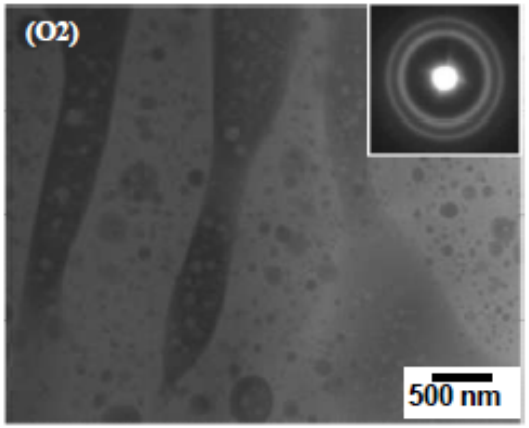

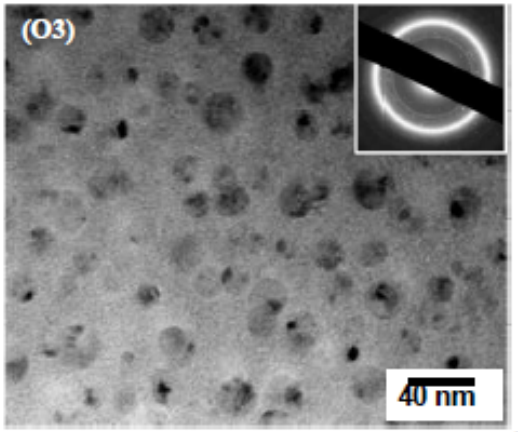

Chang et al., Acta Mater (2010)

Microstructure evolution (GdTiAlCu)

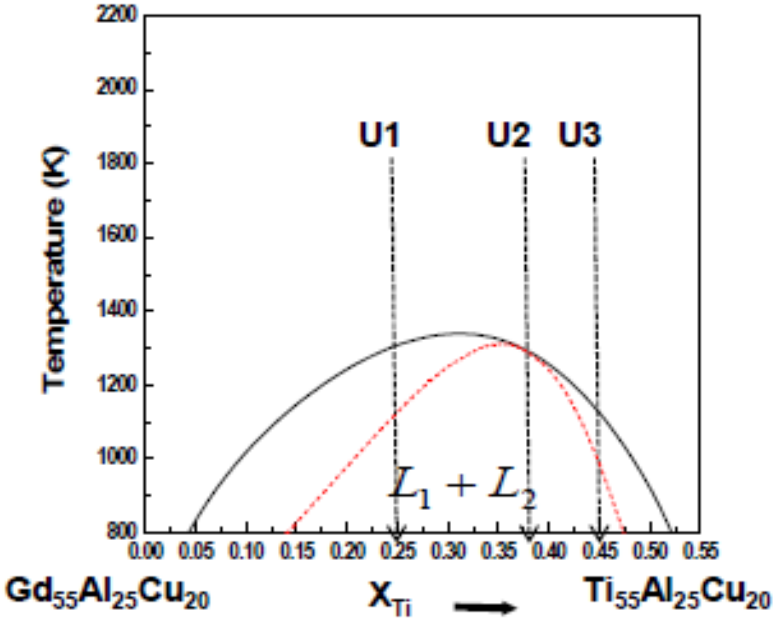

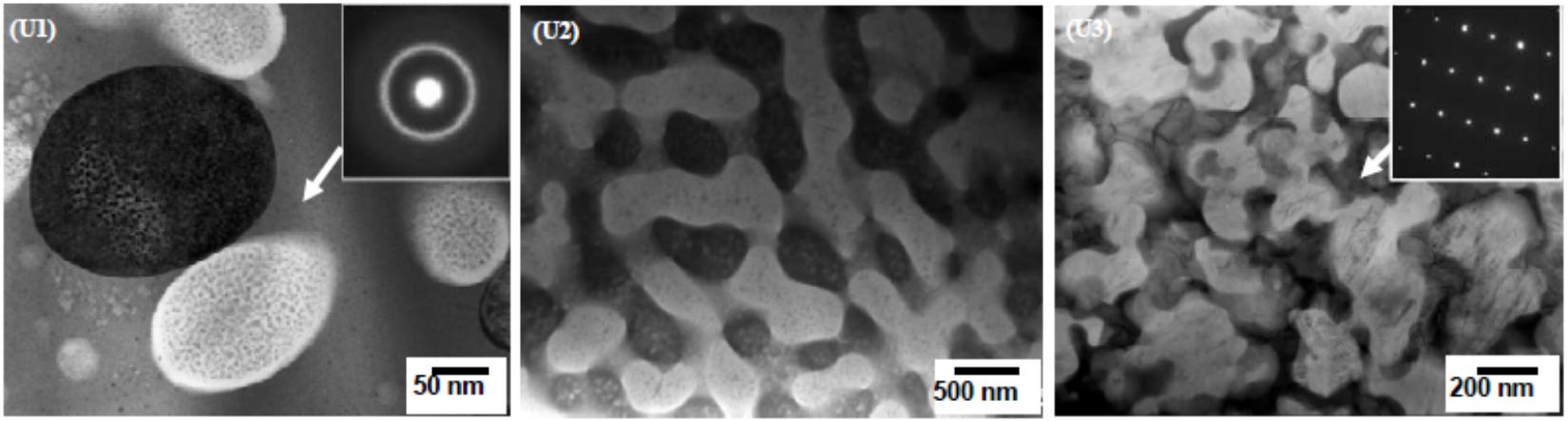

Chang et al., Acta Mater (2010)

Critical temperature

Spinodal critical point
$Gd_{25}Ti_{30}Al_{25}Co_{20}$ (at **1950 K**)

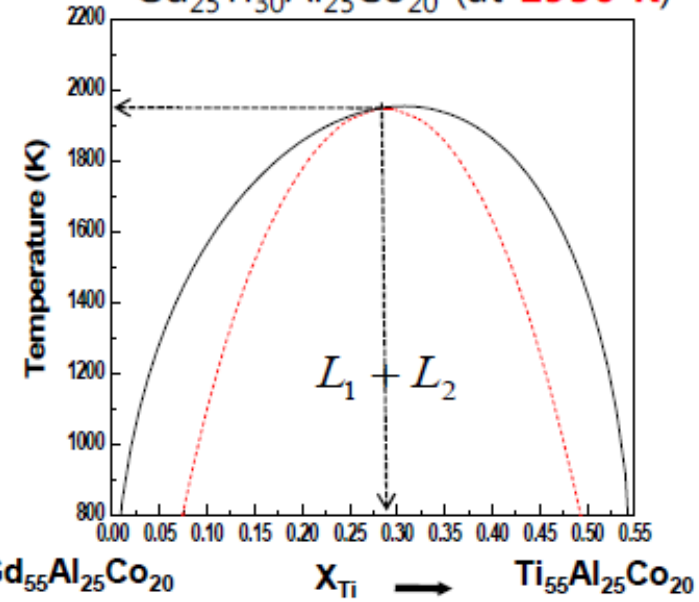

Spinodal critical point
$Gd_{18}Ti_{37}Al_{25}Cu_{20}$ (at **1300 K**)

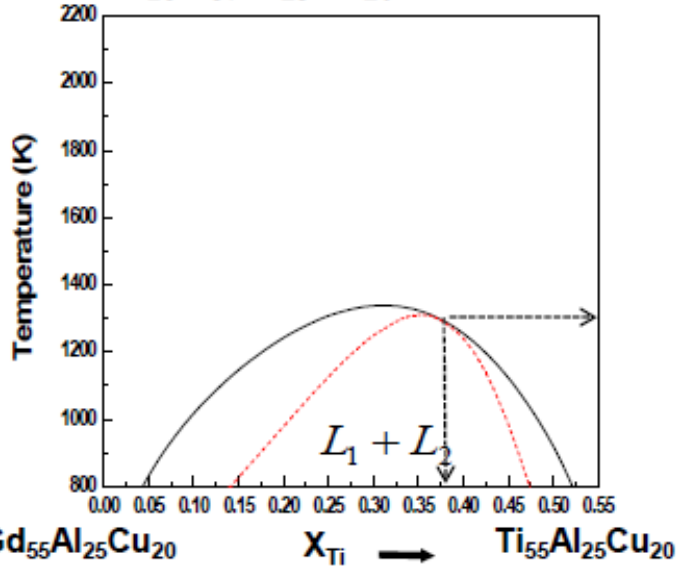

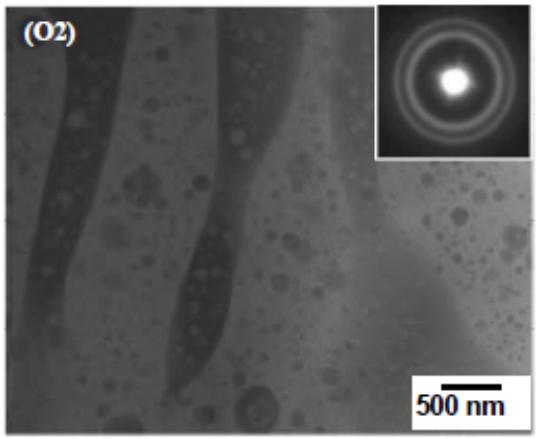

Scale of interconnected structure

←Several um

200~300 nm→

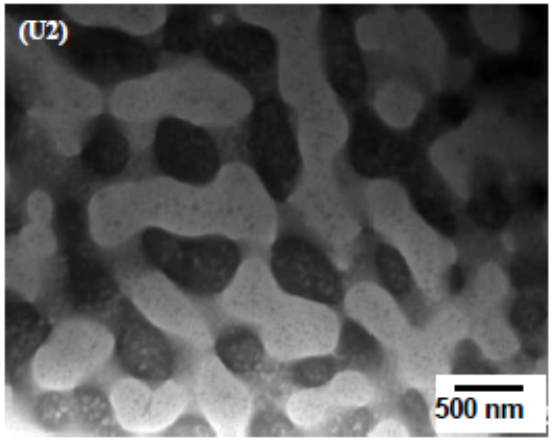

Asymmetry of spinodal curve / Decomposition range

❖ Symmetric spinodal curve / smaller decomposition range

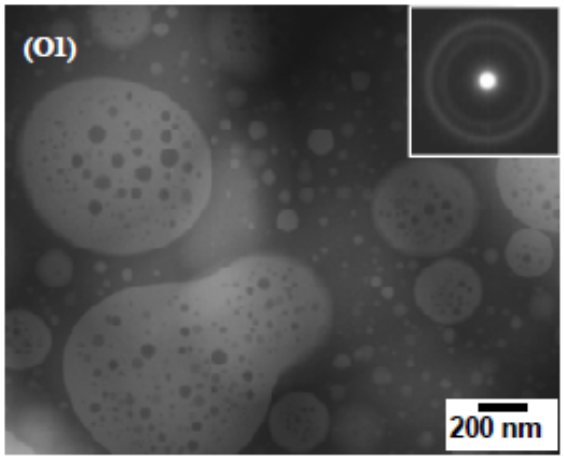

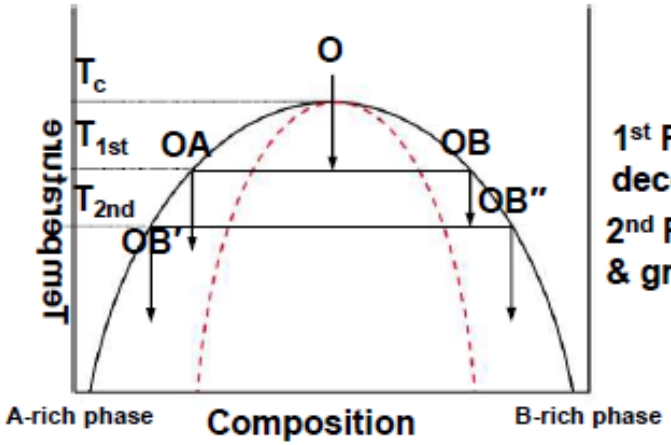

1st P.S.; spinodal decomposition

2nd P.S.; nucleation & growth

❖Asymmetric spinodal curve / larger decomposition range

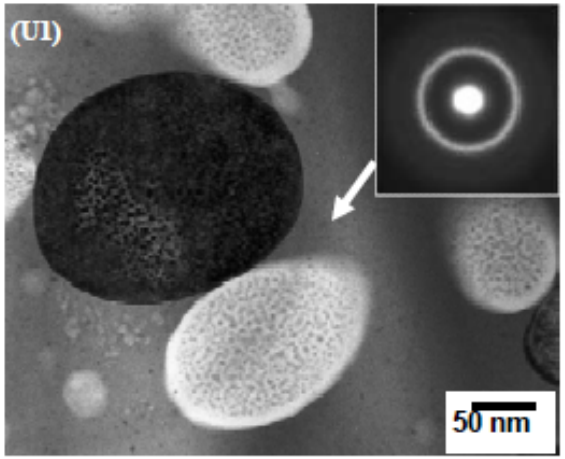

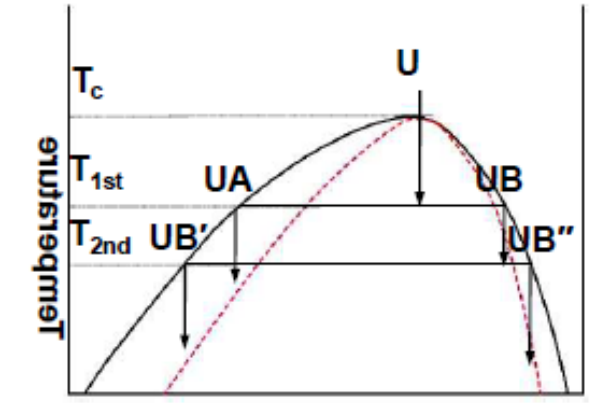

1st P.S.; spinodal decomposition

2nd P.S.; spinodal decomposition

(b) Significantly different heat of mixing relation among constituent elements

According to Meijering , a ternary alloy phase can decompose into two phases with different composition seven when the enthalpy of mixing is negative.

- Cu-Zr-Be ternary alloy system

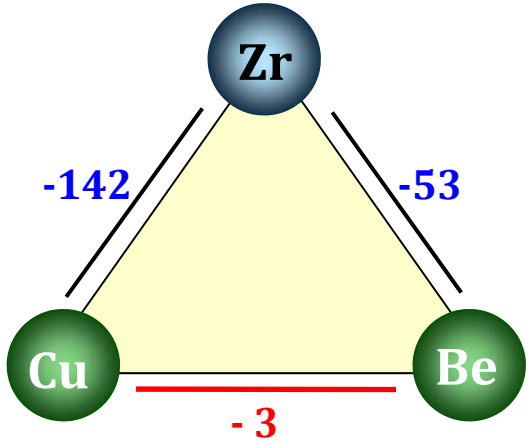

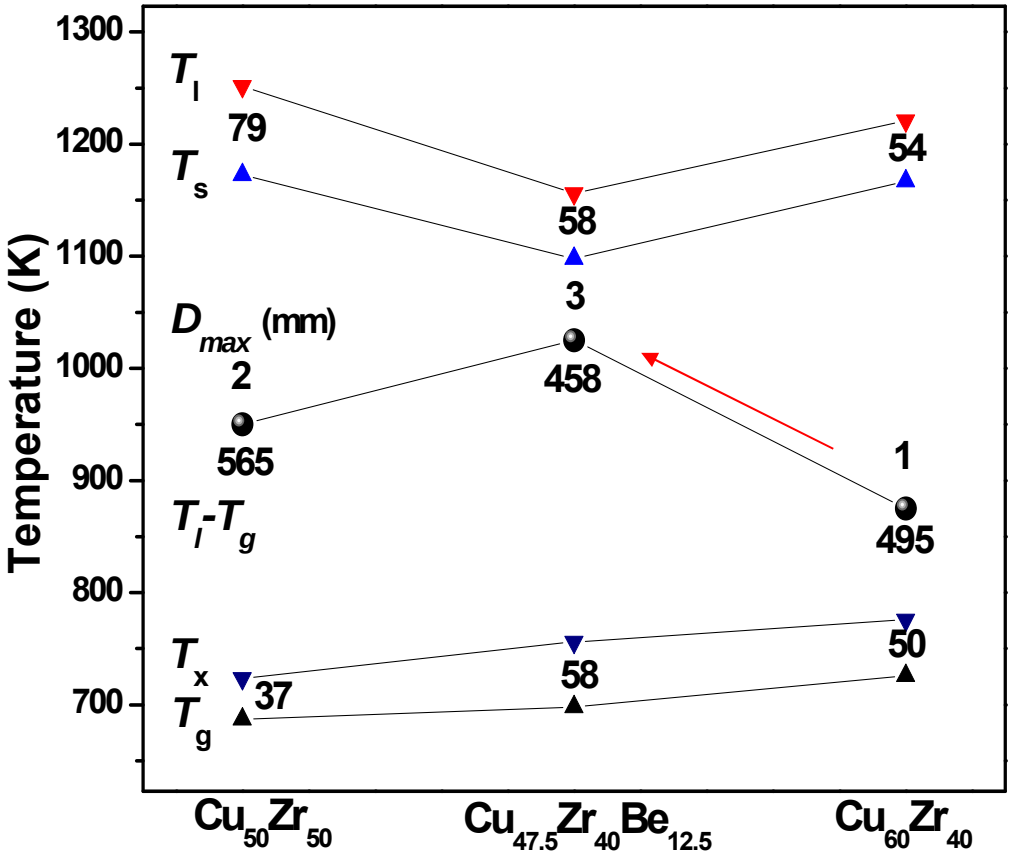

* ESPark, Acta Materialia (2008)

Cu-Zr-Be ternary alloy system: Cu-Zr & Zr-Be rich phases

- Compression test

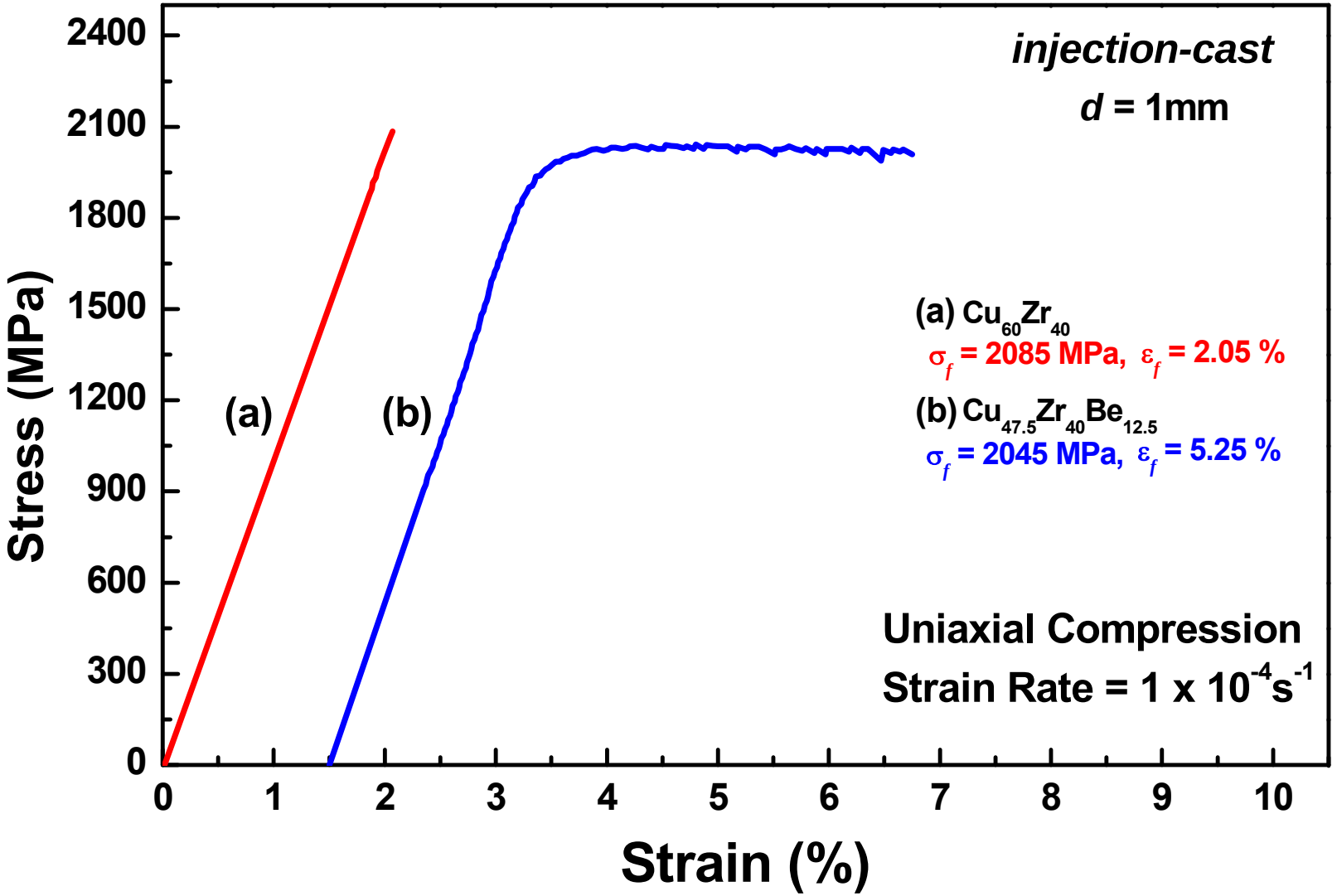

EXAFS analysis

	r (Å)		*N*		Total *N*	σ²	
	Cu-Cu	Cu-Zr	Cu-Cu	Cu-Zr		Cu-Cu	Cu-Zr
$Cu_{60}Zr_{40}$	2.49	2.69	3.0	3.7	6.7	0.0116	0.0233
$Cu_{47.5}Zr_{40}Be_{12.5}$	2.51	2.70	2.5	4.8	7.3	0.0107	0.0227
	Zr-Zr	Zr-Cu	Zr-Zr	Zr-Cu		Zr-Zr	Zr-Cu
$Cu_{60}Zr_{40}$	3.10	2.68	6.9	4.4	11.3	0.0263	0.0124
$Cu_{47.5}Zr_{40}Be_{12.5}$	3.12	2.69	6.2	3.5	9.7	0.0257	0.0130

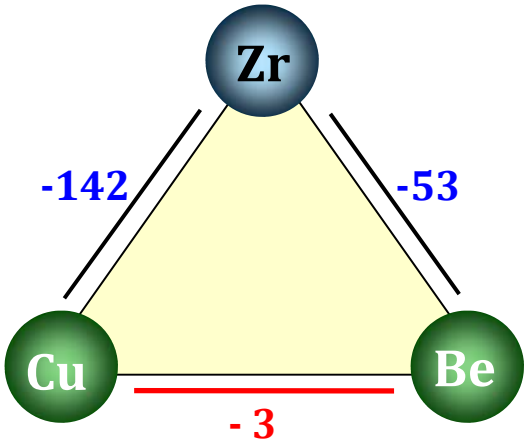

Atoimic diameter in Å: Cu-Cu = 2.56, Cu-Zr = 2.88, Zr-Zr = 3.20.

Cargill-Spaepen short-range order parameters, η

	Z_{AB}	<Z>	Z^*_{AB}	Z^{**}_{AB}	η
$Cu_{60}Zr_{40}$	3.7	8.540	3.416	3.546	0.043
$Cu_{47.5}Zr_{40}Be_{12.5}$	4.8	7.348	2.939	3.855	0.245

Cargill-Spaepen SRO parameter

$$\eta = Z_{AB} / Z^{**}_{AB} - 1$$

$$Z^{**}_{AB} = x_B Z_B Z_A / < Z >$$

η > 0

chemical ordering between AB nearest-neighbor pairs

Unique Composite Materials Using Miscibility Gap

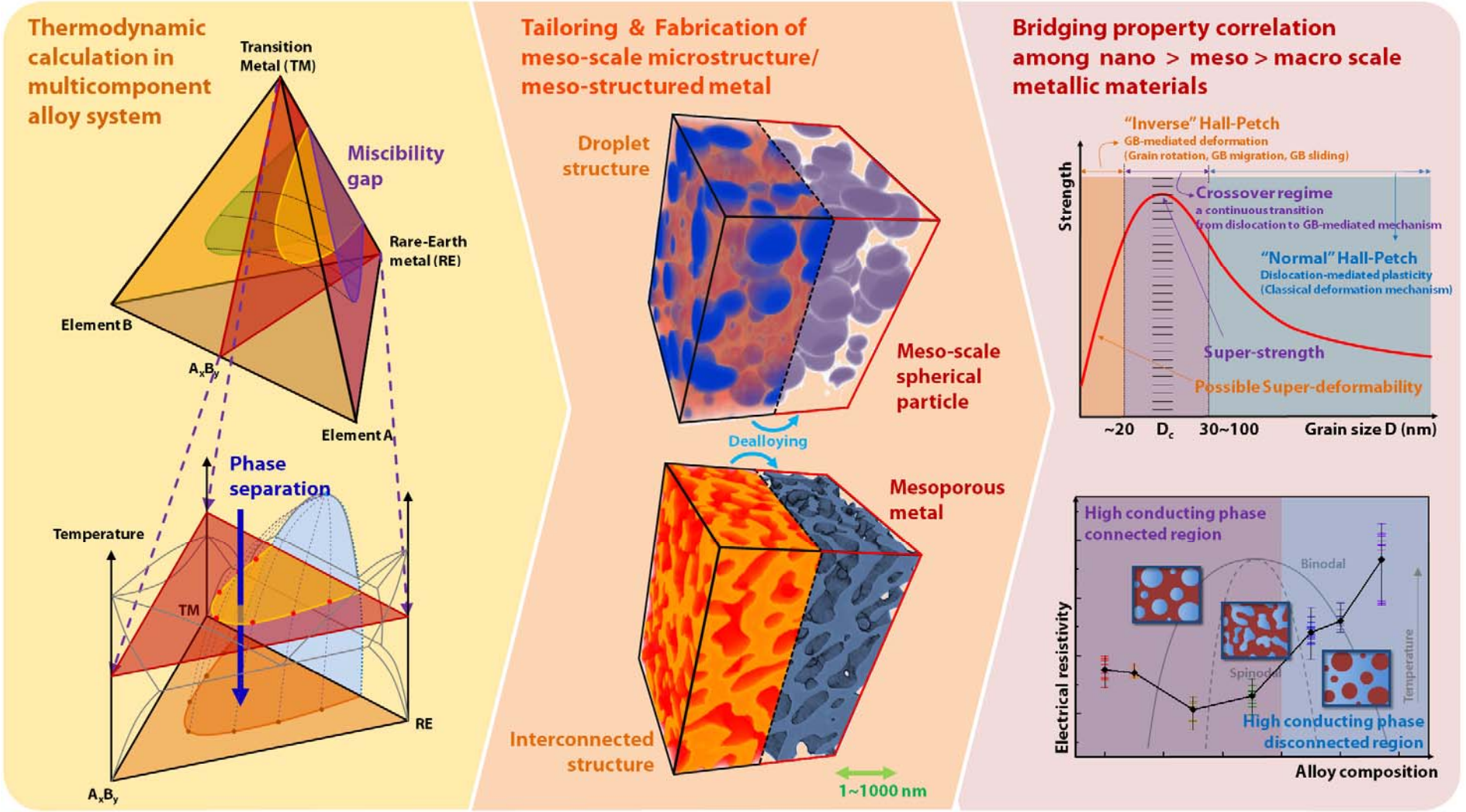

Phase separation by adding elements having PEM

* Substitution of Nd with Zr in Nd-Co-Al system

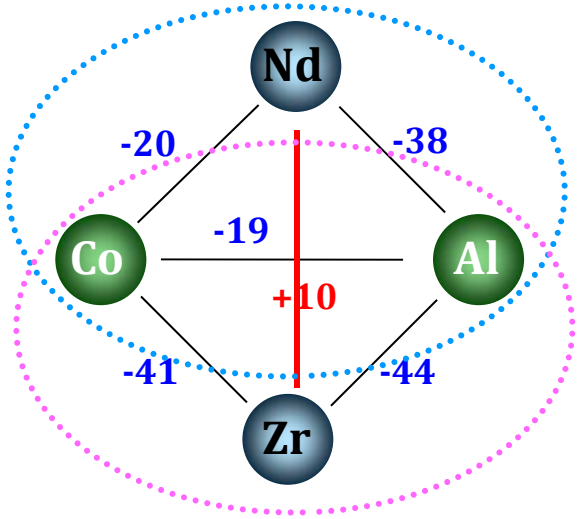

$Nd_{60}Al_{10}Co_{30}$ - 5mm

$Zr_{55}Al_{20}Co_{25}$ - 3mm

Possibility of two phase !!!

Nd-Co-Al, Zr-Co-Al

• Sripta Mater. 56, 197 (2007)

TEM results for $Nd_{30}Zr_{30}Al_{10}Co_{30}$ alloy

$Nd_{60}Al_{10}Co_{30}$
2.91 Å

$Nd_{30}Zr_{30}Al_{10}Co_{30}$
2.37 Å, 2.99 Å

$Zr_{60}Al_{10}Co_{30}$
2.40 Å

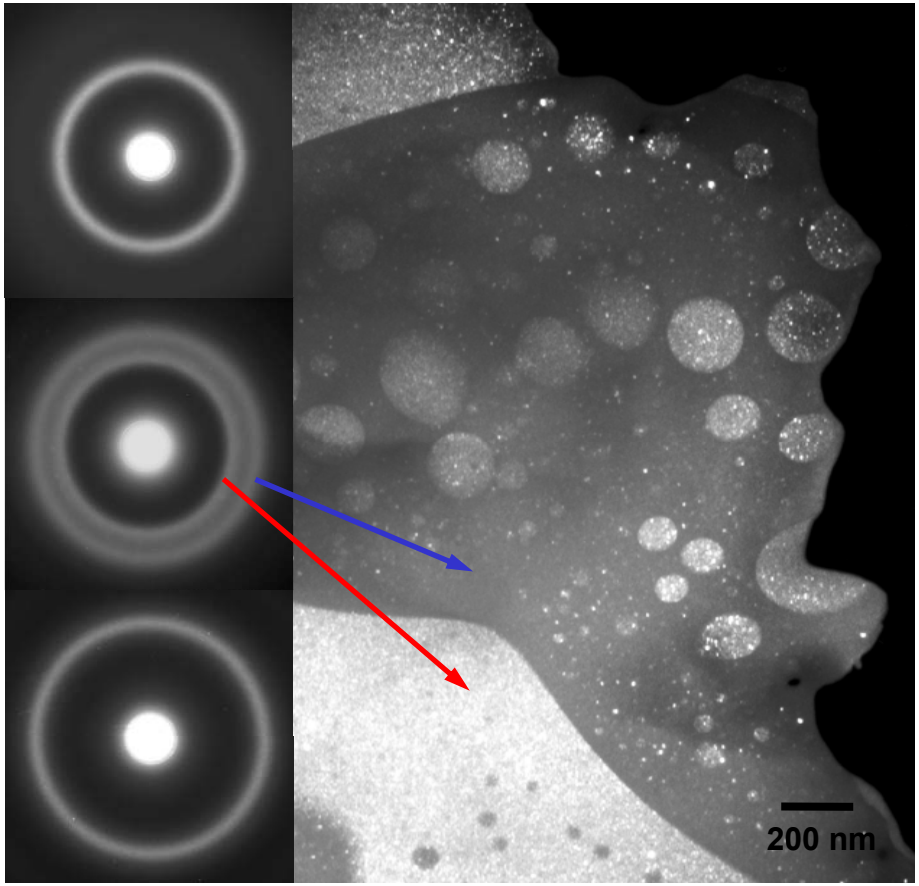

SADP and Dark-field TEM image

Measurement of viscosity using TMA

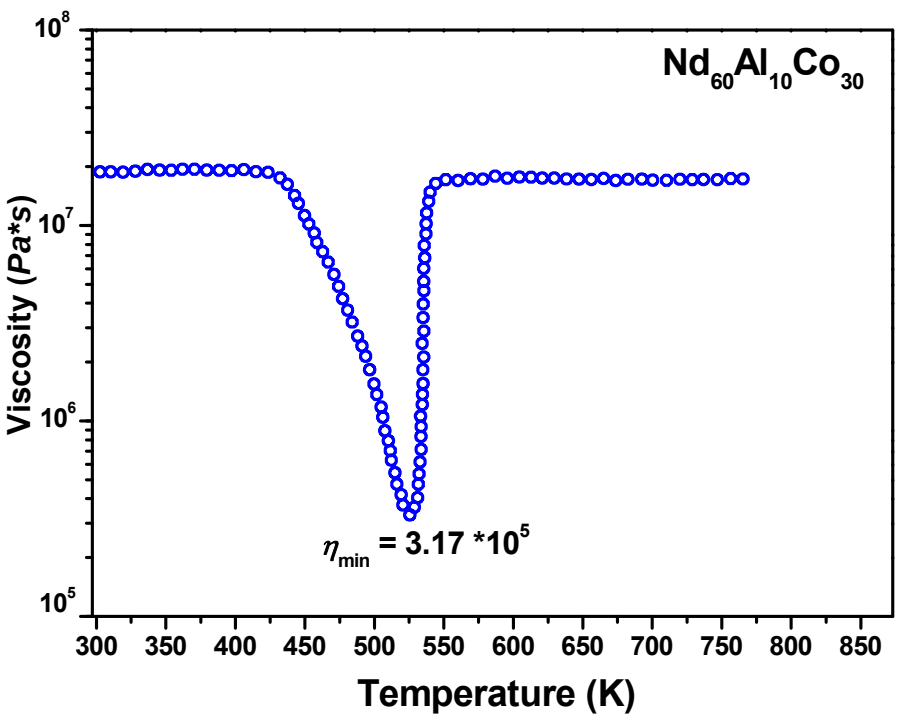

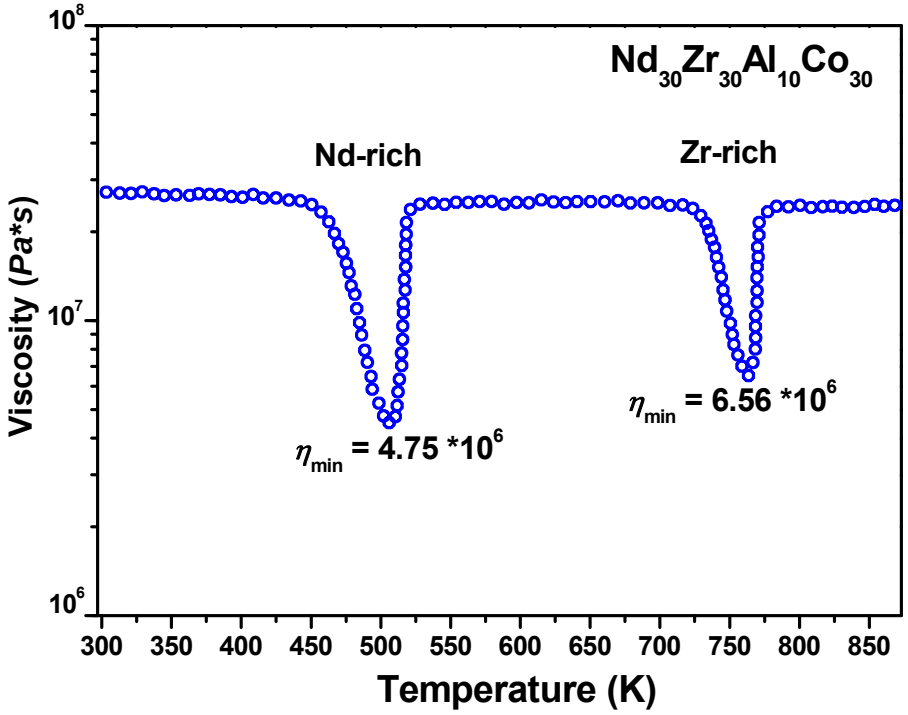

Selective partial devitrification (first SLR), followed by easy deformation of the amorphous/ crystalline composite structure (second SLR) is possible for this alloy system.

Measurement of magnetic property using VSM

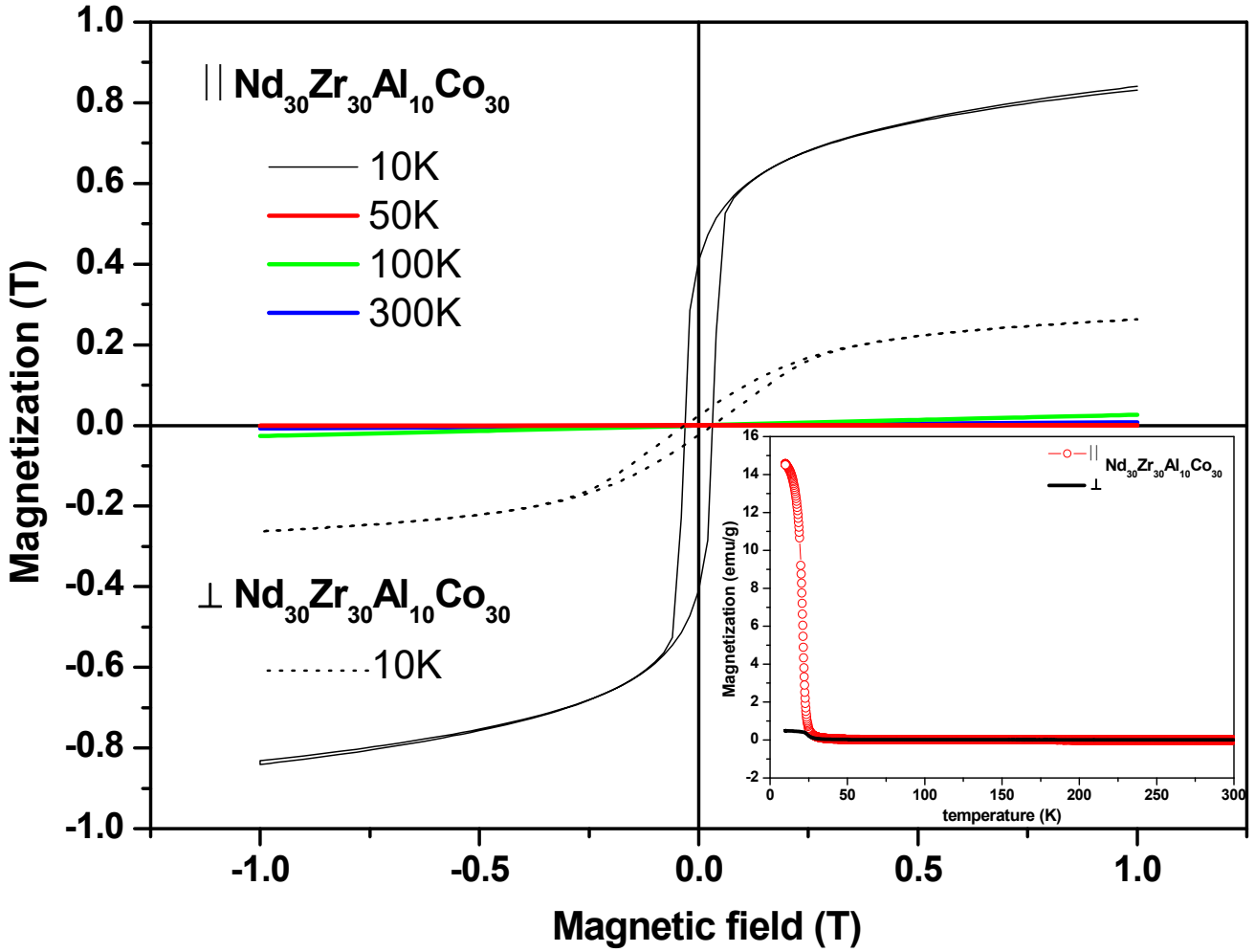

Directional changes of magnetic property in two-phase metallic glass

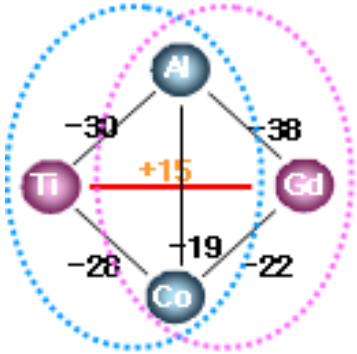

$Gd_{55}Al_{25}Co_{20}$

Ti

Zr

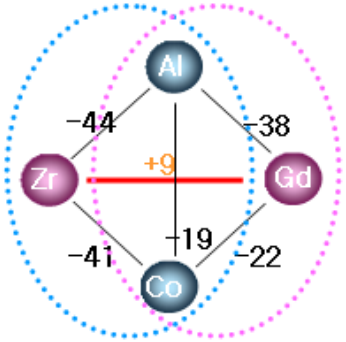

$Gd_{30}Ti_{25}Al_{25}Co_{20}$

$Gd_{30}Zr_{25}Al_{25}Co_{20}$

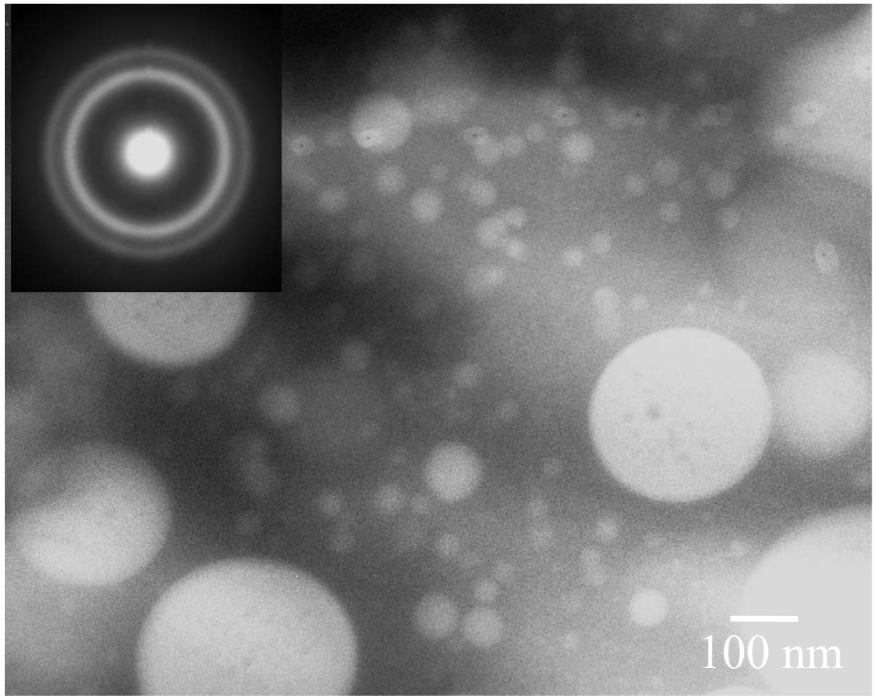

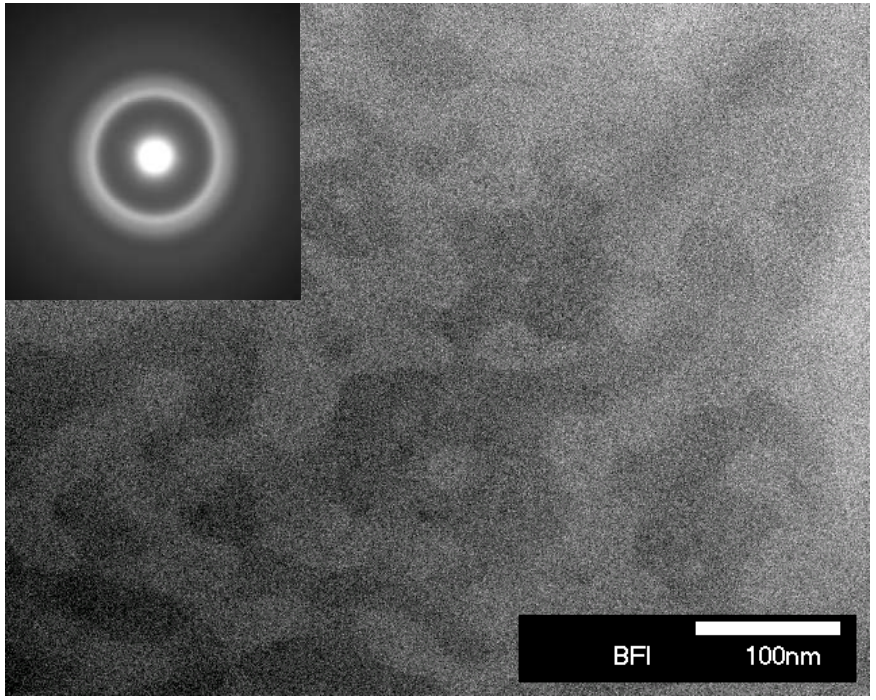

Droplet structure ⟷ Interconnected structure

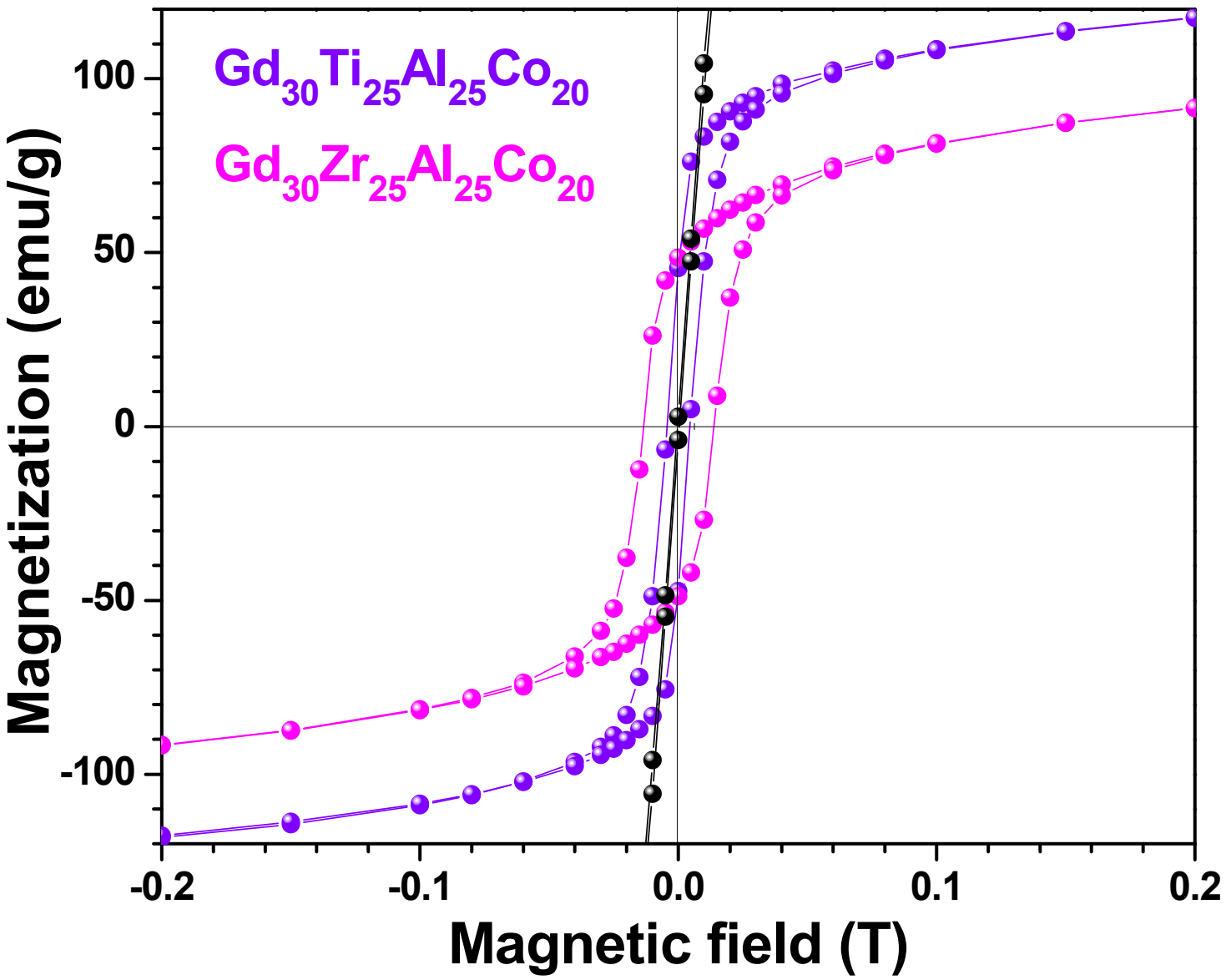
Gd30Ti25Al25Co20
Gd30Zr25Al25Co20
Magnetization (emu/g)
Magnetic field (T)
100
50
0
-50
-100
-0.2
-0.1
0.0
0.1
0.2

Interconnected structure

$Gd_{30}Zr_{25}Al_{25}Co_{20}$

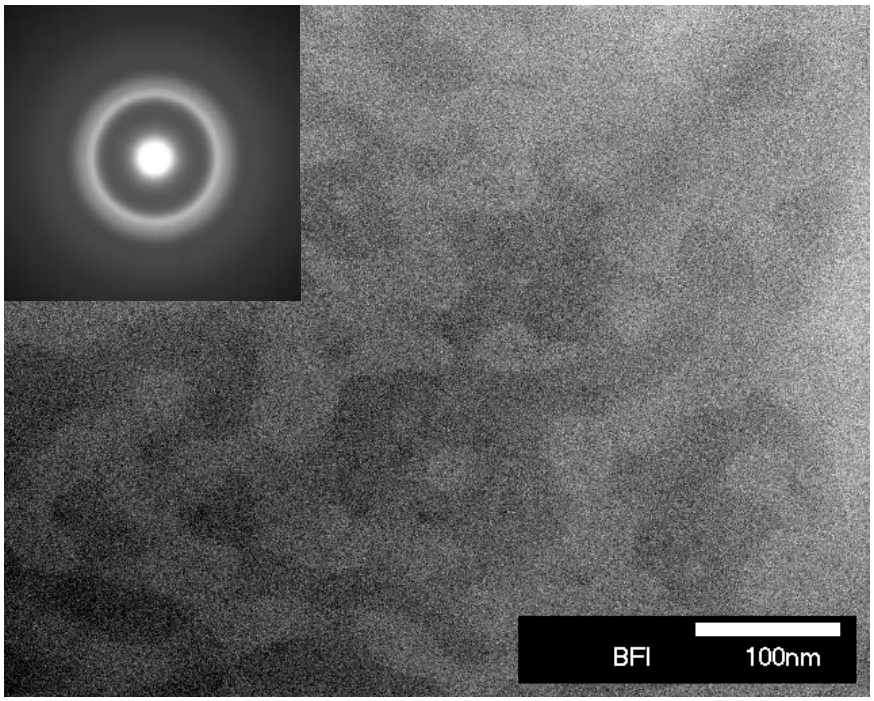

Amorphous + Amorphous

$Gd_{30}Zr_{25}Al_{25}Cu_{20}$

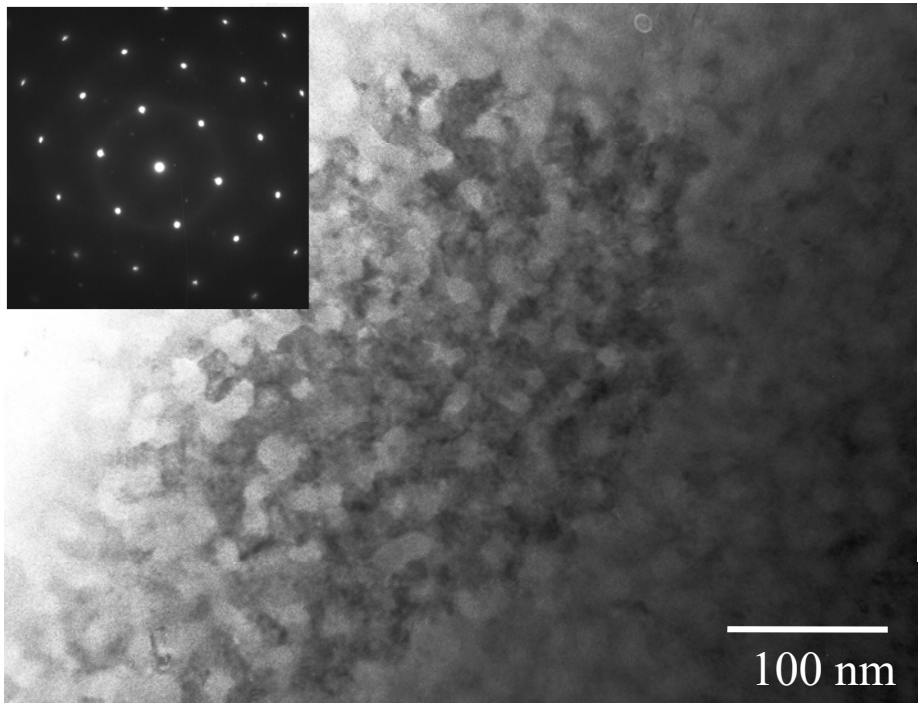

Amorphous + Crystals

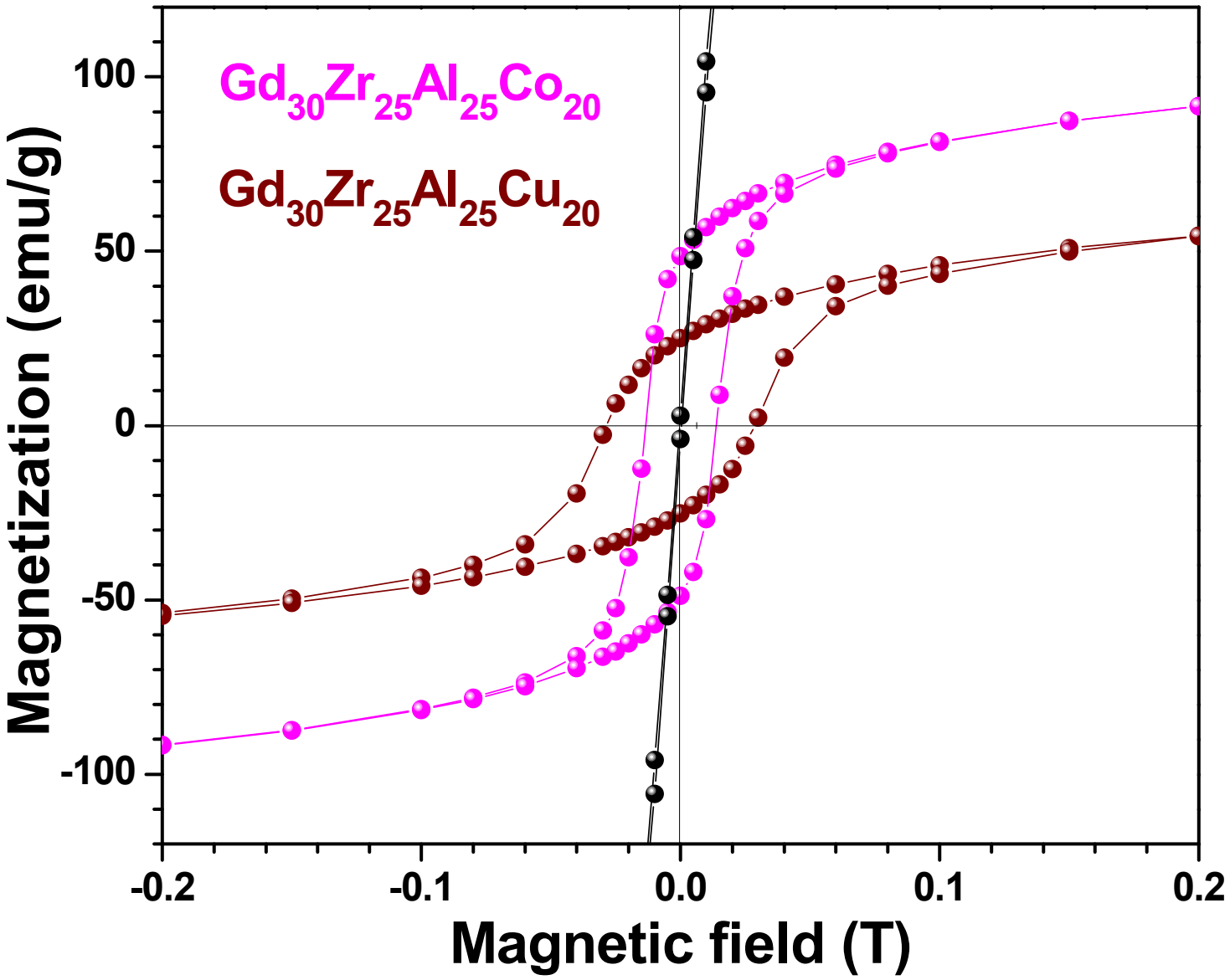
Gd30Zr25Al25Co20
Gd30Zr25Al25Cu20
Magnetization (emu/g)
Magnetic field (T)
100
50
0
-50
-100
-0.2
-0.1
0.0
0.1
0.2

$Gd_{30}Zr_{25}Al_{25}Co_{20}$

* unpublished (2007)

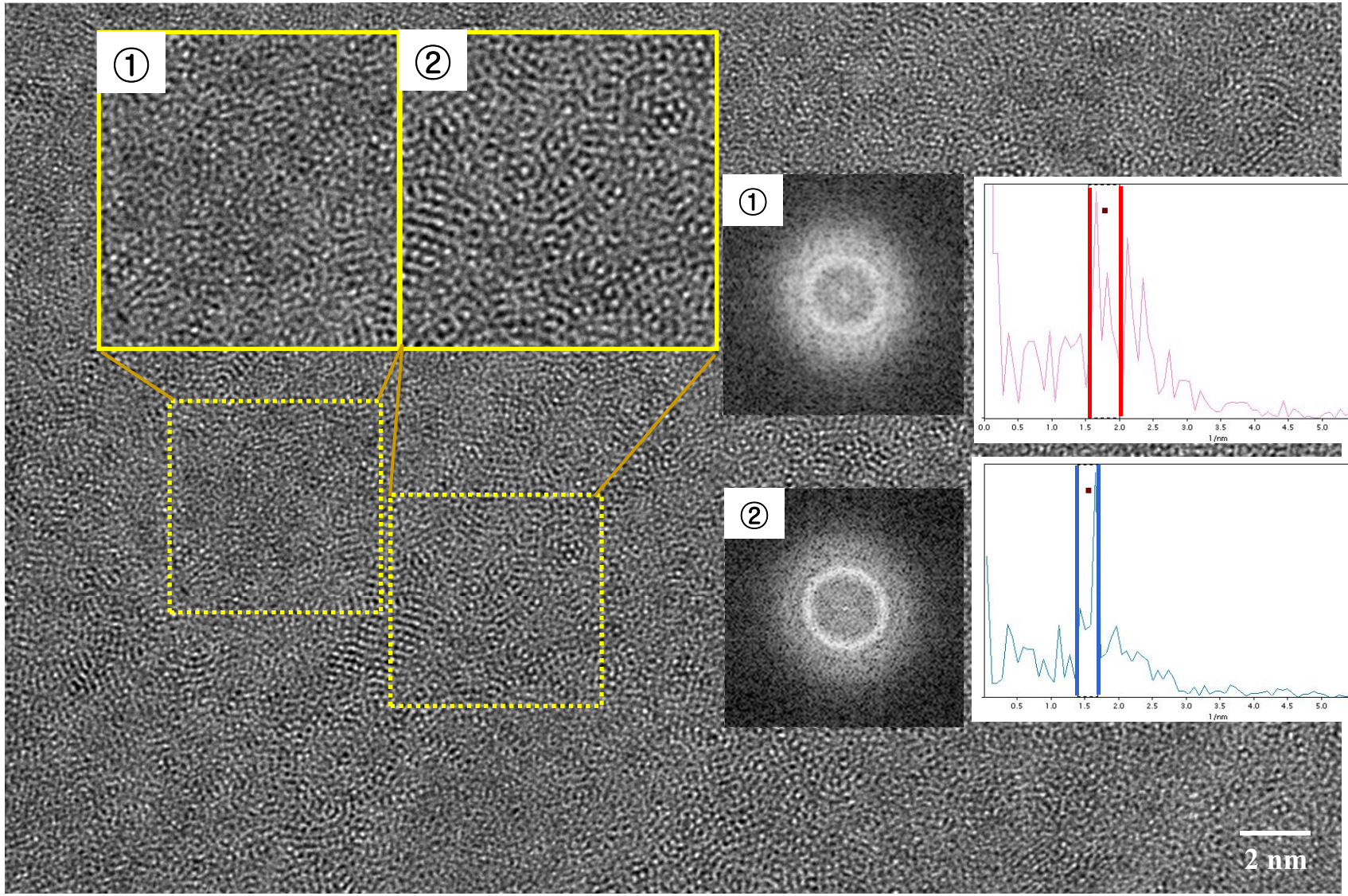

Effect of element with positive enthalpy of mixing among constituent elements

atomic scale heterogeneity

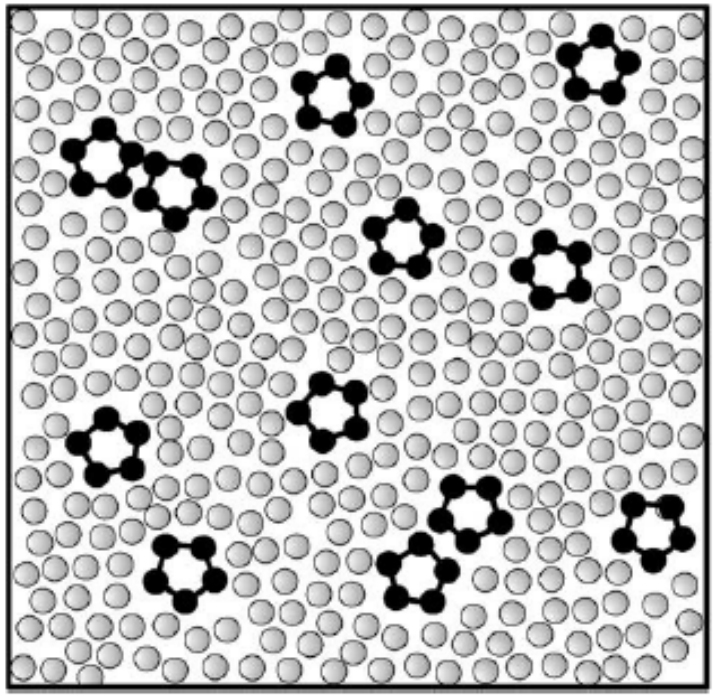

Enhancement of plasticity in BMGs

Phase separating metallic glasses

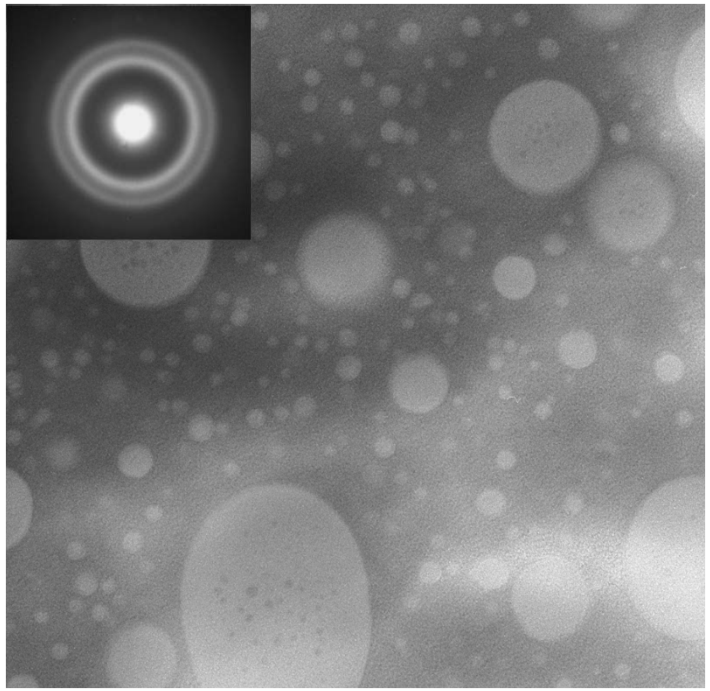

Unique properties

Dealloying (selective dissolution) process

- **Process of selective dissolution of the most electrochemically active component**

J. Jayaraj et al., Scripta Mat., 55 (2006) 1063.

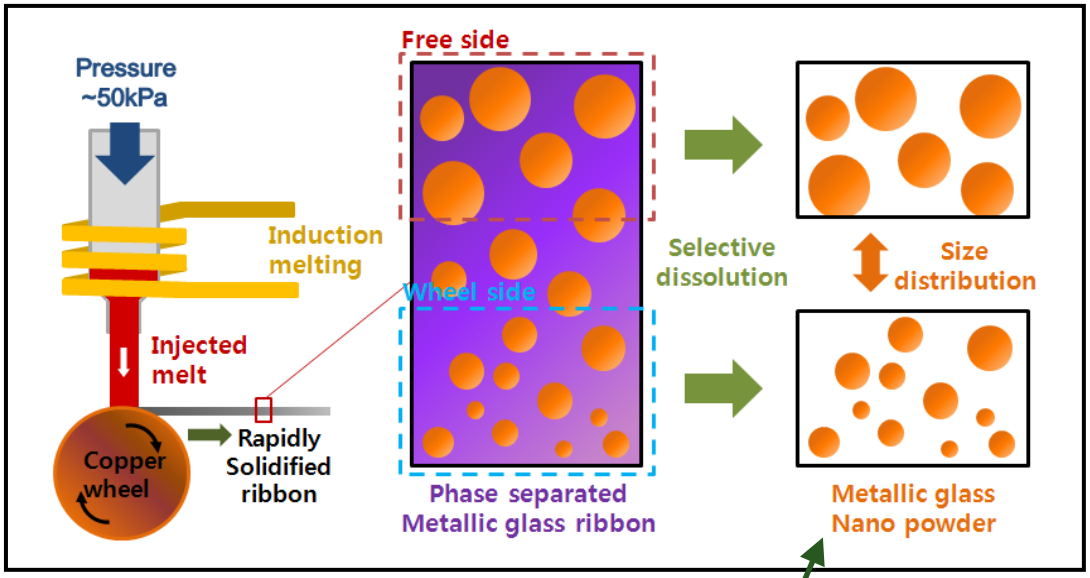

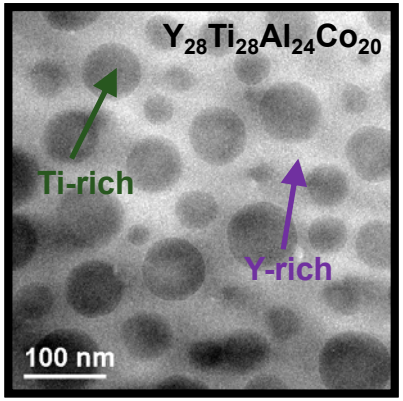

Dealloying process

J. Jayaraj et al., Scripta Mat., 55 (2006) 1063.

Y : intensively reactive to HNO_3 soln.
Ti : strong resistance to corrosion by HNO_3 soln.

Immersion of the alloy in etchant solution.

➡ Selective dissolution of Y-rich phase

➡ Formation of Ti-rich spherical nanoparticles

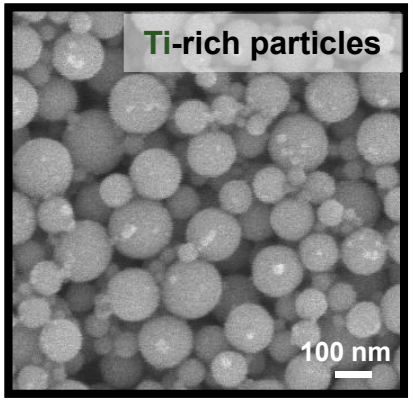

Compositional effects on phase separated microstructures

▼ Y-Ti-Al-Co system

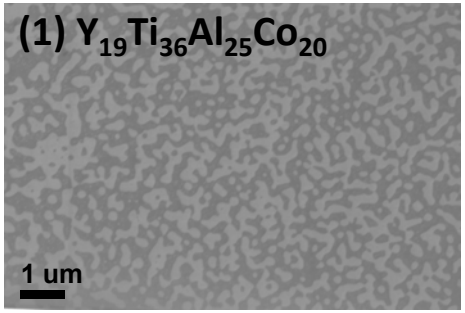

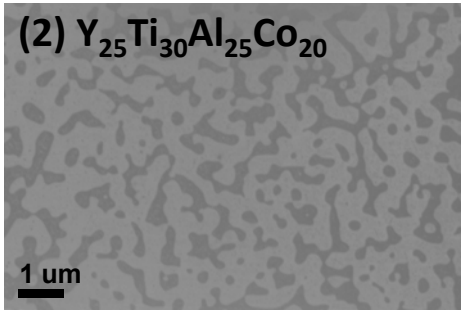

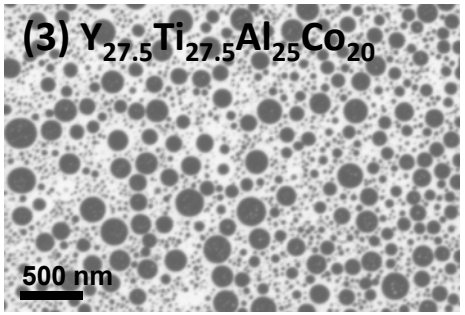

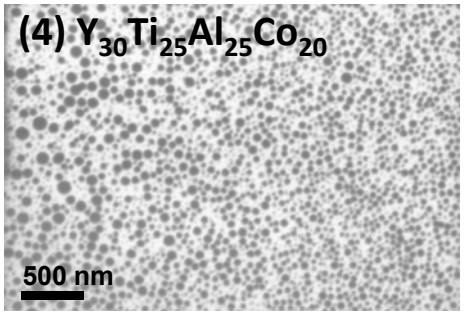

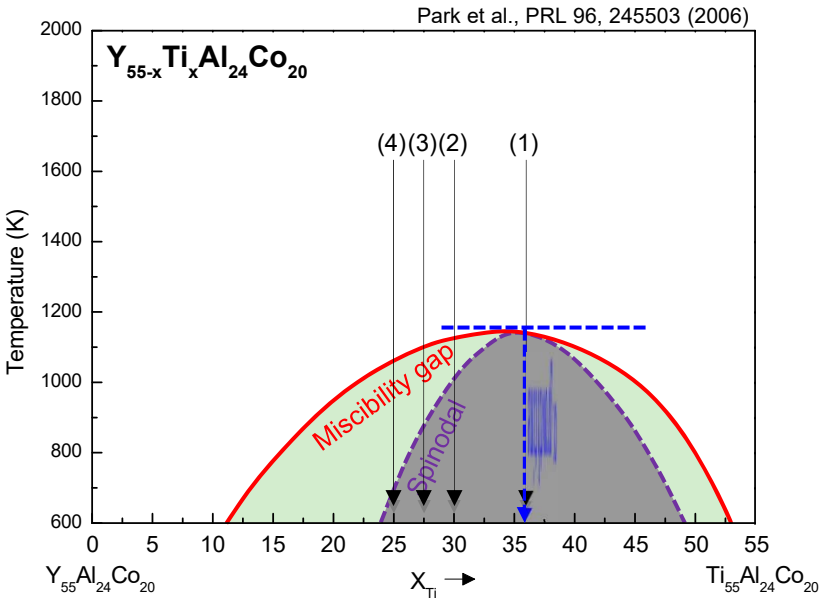

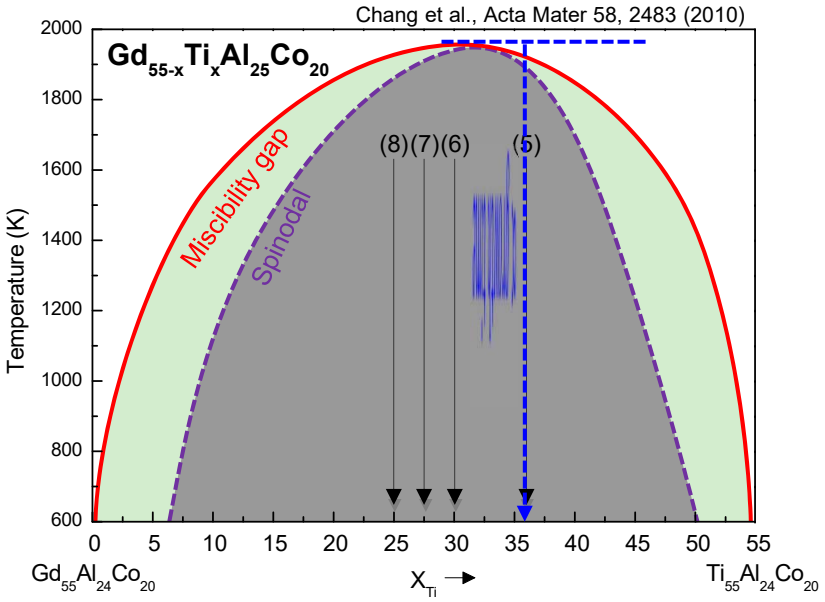

▼ Gd-Ti-Al-Co system

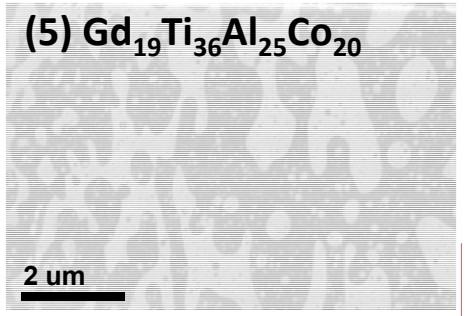

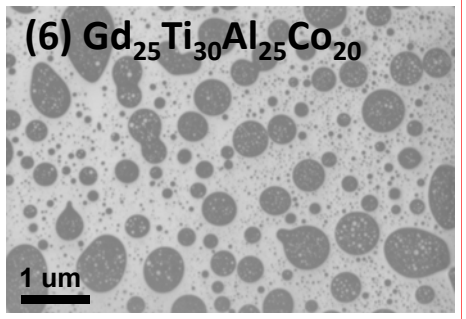

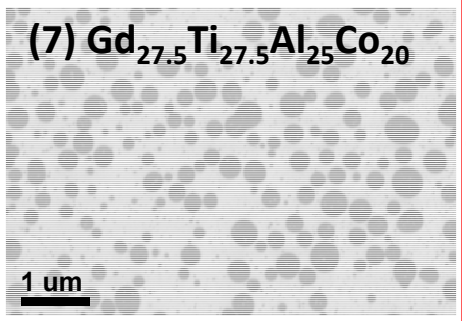

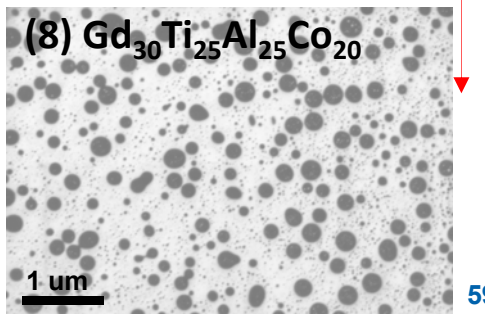

Increase of (Y,Gd) composition

Cooling rate effect on phase separated microstructures

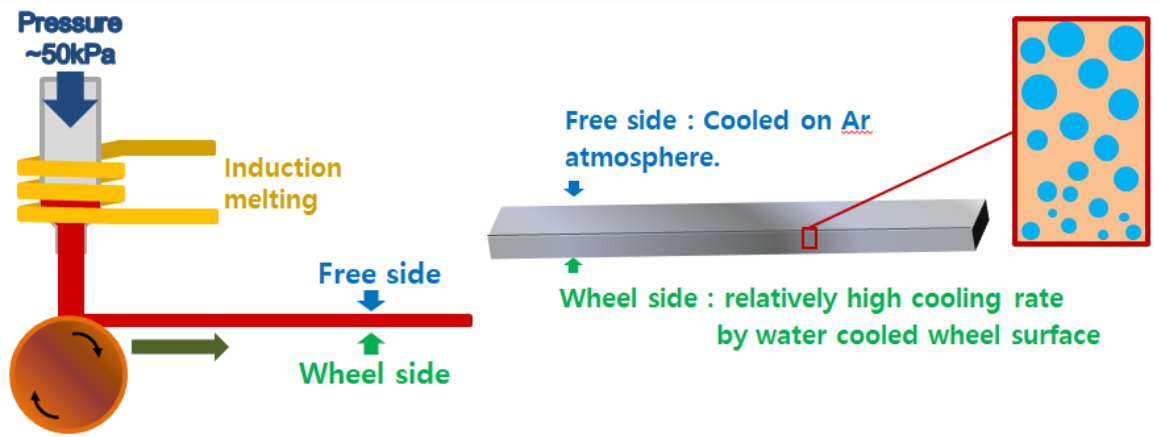

- SEM images of $Y_{27.5}Ti_{27.5}Al_{25}Co_{20}$ ribbon sample

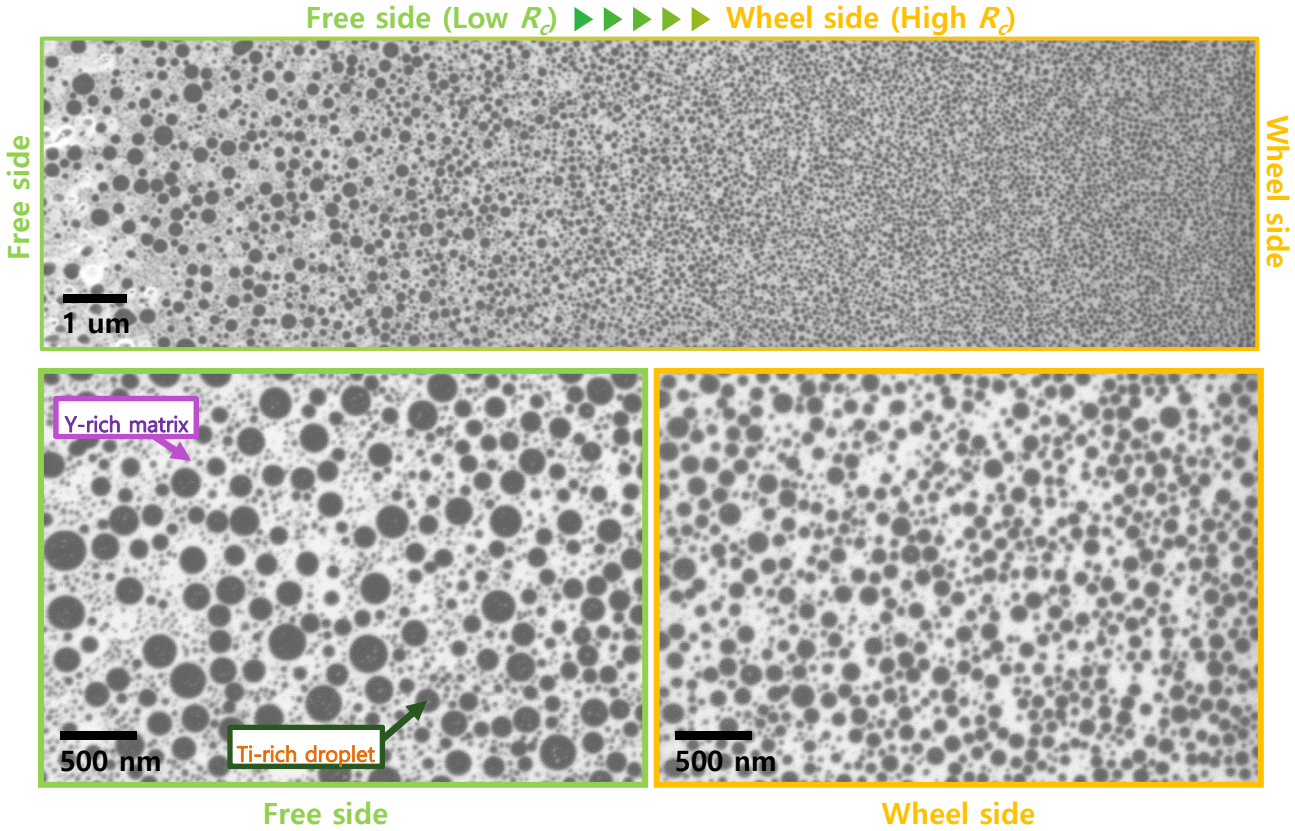

Nanoparticle preparation : Dealloying of phase separating metallic glass

Dealloying process

J. Jayaraj et al., Scripta Mat., 55 (2006) 1063.

Y, Gd : intensively reactive to HNO_3 soln.
Ti : strong resistance to corrosion by HNO_3 soln.

Immersion of the alloy in etchant solution.

➡ **Selective dissolution of Y, Gd-rich phase**

➡ **Formation of Ti-rich spherical nanoparticles**

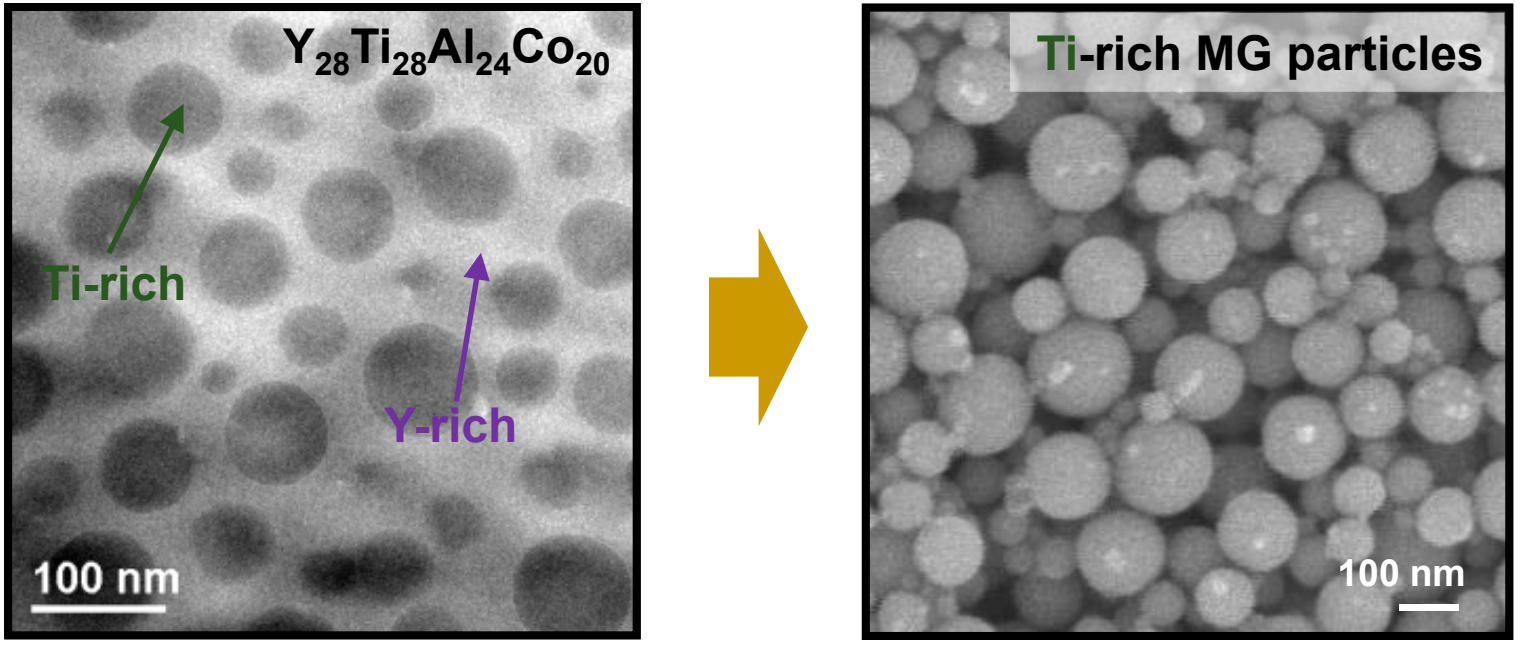

⇨ **Various diameters / same spherical geometry / without FIB process / relatively short preparation time**

Co-rich region formation after oxidation

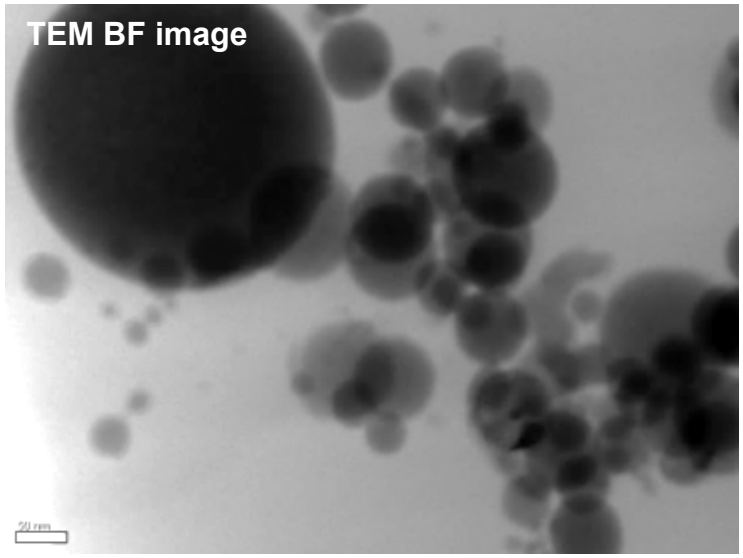

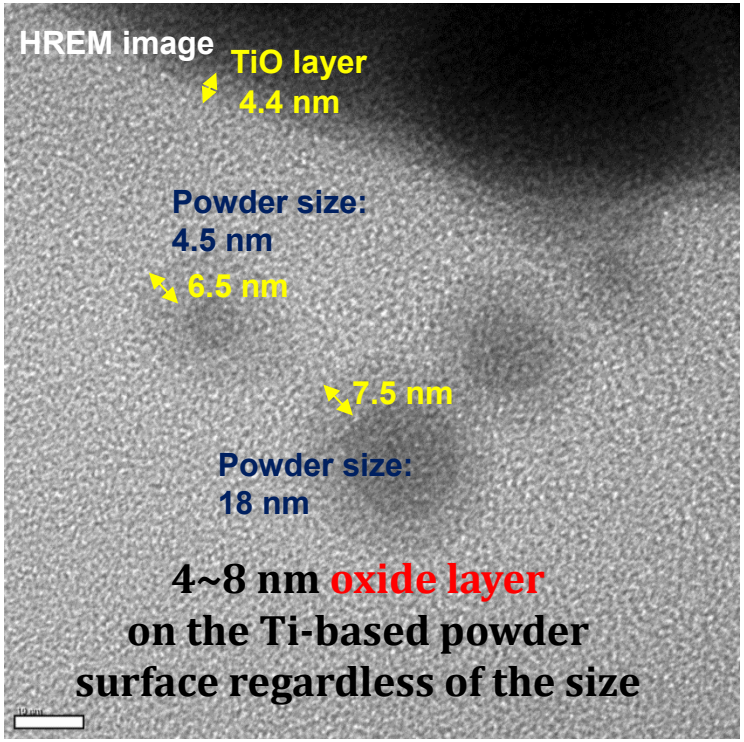

4~8 nm oxide layer on the Ti-based powder surface regardless of the size

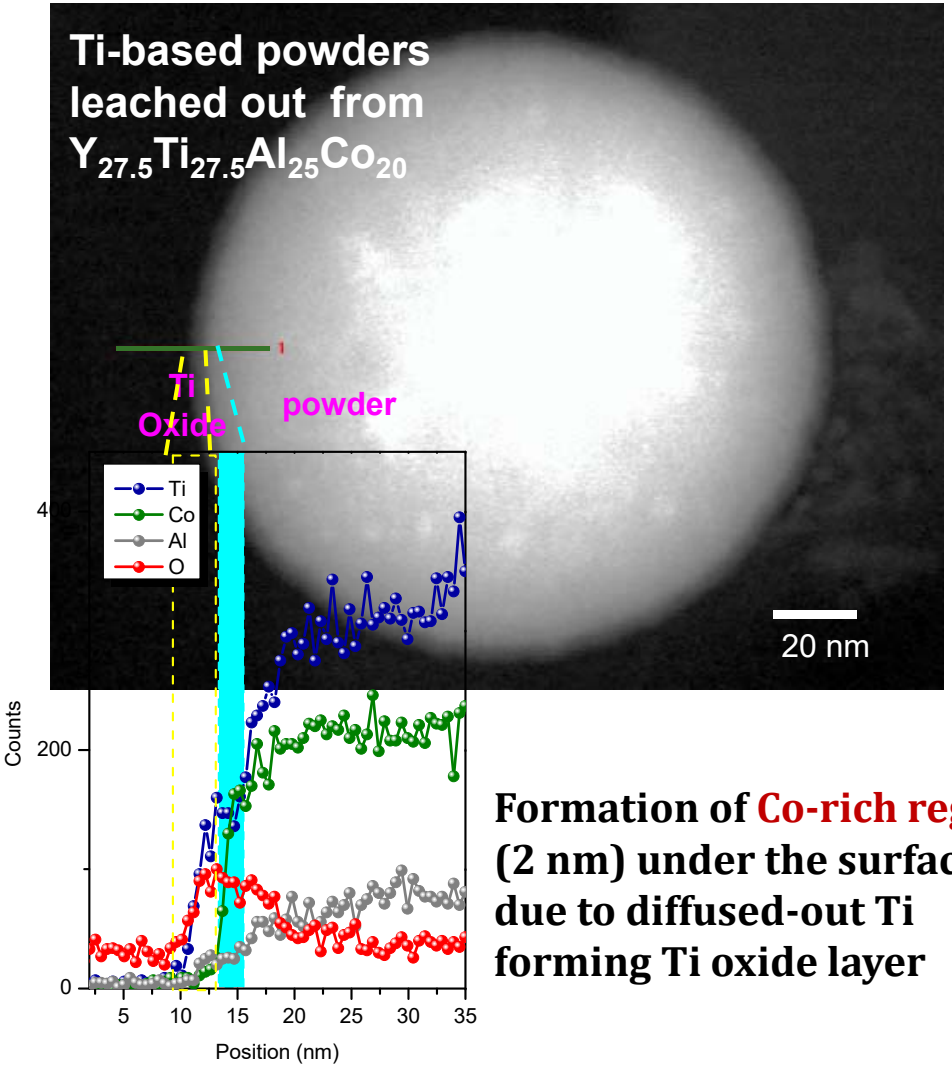

Formation of Co-rich region (2 nm) under the surface due to diffused-out Ti forming Ti oxide layer

Oxide layer	Co-rich region (Ave. comp.)	Particle (Ave. comp.)
Ti-O	$Ti_{16}Co_{22}Al_4O_{58}$	$Ti_{51}Co_{38}Al_{11}$

Surface modification of Ti-based nanopowders ➡ unique properties

▸ **SQUID results**

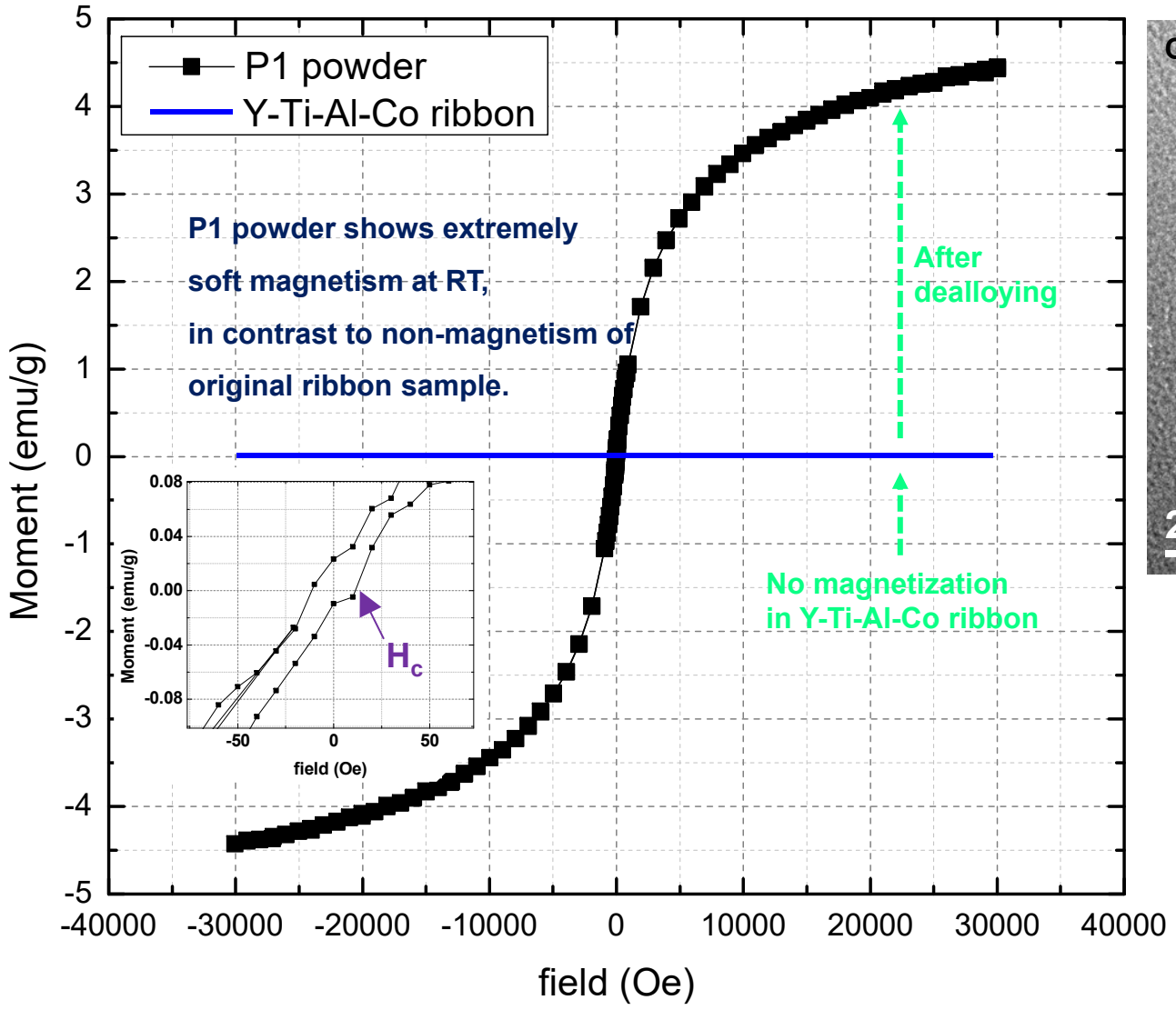

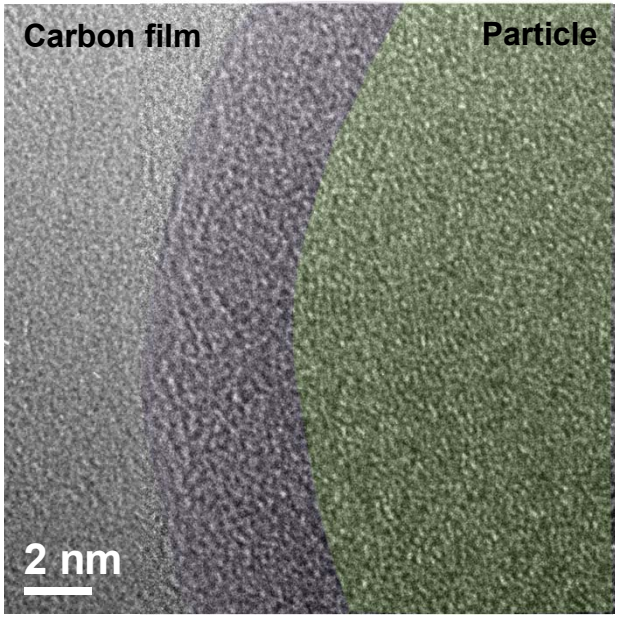

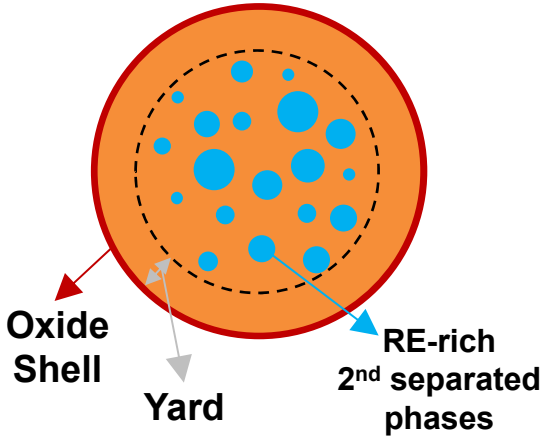

Selective dissolution of Ti-rich phase

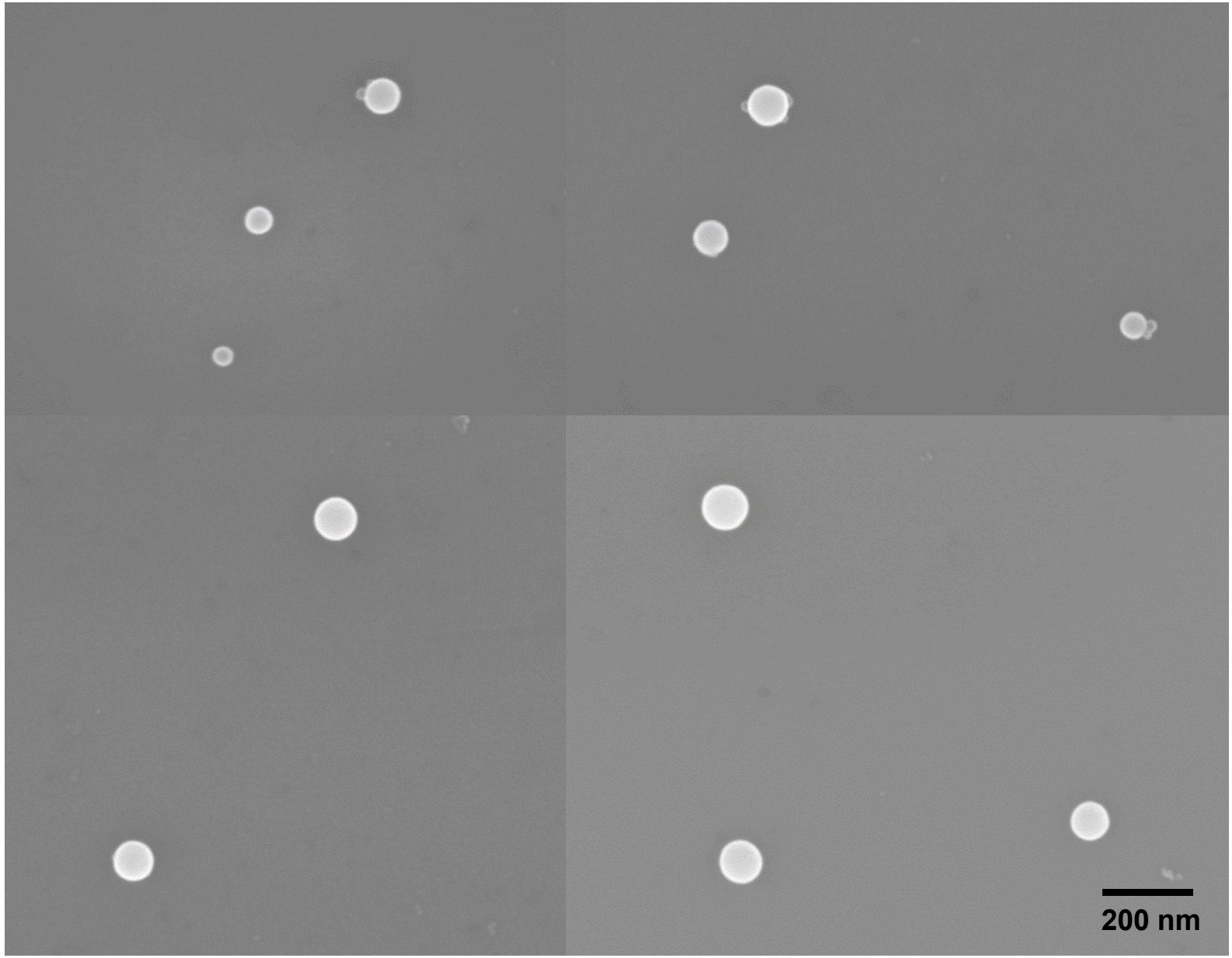

Surface morphology and microstructure of the metallic glass nanoparticle

- **Particles prepared by dealloying $Gd_{27.5}Ti_{27.5}Al_{25}Co_{20}$ ribbon sample**

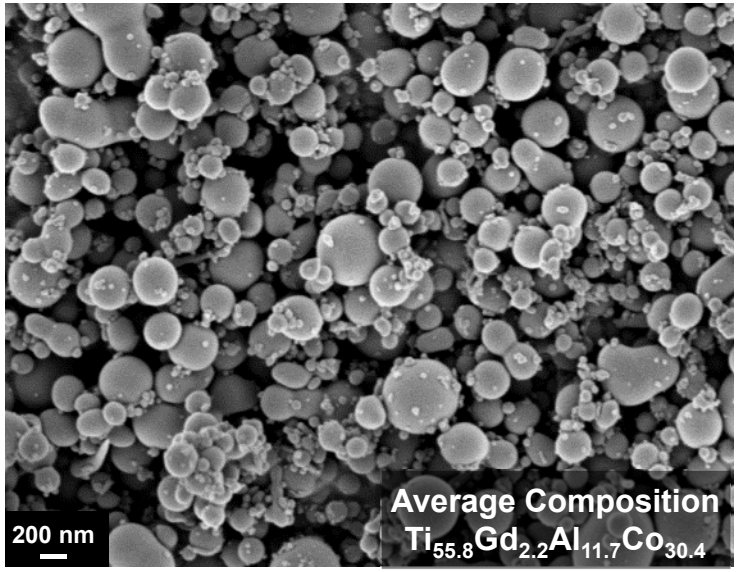

SEM image : Dealloyed Ti-Co-based MG nanoparticles

Ultrasonication

Spin-coating, Spraying

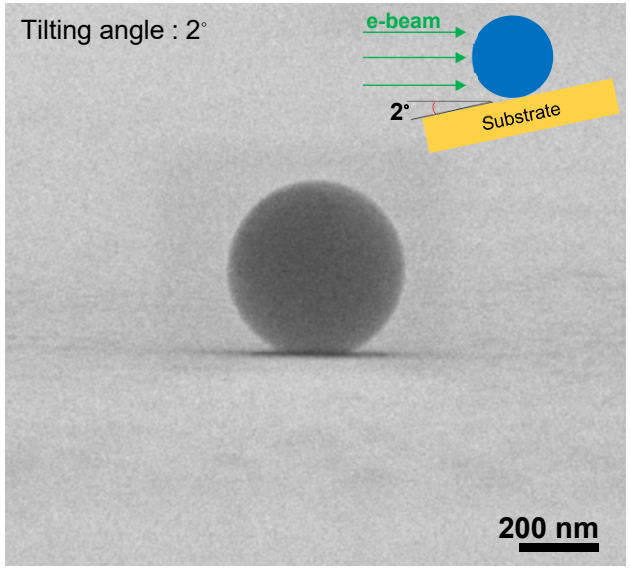

SEM image : Single nanoparticle on flat substrate

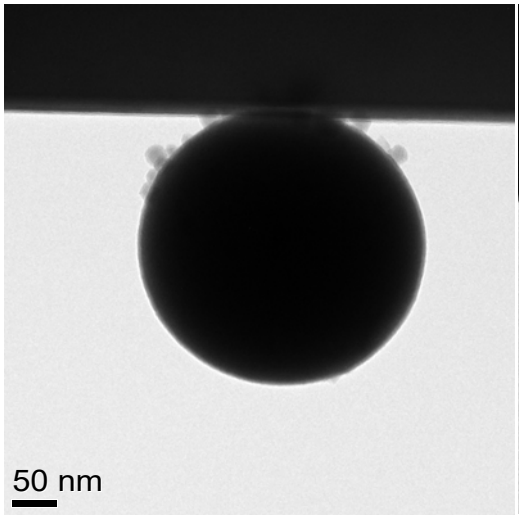

BF-TEM image : a particle (d>300nm)

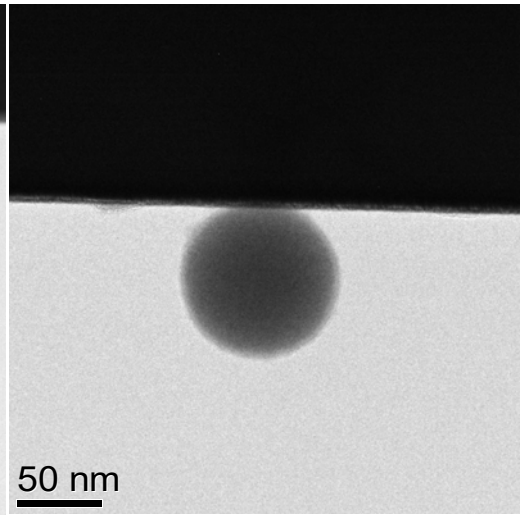

BF-TEM image : a particle (d<100nm)

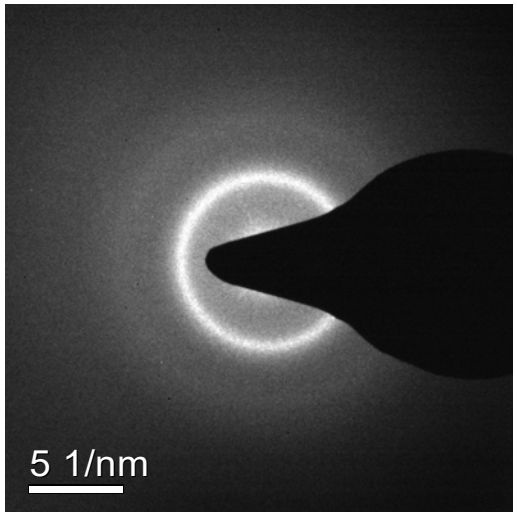

SADP of a single particle

Hysitron Picoindenter PI-85 (for SEM) & PI-95 (for TEM)

PI-85 with FEI FE-SEM

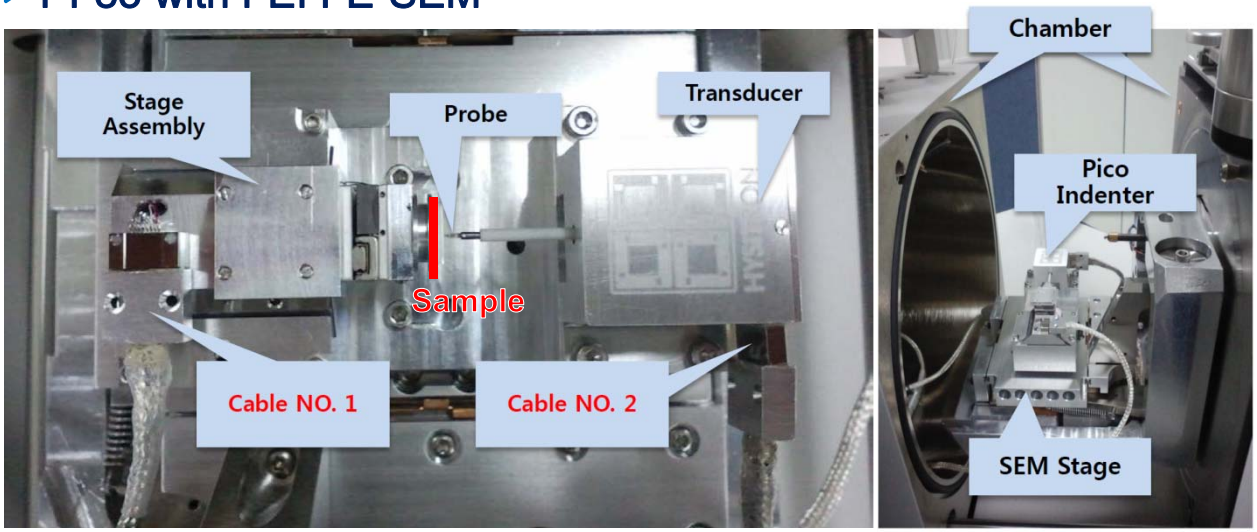

☐ Pico Indenter + SEM Chamber

PI-95 for FEI TEMs (F20, Titan)

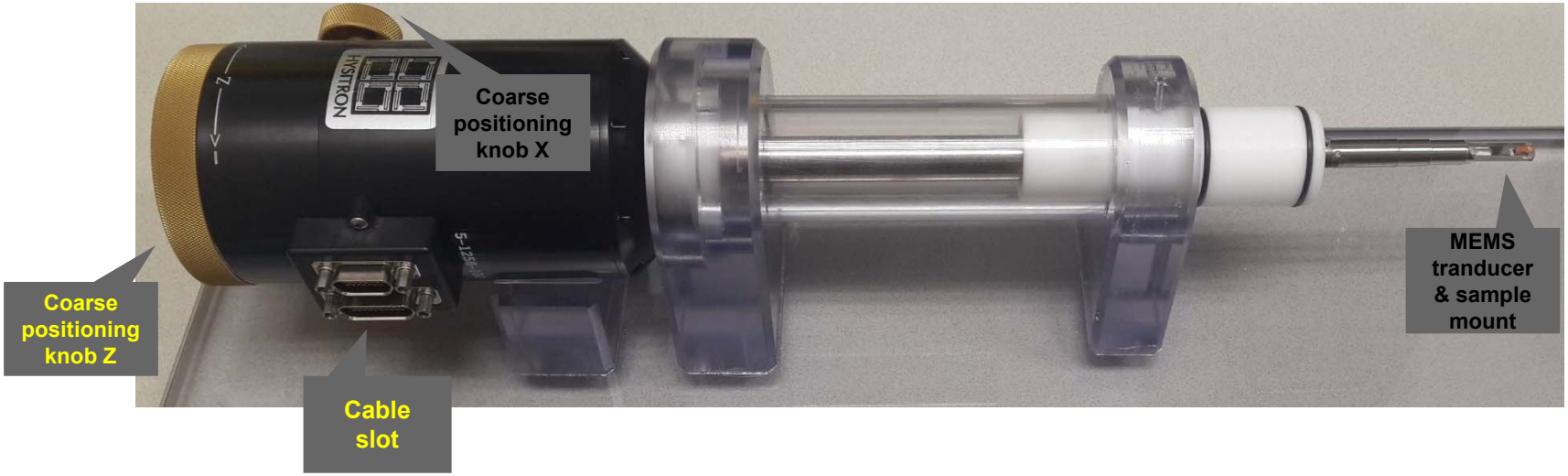

Compression test of MG nanoparticles using in-situ SEM indentation holder

- Particles prepared by dealloying $Gd_{27.5}Ti_{27.5}Al_{25}Co_{20}$ ribbon sample
  - Particle diameter, d_1 = 410 nm
  - Depth control mode, compression rate : 1 nm/s (strain rate: 2.4 x 10^{-3} s^{-1})
  - Indenting probe : Flat punch diamond tip (diameter ~ 1.2um)

20x speed video from SEM imaging (15kV, Tilt angle : 2°)

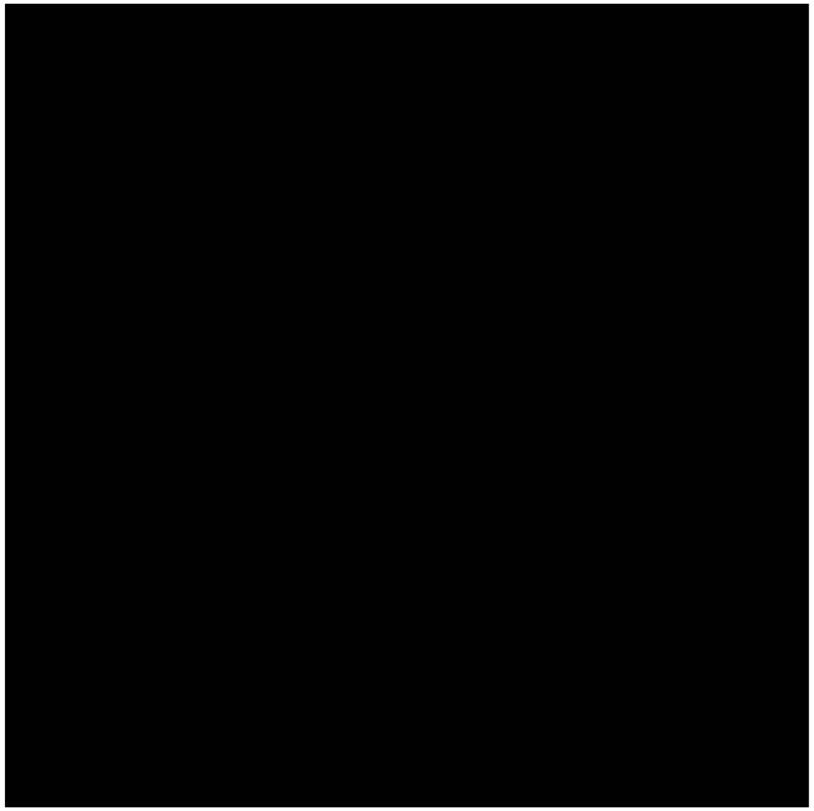

Load-depth plot from in-situ compression test

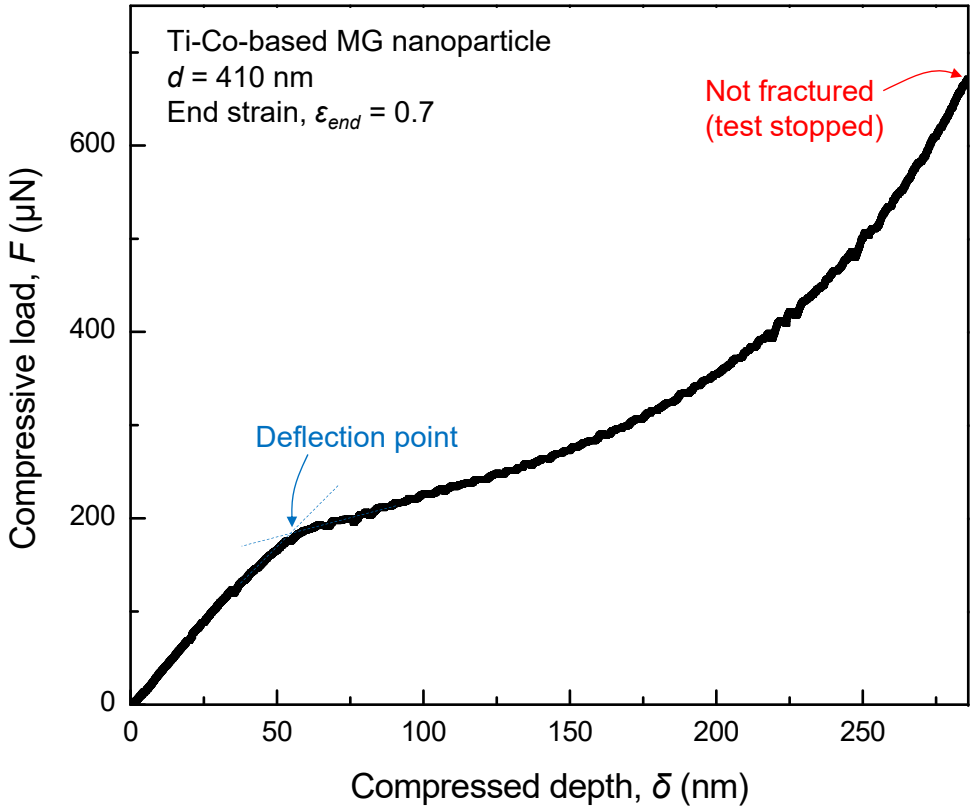

Selective dissolution of Y-rich phase in Y-Ti-Al-Co metallic glass

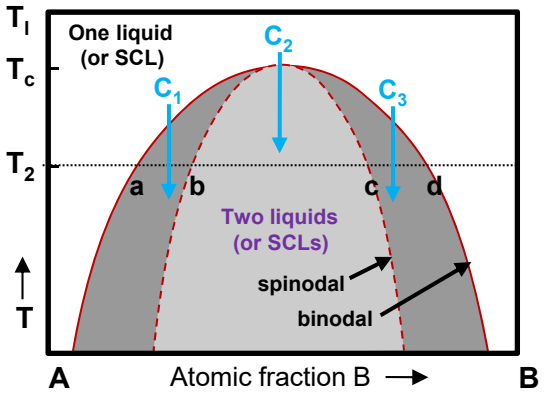

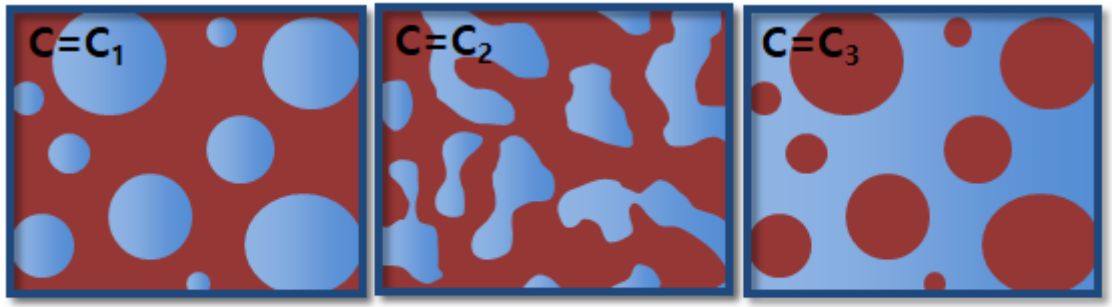

A-rich matrix
B-rich droplet

Interconnected
structure

B-rich matrix
A-rich droplet

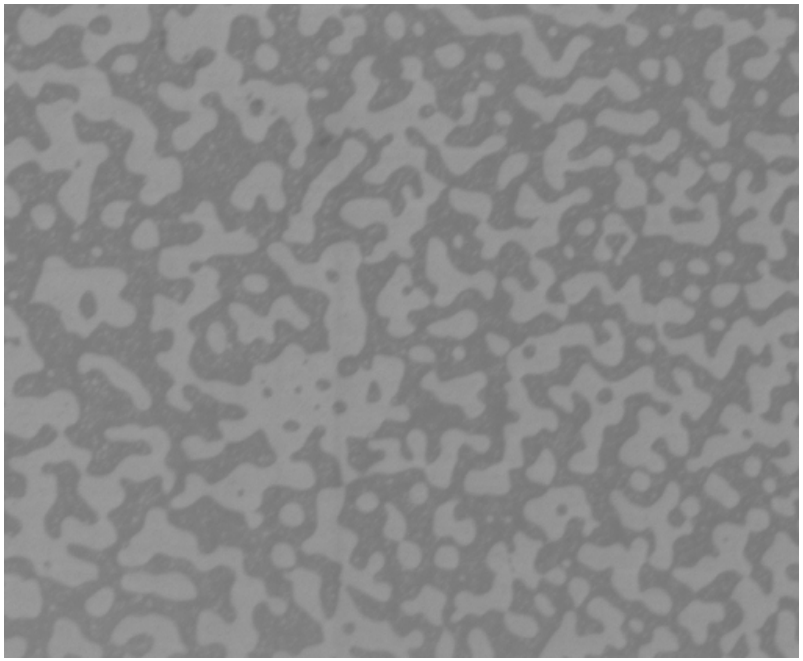

PS-MG precursor alloy

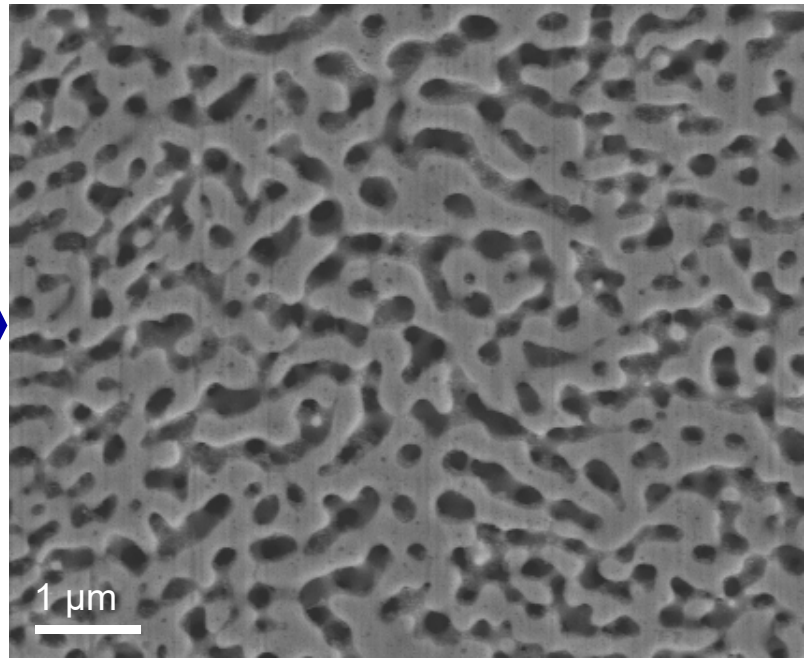

Ti-based amorphous nanofoam

Compressive deformation of metallic glass nanofoam

Ligament average size ~ **150 nm**

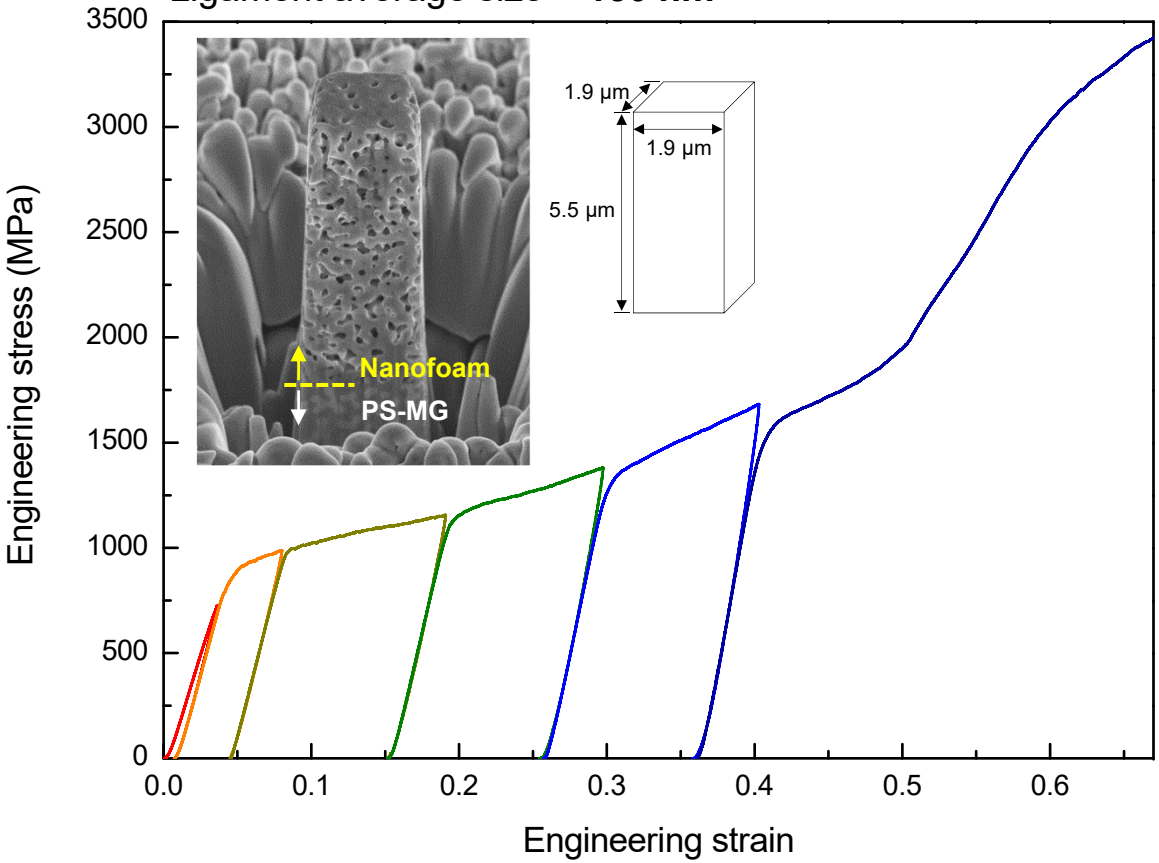

High strength (σ_{foam} ~ 880 MPa) with excellent compressive plasticity (porosity ~ 42%)

For open-cell foams,

$$\frac{\sigma_{foam}}{\sigma_{ligament}} = 0.23\,\rho_{rel}^{1.5}(1+\rho_{rel}^{0.5})$$

where $\rho_{rel} = (1 - porosity) = \frac{\rho_{foam}}{\rho_{bulk}}$

Gibson & Ashby, *Cellular Solids : Structure and properties*, 2nd ed. (1997)

➡ $\sigma_{ligament}$ ~ 4.9 GPa

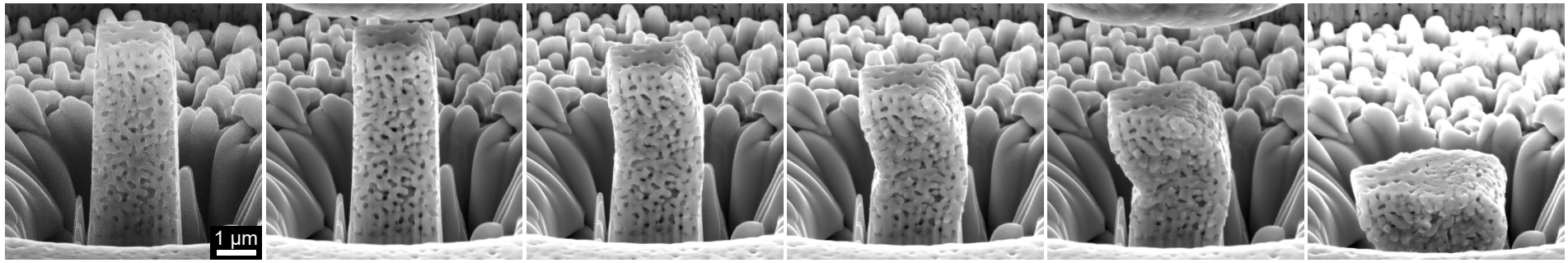

After cycle 1 | After cycle 2 | After cycle 3 | After cycle 4 | After cycle 5 | After cycle 6

5.7. Annealing of Bulk Metallic Glasses: SR → SCLR (& PS) → Crystallization

5.7.4 Crystallization: T_x ~ kinetic temperature, depends on the heating rate

- The nature of the crystalline phase produced on long time annealing was different depending on whether the annealing temperature was below Tg or above Tg.

→ In the glass state, the number of crystalline nuclei is constant, while in the supercooled liquid state, the nucleation rate is constant. In both the cases, the crystal nuclei grow through an interfacial reaction controlling process.

$$f = 1 - \exp\left(-kt^n\right)$$

k: 온도에 민감 $f(I, v)$ $\quad -\frac{\pi}{3} Iv^3$

n: 1 ~ 4 (depend on nucleation mecnanism)

Growth controlled. Nucleation-controlled.

n value is not constant, but is increasing continuously from 3.0 to 3.7 with increasing T_a.

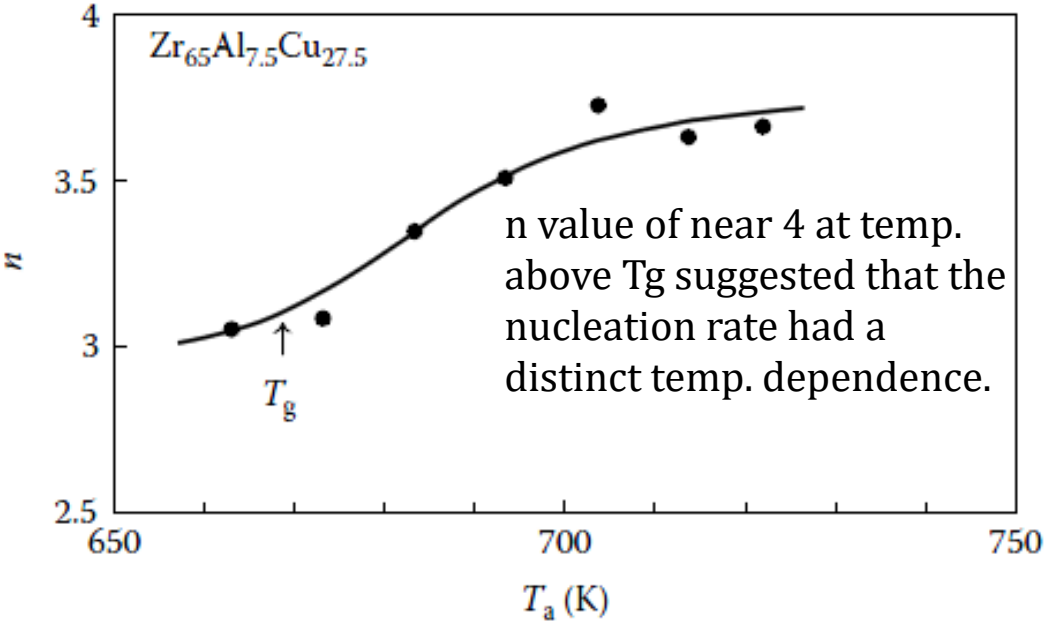

FIGURE 5.21
Variation of the Avrami exponent, n with annealing temperature, T_a during the isothermal annealing of glassy $Zr_{65}Al_{7.5}Cu_{27.5}$ alloy.

The nucleation rate is a function of both t_a and T_a. For isothermal annealing, the nucleation rate, $I(t_a)$ as a function of annealing time, t_a, at any temperature can be expressed according to the equation

$$I(t_a) = I_0 \exp\left(-\frac{\tau}{t_a}\right) \tag{5.9}$$

where

I_0 is the steady-state homogeneous nucleation rate

τ is the incubation time

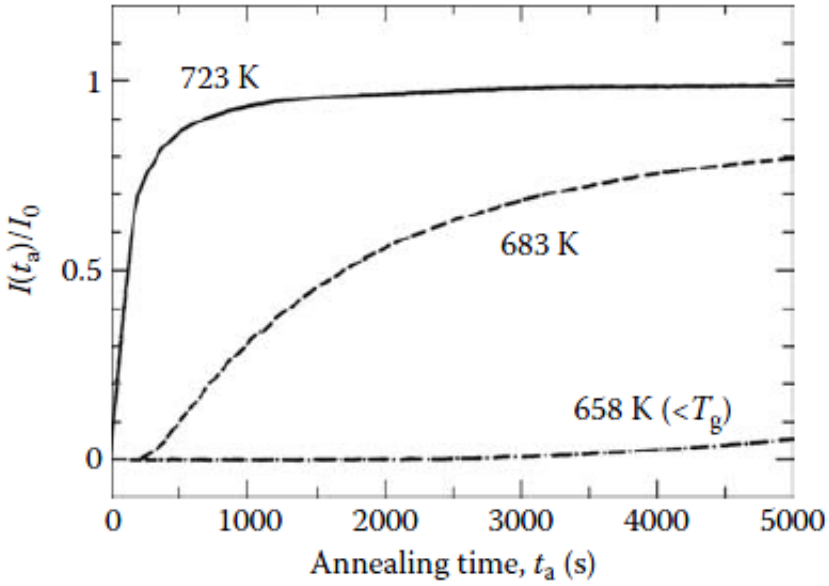

FIGURE 5.22
Variation of the reduced homogeneous nucleation rate, $I(t_a)/I_0$ evaluated from the incubation time for the precipitation of the $Zr_2(Cu,Al)$ phase with annealing time, t_a for the glassy $Zr_{65}Al_{7.5}Cu_{27.5}$ alloy annealed at 658, 683, and 723 K.

* **Non-Arrehenius-type thermal activation process**: The activation energy was calculated to change from 400 kJ/mol in the glassy solid to 260 kJ/mol in the supercooled liquid state for the nucleation of the Zr_2Cu and ZrAl phases, and from 370 kJ/mol in the glassy solid to 230 kJ/mol in the supercooled liquid state for crystallization.

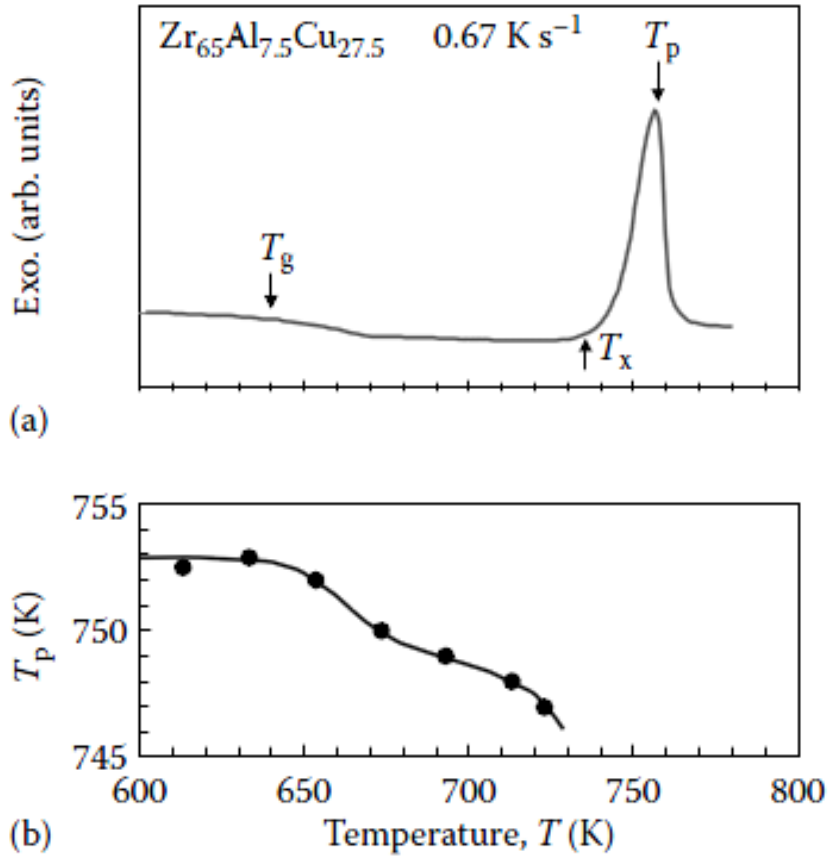

FIGURE 5.23
(a) DSC plot of the $Zr_{65}Al_{7.5}Cu_{27.5}$ glassy alloy continuously heated at a rate of 0.67 K s^{-1} (40 K min^{-1}). The T_g, T_x, and T_p values are indicated. (b) Variation of the peak temperature, T_p in the exothermic reaction due to crystallization with heating temperature, T_a.

* **The peak temperatures for nucleation and growth are well separated for glassy alloys exhibiting a significant width of the supercooled liquid region (ΔTx)**, where as for glassy alloys that do not show a Tg, these two peak temperatures overlap. This difference is expected **to reflect in the nature of the crystallized product** obtained from the supercooled liquid region. Accordingly, **the crystallized structure was examined as a function of the heating rate.**

---

* In $Zr_{65}Al_{7.5}Cu_{27.5}$ with large ΔT_x, the contribution to the growth rate increases with increasing heating rate as compared with the contribution to the nucleation rate. However, no significant change in the grain size of the Zr_2Cu phase with heating rate is seen for the $Zr_{67}Cu_{33}$ alloy with the much smaller ΔTx.

→ **Thus, the increase in the contribution to the growth rate with increasing heating rate becomes significant at temperatures just below Tx in the wide supercooled liquid region.**

- **Annealed for 1020s (17min) at 693K (above Tg): BCT Zr_2Cu phase precipitated in SCLR**/ dendritic morphology with a preferential growth direction, indicating that the redistribution of the constituent elements at the liquid-solid interface was necessary for the growth of the crystalline phase.
- **Annealed for 780 ks (9 days) at 613 K (below Tg): Zr_2Cu phase precipitated in the glassy solid**/ a nearly spherical morphology with rather smooth interface, suggesting that the growth of the Zr2Cu phase took place in the absence of significant redistribution of the constituent elements at the interface between Zr2Cu and the glassy phases/ more homogeneous distribution of Zr2Cu

---

* **The structure and morphology of the crystallized phases also appear to be a function of the Al content in the alloy.**

5.8 Effect of Environment: especially in the case of reactive glasses, for example, those based on Zr and Fe.

- In $Fe_{77}Gd_3B_{20}$ ribbon, the significant difference in the crystallization behavior was attributed to **surface oxidation, which reduces their thermal stability.**

- In $Zr_{41}Ti_{14}Cu_{12.5}Ni_{10}Be_{22.5}$, the crystallization of the glassy phase started earlier with decreasing air pressure during annealing due to deeper oxygen penetration at low pressure./ Oxygen is know to speed up the crystallization process by promoting extra heterogeneous sites for nucleation. When the oxygen pressure was low , the thickness of the surface oxide layer was small and therefore more oxygen could diffuse inside and accelerate the crystallization process.
  → The crystallization kinetics were faster at low partial pressure of oxygen.

- **The presence of oxygen in the alloys has a significant effect on the nature of the phases formed after quenching and also those formed on crystallization.** Therefore, it is essential that the alloys are clean and devoid of impurities, especially in active metals. Otherwise comparison between results by different investigators becomes difficult.

5.9 Effect of Pressure during Annealing

- hot pressing, hot extrusion, hot isostatic pressing, and other recently developed methods such as spark plasma sintering
- becomes useful to evaluate the thermal stability of glasses when exposed to high pressures
- critical for optimizing the consolidation process parameter or deforming in the supercooled liquid region

* Four different effects of pressure during annealing

1. Since there is an increase in the density of the product on crystallization (the glassy alloys are about 1%–2% less dense than their crystalline counterparts), it is natural to expect that the application of pressure would reduce the free volume in the glassy phase and therefore it is expected that crystallization will be accelerated. Such a process could easily happen when the glass crystallizes by a polymorphous mode.
2. Due to the retarded mobility of atoms (diffusivity) under high pressures, atomic diffusion is reduced and therefore crystallization is retarded as evidenced by the increase of crystallization temperatures. Since atomic diffusion is required for primary and eutectic-type crystallization modes, the application of pressure is expected to retard the crystallization of metallic glasses when the transformation takes place by any of these modes.

3. The relative Gibbs free energies of the glassy and other competing crystalline phases and also the activation barriers could be altered by the application of pressure. Consequently, metastable phases could form, the relative amounts of the different phases could be different, or alternately, different crystallization paths could be followed. The situation will be decided by the sign and magnitude of the variation of the crystallization temperature with pressure, that is, dT_x/dP.

   As an example, during the primary crystallization of Fe–B glassy alloys, α-Fe is formed at atmospheric pressure. However, when crystallization is conducted at pressures above 100 kbar, the formation of the metastable hcp ε-Fe phase was found to form [148]. Similarly, instead of the equilibrium tetragonal Nb_3Si phase, the cubic A15 Nb_3Si phase formed in the Nb–Si system during crystallization at high pressures in the glassy Nb–Si alloys [149]. Again, in the case of the crystallization of the $Zr_{41}Ti_{14}Cu_{12.5}Ni_{10}Be_{22.5}$ glassy alloy, Yang et al. [150] reported that the primary crystallized phase was the same at all pressures studied, but the subsequent phase-formation sequence was different at different temperatures.

4. The last effect of the application of pressure to metallic alloys is that amorphization could occur, that is, pressure-induced amorphization takes place [151–153]. For example, Wang et al. [151] reported that by cooling the $Zr_{41}Ti_{14}Cu_{12.5}Ni_{10}Be_{22.5}$ liquid at a high pressure of 6 GPa, they were able to obtain a high-density glassy alloy that had a structure and properties different from the low-density glassy alloy obtained by water quenching the melt.

TABLE 5.6

Effect of Pressure in Increasing the Crystallization Temperature of Bulk Metallic Glasses

Composition	Pressure Range Used (GPa)	Rate of Increase of T_x(K GPa^{-1})	Reference
$Al_{89}La_6Ni_5$	0–4	Decrease at a rate of 50 between 0 and 1 GPa and then increase at a rate of 25	[154]
$Fe_{72}P_{11}C_6Al_5B_4Ga_2$	0–2.4	30 (T_x dropped at higher pressures between 2.4 and 3.2)	[147]
$Mg_{60}Cu_{30}Y_{10}$	0–4	16	[155]
$Pd_{40}Ni_{40}P_{20}$	0–4.2	11	[156]
$Pd_{40}Cu_{30}Ni_{10}P_{20}$	0–4	11	[157]
$Zr_{66.7}Pd_{33.3}$	0–4	22	[135]
$Zr_{70}Pd_{30}$	0–3	11 ± 3 for quasicrystalline phase 9 ± 4 for intermetallic phase	[158]
$Zr_{65}Al_{7.5}Ni_{10}Cu_{7.5}Ag_{10}$	0–4.2	9.4 for T_{x1} No change for T_{x2}	[159]
$Zr_{48}Nb_8Cu_{14}Ni_{12}Be_{18}$	0–4.4	9.5	[160]
$Zr_{41.2}Ti_{13.8}Cu_{12.5}Ni_{10}Be_{22.5}$	0–3	19	[161]
$Zr_{46.8}Ti_{8.2}Cu_{7.5}Ni_{10}Be_{27.5}$	0–4.2	1.7	[162]
$Zr_{41}Ti_{14}Cu_{12.5}Ni_{10}Be_{22.5}$	0.5–6.5	12.8 (a sudden drop occurred at 5.6 GPa)	[150]

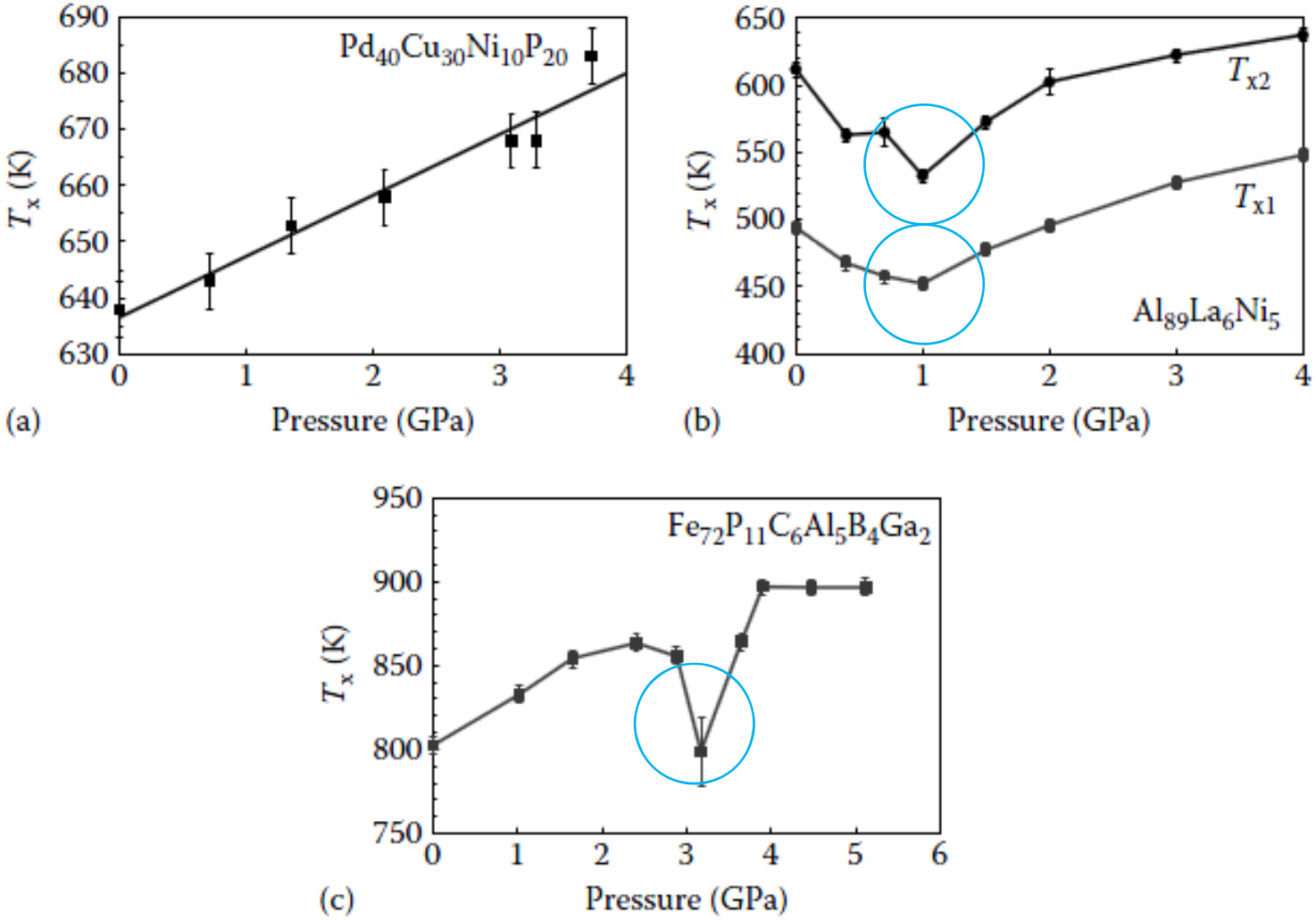

FIGURE 5.24
Variation of T_x with pressure in bulk metallic glassy alloys. Note that the T_x usually increases with increasing pressure although there are cases where either a decrease or no change has also been observed. Three typical examples are shown in (a) $Pd_{40}Cu_{30}Ni_{10}P_{20}$ glass, (b) $Al_{89}La_6Ni_5$ glass, and (c) $Fe_{72}P_{11}C_6Al_5B_4Ga_2$ glass. (Reprinted from Jiang, J.Z. et al., *J. Appl. Phys.*, 87, 2664, 2000. With permission.)

The rate of nucleation, I can be represented by the equation

$$I = I_0 \exp\left(-\frac{\Delta G^* + \Delta G^d}{RT}\right)$$

where

I_0 is a constant

ΔG^* is the thermodynamic activation barrier, that is, free energy required to form the critical nucleus

ΔG^d is the activation energy for diffusion (to transport atoms across the interface)

R is the universal gas constant

T is the temperature

$\Delta G^* + \Delta G^d = \Delta G$ is the total energy required for the nucleation

$$\Delta G^* = \frac{16\pi\sigma^3}{3\Delta G_v^2} = \frac{16\pi\sigma^3}{3\left(G_c - G_a\right)^2}$$

where

σ is the interfacial energy between the amorphous and crystalline phases

G_c and G_a are the Gibbs free energies of the crystalline and amorphous phases, respectively

At a given temperature and pressure, ΔG^* can be expressed as

$$\left(\Delta G^*\right)_{P,T} = \frac{16\pi\sigma^3 \left(V_c\right)^2}{3\left[P\left(V_a - V_c\right) - \Delta G^{a\to c} + E\right]^2}$$

where

V_c and V_a are the molar volumes of the crystalline and amorphous phases, respectively $\Delta G^{a\to c} = G_c - G_a$

E is the elastic energy induced by the volume change when the phase transformed from the amorphous to the crystalline state

Assuming a negligible pressure dependence of $\Delta G^{a\to c}$, E, and σ, we can see that ΔG^* decreases with increasing pressure and therefore crystallization is favored.

$$\left(\frac{\partial G}{\partial P}\right)_T = -\frac{32\pi\sigma^3}{3\left(\Delta G^{a\to c}\right)^3}\left(V_c - V_a\right) + \left(\frac{\partial \Delta G^d}{\partial P}\right)_T$$

($V_c < V_a$; $-$ in the denominator; $-$ outside; $+$ on the second term)

Whether increasing pressure promotes or retards crystallization is determined by the magnitudes of the two terms.

Ex) polymorphous mode→no atomic redistribution → always promotes crystallization